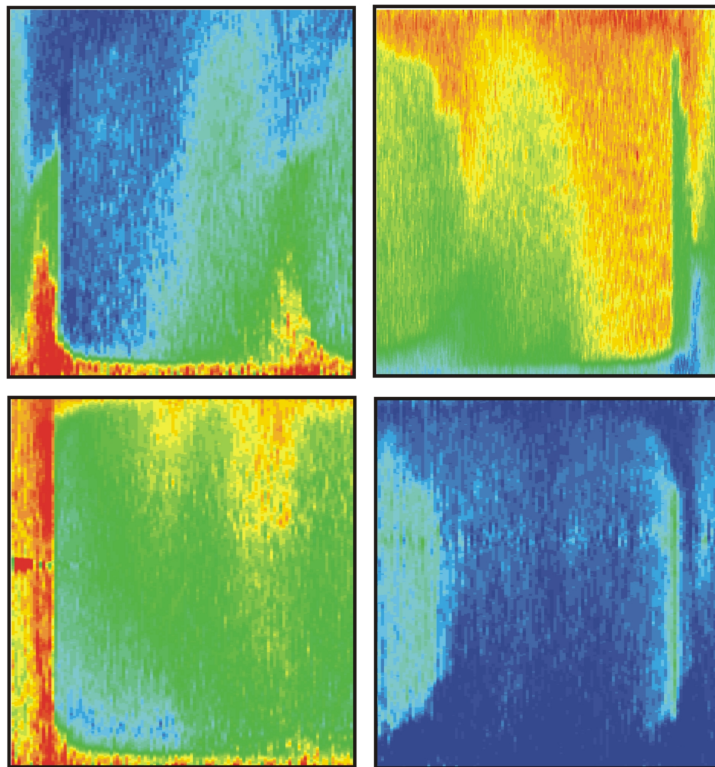# Adiabatic transport in the quantum Hall regime:

Comparison between transport and scanning force microscopy investigations

Franck DAHLEM

Adiabatic transport in the quantum Hall regime: Comparison between transport and scanning force microscopy investigations

Von der Fakultät Mathematik und Physik der Universität Stuttgart zur Erlangung der Würde eines Doktors der Naturwissenschaften (Dr. rer. nat.) genehmigte Abhandlung

vorgelegt von

FRANCK DAHLEM

aus Moutiers, Frankreich

Hauptberichter:	**Prof. Dr. K. v. KLITZING**
Mitberichter:	**Prof. Dr. P. MICHLER**
Tag der Einreichung:	**4 April 2008**
Tag der mündlichen Prüfung:	**13 June 2008**

To Rudeesun

Keith Jarrett, the Köln concert.

Contents

Symbols

Symbols

$\mathbf{A}$	Vector potential
$\mathbf{B}$	Magnetic flux density
d	Depletion length
D_0	Density of states at zero magnetic field
$D(\epsilon)$	Density of states (DOS)
$D_{\mathrm{T}}(\epsilon)$	Thermodynamic density of states (TDOS)
$-e$	Electron charge
$\mathbf{E}$	Electrical field
ε	Electron energy
ε_i^z	Energy minimum of the ith subband due to potential confinement in z direction
ε_{c}	Energy minimum of the conduction band
ε_{F}	Fermi energy
$\varepsilon_{n,s}$	Single-particle eigen energy in quantum state n and spin s
ε_{v}	Energy maximum of the valence band
$f(\varepsilon)$	Fermi-Dirac distribution function
g_{s}	Spin degeneracy
g^*	Landé factor
$\hbar = h/2\pi$	where h the Planck constant
I_{net}	Net current
j	Current density
k	Wave number
k_{B}	Boltzmann constant

L Spatial length

$l_B = \sqrt{\hbar/eB}$ Magnetic length

m^* Effective electron mass

m_0 Bare electron mass

n_{s} Electron sheet density

q Charge

$R_K \widehat{=} h/e^2$ von Klitzing constant

$R_{K-90} = 25812.807\,\Omega$ Conventional von Klitzing constant

$R_n = l_B\sqrt{2n+1}$ Cyclotron radius

R_{xx} Longitudinal resistance

R_{xy} Hall resistance

T Temperature

$\mathbf{v}_{\mathrm{D}}$ Drift velocity

V Voltage

$\alpha = e^2/h \cdot (\mu_0 \cdot c/2)$ Fine structure constant

ϵ_0 Dielectric constant in vacuum

ϵ_{r} Relative dielectric constant

μ Electron mobility

μ_{ch} Chemical potential

μ_{elch} Electrochemical potential

ϕ Electrostatic potential

$\chi(x), \varphi(y), \Psi(z)$ Single particle wave function

$\tilde{\sigma}$ Conductivity tensor

$\omega_c = eB/m^*$ Cyclotron frequency

Introduction

The quantum Hall effect (QHE) is a transport phenomena occurring in two-dimensional electron or hole system (2DES or 2DHS) under high magnetic field. It corresponds to quantized Hall resistance plateaus appearing simultaneously with zero longitudinal resistances. The value of the Hall resistance plateau in the integer quantum Hall effect (IQHE) is $h/(e^2 \cdot i)$ with $i = \{1, 2 \ldots\}$. It was firstly discovered by Klaus von Klitzing in 1980 [1, 2] who was honored by the Nobel prize in 1985. Later a second Nobel prize was given to D.C. Tsui, H.L. Störmer and R.B. Laughlin for the discovery of the fractional quantum Hall effect [3–7]. The value of the Hall resistance plateau in the fractional quantum Hall effect is $h/(e^2 \cdot f)$ where f is a fractional number. In metrology, quantized Hall resistance plateaus are measured in order to define the standard resistance $R_{K-90} = 25812.807\,\Omega$ -called the conventional von Klitzing constant.

After twenty-five years and several books on the topic [8–11], the quantum Hall effect is still the subject of intensive research (we can cite for instance the Bose-Einstein condensation in 2DES bilayer [12–17], the non-abelian 5/2 state [18], or the unconventional QHE in graphene sheet [19]). Over these years, several microscopic pictures have been suggested to explain the quantized Hall resistance. Important progresses on this field have been done in our group via the local probing of the Hall potential profiles by scanning force microscopy [20,21]. Following these local measurements, a description of the quantum Hall effect has been proposed in which the screening of the electrostatic potential plays a fundamental role. In this picture, the non dissipative current is carried by incompressible strips (IS) which separate compressible strips (CS) with different electrochemical potential. An incompressible strip is a region in which the Fermi energy is located inside the energy gap (the electron density is constant and the electrostatic potential is changing) whereas a compressible strip occurs if the Fermi energy is pinning inside a Landau level (the electron density is changing and the electrostatic potential is screening). Recent self-consistent calculations of R. Gerhardts *et al.* [22–24] support such description of the quantum Hall effect in terms of compressible and incompressible strips.

The following PhD work demonstrates that the model based on compressible and incompressible strips accounts also for the adiabatic transport features observed on high mobility samples in the quantum Hall regime. Usually presented in the literature with the edge state picture, such features are the disappearance of peaks in the Shubnikov-de Haas oscillations, the extension of quantum Hall plateaus to lower magnetic fields and the existence of non-local resistances. The following research will show that in adiabatic situations, compressible regions with an *un-*

usual difference of electrochemical potential are found to coexist along the same edge due to an insulator-like incompressible strip in between and due to the lack of impurities scattering. The insulator properties of incompressible strips in front of the alloyed ohmic contacts are found to be anisotropic with a dependency on the orientation of the contact borderline with respect to the crystal direction.

The thesis is organized as following: The physics of 2DES is the topic of the *first chapter* in which the quantum Hall effect and different microscopic pictures for its explanation are reviewed. The scanning force microscope as a local voltage probe to microscopically study the QHE is described with the experimental setup in *chapter 2*. *Chapter 3* offers some basics on the adiabatic transport in term of the edge state picture. The magneto-transport and scanning probe measurements on four-terminal Hall bars with a high mobility 2DES (about $130 \, \mathrm{m^2/V\,s}$) are shown in *chapter 4* and *5*, respectively. As a *final chapter*, the presentation of an adiabatic transport model based on compressible and incompressible strips with different width at the contact borderline depending on the heterostructure orientation on the crystal is introduced to explain our complete measurements.

Bibliography

[1] K. Klitzing, G. Dorda, and M. Pepper, Phys. Rev. Lett. **45**, 494 (1980).

[2] K. Klitzing, Rev. Mod. Phys. **58**, 519 (1986).

[3] D. Tsui, Rev. Mod. Phys. **71**, 891 (1999).

[4] D. Tsui, H. Störmer, and A. Gossard, Phys. Rev. Lett. **48**, 1559 (1982).

[5] H. Störmer, Rev. Mod. Phys. **71**, 875 (1999).

[6] R. Laughlin, Rev. Mod. Phys. **71**, 863 (1999).

[7] R. Laughlin, Phys. Rev. Lett. **50**, 1395 (1983).

[8] S. Datta, *Electronic transport in mesoscopic systems* (Cambridge University Press, Oxford, 1995), Vol. 54, p. 437.

[9] H. Kamimura and H. Aoki, *The physics of interacting electrons in disordered systems* (Clarendon Press, Oxford, 1989).

[10] R. Prange and S. Girvin, *The quantum Hall effect* (Springer, Berlin, 1987).

[11] T. Chakraborty and P. Pietiläinen, *The quantum Hall effects, integral and fractional* (Springer, Berlin, 1995).

[12] J. P. Eisenstein and A. H. MacDonald, Nature **432**, 691 (2004).

[13] M. Kellogg, I. B. Spielman, J. P. Eisenstein, L. N. Pfeiffer, and K. W. West, Phys. Rev. Lett. **88**, 126804 (2002).

[14] M. Kellogg, J. P. Eisenstein, L. N. Pfeiffer, and K. W. West, Phys. Rev. Lett. **93**, 036801 (2004).

[15] I. B. Spielman, J. P. Eisenstein, L. N. Pfeiffer, and K. W. West, Phys. Rev. Lett. **84**, 5808 (2000).

[16] I. B. Spielman, J. P. Eisenstein, L. N. Pfeiffer, and K. W. West, Phys. Rev. Lett. **87**, 036803 (2001).

[17] R. D. Wiersma, J. G. S. Lok, S. Kraus, W. Dietsche, K. von Klitzing, D. Schuh, M. Bichler, H.-P. Tranitz, and W. Wegscheider, Phys. Rev. Lett. **93**, 266805 (2004).

[18] A. Stern and B. I. Halperin, Phys. Rev. Lett. **96**, 016802 (2006).

[19] K. Novoselov, E. McCann, S. V. Morozov, V. I. Fal'ko, M. I. Katsnelson, U. Zeitler, D. Jiang, F. Schedin, and A. K. Geim, Nat. Phys. **2**, 177 (2006).

[20] P. Weitz, E. Ahlswede, J. Weis, K. Klitzing, and K. Eberl, Physica E **6**, 247 (2000).

[21] E. Ahlswede, P. Weitz, J. Weis, K. Klitzing, and K. Eberl, Physica B **298**, 562 (2001).

[22] A. Siddiki and R. Gerhardts, Phys. Rev. B **68**, 125315 (2003).

[23] A. Siddiki and R. Gerhardts, Phys. Rev. B **70**, 195335 (2004).

[24] A. Siddiki, Ph.D. thesis, Model calculation of current and density distributions in dissipative Hall bar, PhD thesis, Max-Planck-Institut für Festkörperforschung / University of Würzburg, 2005.

1. Two-dimensional electron system (2DES) in high magnetic fields

This chapter summarizes the basic properties of a two-dimensional electron system (2DES). After a brief presentation of its properties at zero magnetic field, the electrical transport through 2DES at low and high magnetic field is discussed. A major part of the chapter is then dedicated to the integer quantum Hall effect (IQHE). At the beginning, the bulk picture and the edge state picture which are generally used to describe IQHE are introduced. Later on, recent experimental [1–3] and theoretical works [4–6] in the group of Klaus von Klitzing are discussed in detail. Those works suggests a microscopic picture of the integer quantum Hall effect based on compressible and incompressible strips. In this PhD thesis, we will use this strip picture to explain our experimental results.

Contents

1.1. 2DES embedded in AlGaAs/GaAs heterostructure

In the quantum Hall effect community, the 2DES is usually obtained from $Al_xGa_{1-x}As/GaAs$ heterostructures. Such III-V material is preferred to the silicon MOSFET due to its higher electron mobility. A typical layer sequence to create 2DES based on $Al_xGa_{1-x}As/GaAs$ is shown in Fig. 1.1(a). By using molecular beam epitaxy (MBE), the sharp interface between the AlGaAs and GaAs is realized with perfect crystal quality. Due to a conduction band offset between AlGaAs and GaAs, the AlGaAs layer doped with silicon atoms gives electrons to the GaAs layer. These electrons are trapped at the heterojunction since Si+ ions create an attractive triangular shaped confinement potential (Fig. 1.1(b-c)). The electrons in this potential well can freely move in the plane parallel to the interface (x and y directions). Their eigenfunctions are
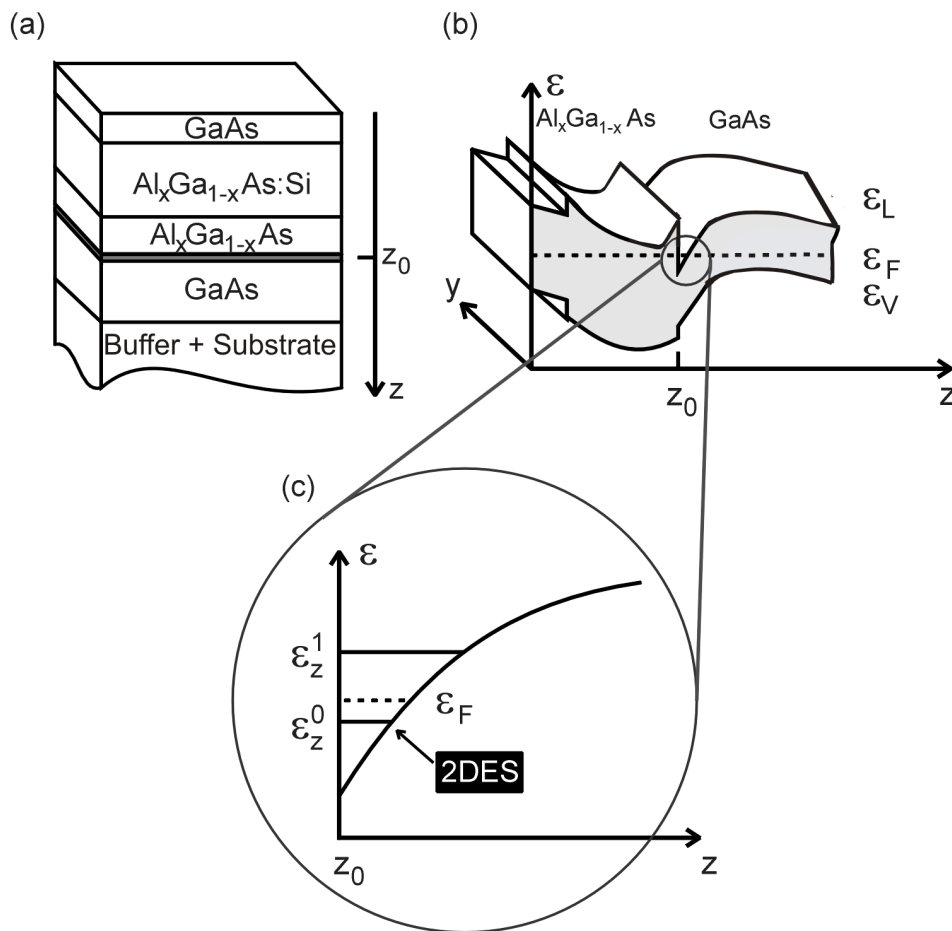
Figure 1.1.: **a)** Layer sequence of an $Al_xGa_{1-x}As/GaAs$ heterostructure. **b)** Bending of the conduction band minimum and valence band maximum at the junction between the AlGaAs layer and the GaAs layer. A triangle-shaped potential well is formed. **c)** At respectively low electron density, the electrons at the interface create a 2DES (Figure taken from E. Ahlswede PhD thesis [3]).

plane waves with a wave vector $\vec{k}$. In z direction a quantization of the energy occurs due to the spatial confinement. The energy spectrum in **k**-space is therefore described by

$$\varepsilon(i, k_x, k_y) = \varepsilon_i^z + \frac{\hbar^2 k_x^2}{2m^*} + \frac{\hbar^2 k_y^2}{2m^*} \tag{1.1}$$

where $m^* \approx 0.067\, m_0$ is the effective electron mass in GaAs. The integer number $i = \{0, 1, 2 \ldots\}$ labels the eigenenergy values in z direction. These quantized levels define the subband minimum [i]. At low temperature and for low electron density, all electrons occupy the first subband ε_0^z - a two-dimensional electrons system (2DES) is formed (see Fig. 1.1 (c)). Such systems have been investigated for several decades and its properties have motivated a lot of interests [7]. One specificity of 2DES, it is its density of states at zero magnetic field which is constant and equal to

$$D(\epsilon) = D_0 = \frac{m^*}{\pi \hbar^2}\,. \tag{1.2}$$

It follows that the Fermi energy, given by

$$\varepsilon_{\mathrm{F}} = \frac{\pi \hbar^2}{m^*} n_s\,, \tag{1.3}$$

linearly depends on the sheet electron density n_s. For typical 2DES with a density around few $10^{15}\ \mathrm{m}^{-2}$, this energy ε_{F} is in between 4 and 20 meV.

1.2. Classical magneto-transport

In magnetic field, 2DES shows interesting transport properties recorded via resistance measurements. Performed at low field, these magneto-resistances (MR) allow to extract the relevant electrical properties of the system i.e. the density n_s and the mobility μ of the charge carriers. The Hall bar geometry presented in the inset of figure 1.2 is a typical setup for transport measurement. The current is applied in between the terminals 1 and 4. The longitudinal resistance $R_{xx} = V_{xx}/I_{\mathrm{net}} = R_{14,23}$ is measured with two contacts located at the same edge (contact 2 and 3) which probe the longitudinal potential drop. The Hall resistance $R_{xy} = V_{xy}/I_{\mathrm{net}} = R_{14,26}$ is recorded with voltage probing contacts located at two opposite mesa edges (contact 2 and 6). The interest on these magneto-resistances comes from their relation to the microscopic electrical properties of the 2DES. This link is usually derived by using the classical equation of motion for a Drude electron - an electron of representative mean properties,

$$m^* \frac{d\mathbf{v}_{\mathrm{D}}}{dt} + \frac{m^*}{\tau} \mathbf{v}_{\mathrm{D}} = -\mathbf{e}[\mathbf{E} + (\mathbf{v}_{\mathrm{D}} \times \mathbf{B})]\,, \tag{1.4}$$

---

[i] The subband separation $\varepsilon_{i+1}^z - \varepsilon_i^z$ is in the order of 10 to 20 meV.

where $\mathbf{v}_D$ denotes the drift velocity of the Drude electron, $\mathbf{B} = (0, 0, B)$ the magnetic field, $\mathbf{E} = (E_x, E_y, 0)$ the applied electric field. In stationary condition, the first term $m^* d\mathbf{v}_D/dt$ is
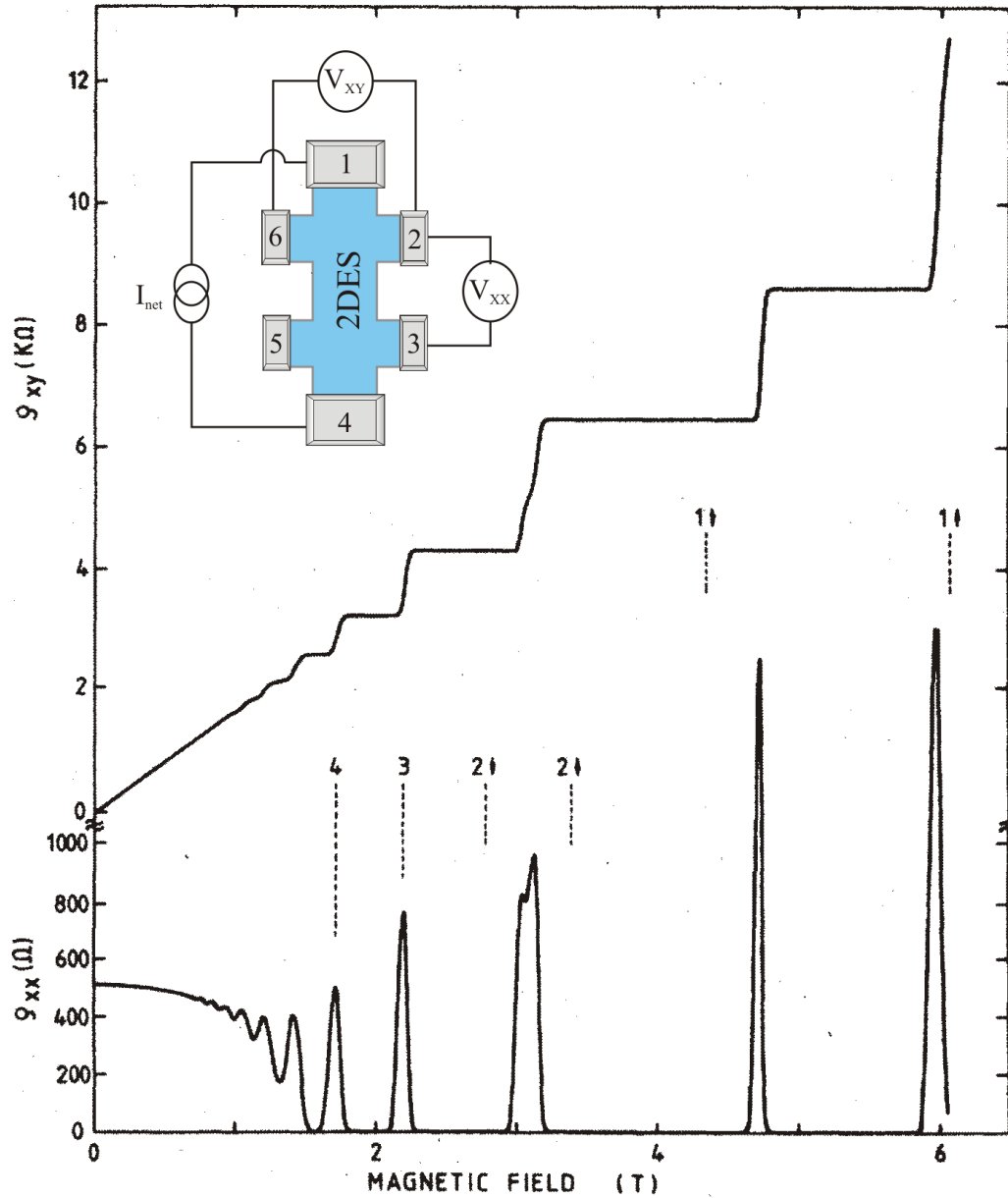
Figure 1.2.: Typical magneto-transport curves: Classical magneto-resistance at low magnetic field and the integer quantum Hall effect at high field [8]. Inset: Hall bar geometry used for measuring the Hall resistance $R_{xy} = V_{xy}/I_{\text{net}} = R_{14,26}$ and the longitudinal resistance $R_{xx} = V_{xx}/I_{\text{net}} = R_{14,23}$.

zero. By replacing $\mathbf{v}_D$ with $\mathbf{j} = -en_s\mathbf{v}_D$, the equation (1.4) can be rewritten as $\mathbf{j} = \tilde{\sigma}\mathbf{E}$, i.e.

$$\begin{pmatrix} j_x \\ j_y \end{pmatrix} = \frac{en_s\mu}{1 + (\mu B)^2} \begin{pmatrix} 1 & \mu B \\ -\mu B & 1 \end{pmatrix} \begin{pmatrix} E_x \\ E_y \end{pmatrix} \tag{1.5}$$

with $\mu = e\tau/m^*$ the electron mobility and τ the average scattering time. In magnetic field, the conductivity $\tilde{\sigma}$ is not a scalar number but a tensor of rank two. The mobility and the density of charge carriers are linked to the microscopic Drude parameters τ and m^* by the equation (1.5). They can also be related to the longitudinal and Hall resistance [9]. From the symmetry ($\sigma_{xx} = \sigma_{yy}$ and $\sigma_{xy} = -\sigma_{yx}$), the inversion of the conductivity into resistivity is given by

$$\begin{pmatrix} \rho_{xx} & \rho_{xy} \\ -\rho_{xy} & \rho_{xx} \end{pmatrix} = \frac{1}{\sigma_{xx}^2 + \sigma_{xy}^2} \begin{pmatrix} \sigma_{xx} & \sigma_{xy} \\ -\sigma_{xy} & \sigma_{xx} \end{pmatrix} .$$

A linear relation between the Hall resistance and the magnetic field follows:

$$R_{xy} = \rho_{xy} = \frac{B}{en_s} . \tag{1.6}$$

This linear dependency with respect to the magnetic field is in agreement with the measurement of the Hall resistance at low field as shown in figure 1.2. The curve $R_{xy}(B)$ is inversely proportional to the electron density and the fit of the slope allows to extract the electron density value n_s. From the Drude model, the longitudinal resistance is constant over the low field range,

$$R_{xx} = \frac{L}{W}\rho_{xx} = \frac{L}{W}\frac{1}{en_s\mu} , \tag{1.7}$$

and the measurement of this resistance around $B = 0$ gives the electron mobility μ. The equations (1.6) and (1.7) will be used to extract the electron density and mobility of our 2DES (see section 4.1.4).

1.3. The quantum Hall effect (QHE)

In high magnetic field B and at low temperature, the 2DES magneto-resistance (MR) shows deviations from the classical MR. Instead of a linear behavior with respect to B, the Hall resistance R_{xy} shows some plateaus around certain magnetic field values. These plateaus are equal to a quantized resistance of $h/(e^2 \cdot i)$ with $i = \{1, 2 \ldots\}$. Simultaneously the longitudinal resistance R_{xx} goes to zero (see Fig. 1.2). The precise quantization of the Hall resistance combined with the vanishing of the longitudinal resistance are the two transport phenomena named as quantum Hall effect (QHE). Similar transport features [10–14] occur at higher magnetic field

with a value of quantization corresponding to $h/(e^2 \cdot f)$ where f is a fractional number. This transport is called fractional quantum Hall effect (FQHE) [ii].

The special feature of the QHE is the fact that a quantized Hall resistance does not depend on the sample geometries and materials. This resistance is only related to two universal constants: e and h. In his original work, Klaus von Klitzing proposed to use the quantum Hall effect to precisely determine the value of the fine structure constant $\alpha = e^2/h \cdot (\mu_0 \cdot c/2)$. Since the Hall plateau resistance is measured with very high accuracy, the value $R_{K-90} = 25812.807\,\Omega$ - called the conventional von Klitzing constant R_{K-90}, has been selected as the standard of resistance starting since 1990. Several descriptions of the phenomena have been proposed based on either bulk localization or edge states or recently on compressible and incompressible strips [15–17]. Although all of them start from the Landau level discretization of the energy spectrum in high magnetic field (section 1.4), the microscopic picture of these model is drastically different.

1.4. Landau level quantization in high magnetic field

In high magnetic field (few Telsa), the field opens gaps in the energy spectrum and reveals the quantum Hall effect in the transport measurements. To determine this energy discretization, a quantum treatment of homogeneous 2DES is performed by solving of the single-particle Schrödinger equation

$$\left[\frac{(\hat{\mathbf{p}} + e\mathbf{A})^2}{2m^*} + eV(x,y)\right]\psi(x,y) = \varepsilon\psi(x,y). \tag{1.8}$$

The homogeneous magnetic field $\mathbf{B}$ is included in the equation through the vector potential $\mathbf{A}$, formulated in Landau gauge[iii] as $\mathbf{A} = (-By, 0, 0)$. The function $\psi(x,y)$ is the eigenwave function [iv] of a single electron and $V(x,y)$ is the sum of the Hartree-Fock and confinement potential due to the finite size of the system. For $V(x,y) = 0$ and after introducing the Landau gauge symmetry, the Schrödinger equation is rewritten as

$$\frac{1}{2m^*}\left[(\hat{p}_x - eBy)^2 + \hat{p}_y^2\right]\psi(x,y) = \varepsilon\psi(x,y). \tag{1.9}$$

Since the Hamiltonian does not contain the operator $\hat{x}$, the operator $\hat{p}_x$ commutes with the Hamiltonian - i.e. $[\hat{H}, \hat{p}_x] = 0$, and the problem is separable in two independent subspaces for x and y. The wave function $\psi(x,y)$ is therefore splitted as $\psi(x,y) = \chi_k(x) \otimes \varphi_n(y)$ with

---

[ii] In this PhD thesis, the temperature of our cryogenic scanning force microscope being limited to $T \approx 1\,K$, the local potential is exclusively measured in the integer quantum Hall regime.

[iii] The choice of the gauge depends on the symmetry. In systems with rotational symmetry (quantum dots with circular confinement or devices with isotropic electron-electron interaction), it is better to use a cylindric gauge.

[iv] The total single particle wave function is given by $\psi(x,y) \otimes \Psi(z)$ with $\Psi(z)$ the wave function related to the confinement in z direction.

$\chi_k(x) = e^{ik_x x}/\sqrt{L_x}$ due to the x-invariance in periodic conditions. The operator $\hat{p}_x$ and $\hat{p}_y$ in the x- and y-subspace are expressed by $\hat{p}_x = -i\hbar\partial/\partial x$ and $\hat{p}_y = -i\hbar\partial/\partial y$. It follows,

$$\frac{1}{2m^*}\left[(\hbar k_x - eBy)^2 - \hbar^2\partial^2/\partial y^2\right]\varphi_n(y) = \varepsilon_n\varphi_n(y). \tag{1.10}$$

This equation (1.10) describes a harmonic oscillator in y-direction

$$\left[-\frac{\hbar^2}{2m^*}\frac{\partial^2}{\partial y^2} + \frac{1}{2}m^*\omega_c^2\cdot(y-Y)^2\right]\varphi_n(y) = \varepsilon_n\varphi_n(y) \tag{1.11}$$

with a cyclotron frequency $\omega_c = eB/m^*$ and a center coordinate $Y = -l_B^2\cdot k_y$ (the parameter $l_B = \sqrt{\hbar/eB}$ is the magnetic length [v]). The equidistant eigenvalues ε_n of this harmonic oscillator are

$$\varepsilon_n = \hbar\omega_c\left(n+\frac{1}{2}\right), \qquad n = \{0,1,2\ldots\}. \tag{1.12}$$

The equation (1.12) shows how 2DES energy spectrum is quantized due to the magnetic field. The effect is well pronounced in GaAs due to its very small effective mass [vi]. Finally to obtain the complete expression of the single electron energy, a Zeeman term related to the electron spin s has to be added to this quantized energy spectrum and to the subband energy ε_z^0:

$$\varepsilon_{n,s} = \varepsilon_z^0 + \hbar\omega_c(n+\frac{1}{2}) + sg^*\mu_B B \qquad \text{with} \qquad s = \pm\frac{1}{2}. \tag{1.13}$$

From the quantization of the energy spectrum, the 2DES density of states which is constant at zero magnetic field (see equation (1.2)), becomes discretized at high field:

$$D(\varepsilon) = n_L\sum_{n,s}\delta(\varepsilon - \varepsilon_{n,s}) \tag{1.14}$$

with n_L the spin-resolved Landau level degeneracy given by

$$n_L = \hbar\omega_c D_0 = \frac{e}{h}B. \tag{1.15}$$

In magnetic field it is convenient to describe the properties of the 2DES by a filling factor ν. This dimensionless parameter is defined as the number of occupied Landau levels at a specific value of magnetic field and for a certain electron concentration:

$$\nu \equiv \frac{n_s}{n_L} = \frac{h}{eB}\cdot n_s. \tag{1.16}$$

The filling factor tells how many magnetic flux quanta $\Phi_0 = h/e$ are present for each electron of N_s electrons contained inside an area of $L_x\cdot L_y$ size crossed by a total magnetic flux of $\Phi = BL_xL_y$:

$$\nu \equiv \frac{h}{eB}\cdot n_s = \frac{n_s L_x L_y}{BL_x L_y e/h} = \frac{N_s}{\Phi/\Phi_0}. \tag{1.17}$$

---

[v] For example at $B = 1$ T, $l_B \sim 26$ nm and at $B = 10$ T, $l_B \sim 8$ nm. This length gives an idea on the spatial extension of the wave function since its radius is $R_n = l_B\sqrt{2n+1}$.

[vi] For the GaAs material, the cyclotron energy $\hbar\omega_c$ changes as 1.75 meV/T.

1.5. Effect of electric field on the Landau levels

The effect of an electric field E can be included to the Landau level quantization due to magnetic field. Treatement of the electric field is relevant in electronic transport since it determines the current density. For instance if a homogeneous Hall electric field $E = -dV(y)/dy$ exists in the y direction, equation (1.10) leads to

$$\left[\frac{(\hbar k_x - eBy)^2 - \hbar^2 \partial^2/\partial y^2}{2m^*} - eEy \right] \varphi_n(y) = \varepsilon_n \varphi_n(y). \qquad (1.18)$$

The eigenvalues of the system are shifted to

$$\varepsilon_n = \hbar\omega_c \left(n + \frac{1}{2} \right) - \frac{m^* E^2}{2B^2} + eY \cdot E, \qquad (1.19)$$

and the energy of the Landau levels are not anymore constant in the y direction but proportional to the center coordinate Y. In this situation, Landau levels are tilted along this direction. Each electron in the new eigenstate system $\{\chi_k(x) \otimes \varphi_n(y)\}$ expressed as $\{|n, k_x\rangle\}$ has a drift velocity due to $\vec{E}$:

$$v_D = \frac{1}{m^*} \langle n, k_x | (-i\hbar\nabla + e\mathbf{A})_{\mathrm{x}} | n, k_x \rangle = \frac{1}{m^*} \langle n, k_x | -i\hbar\partial/\partial x - eBy | n, k_x \rangle = \frac{E}{B}, \quad (1.20)$$

which is independent of the state. As all electrons behave in the same way, the current density j_x may be written as $j_x = -en_s v_D$. Using equation (1.20), the current density depends on the variation of the electrostatic field with a weight which is related to the local occupancy of the Landau levels:

$$j_x = -en_s \frac{-1}{B} \frac{\partial V(y)}{\partial y} = -\nu \frac{e^2}{h} \frac{\partial V(y)}{\partial y} = \nu \frac{e^2}{h} E. \qquad (1.21)$$

In the special case of a homogeneous electric field, the current distribution is uniform. In high magnetic field, it may happen that $\partial V(y)/\partial y$ changes along the y-direction and the distribution of current becomes inhomogeneous (see section 1.8).

1.6. Bulk and edge model for the QHE

1.6.1. Bulk picture

The bulk description of the QHE starts from the necessity to include a certain disorder to understand why broad plateaus in the Hall resistance appear. The bulk model is based on the existence of extended and localized states in the infinite 2DES [18]. The extended state has a finite amplitude at every point in the sample whereas the localized state has a finite amplitude in only a small region of the sample [19]. At $B = 0$ and $T = 0$, the scaling theory of

localization [20] predicts the absence of extended states in disordered 2DES : all electrons are diffused by the impurities, interfere and become localized in regard to scaling theory [21]. With a longitudinal conductivity $\sigma_{xx} = 0$ driven by the electron mobility at the Fermi energy, the system is an Anderson insulator. In high magnetic field, the situation is slightly different since the 2DES density of state is quantized in Landau levels - i.e. only certain cyclotron orbits are allowed (see section 1.4) and localization is dominated by the quantum hopping of cyclotron motions. Impurities, defects and inhomogeneities contribute to random potential fluctuations which lead to the broadening of the DOS around each of these Landau levels. The variation of magnetic field modifies the Landau level occupancy $n_L(B)$ (equation (1.15)) and the gap
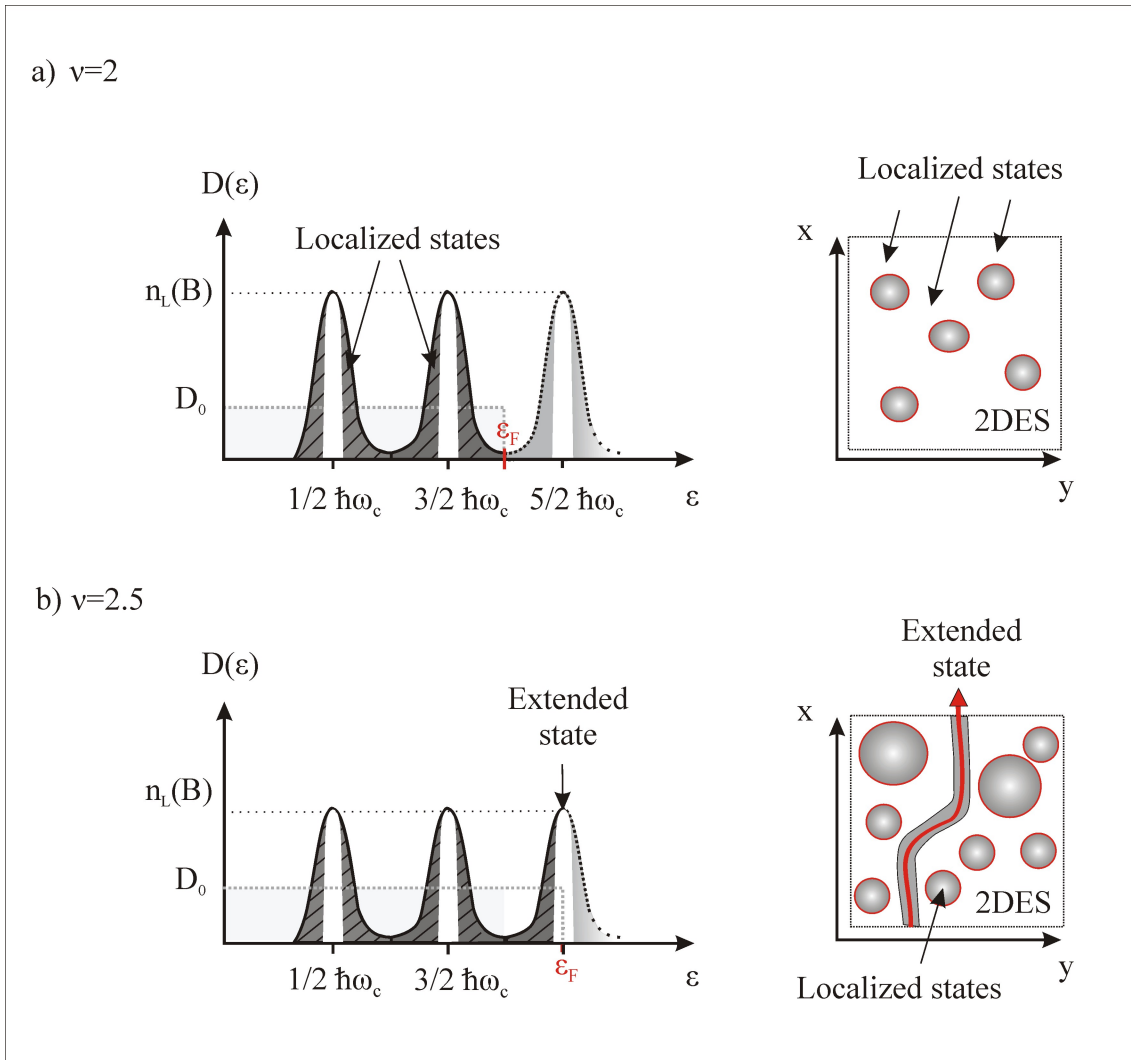
Figure 1.3.: **a)** Broadening Landau levels at $\nu = 2$. The states at the Fermi level are all localized. **b)** At $\nu = 2.5$, there is an extended state which carries current due to the percolation path.

energy $\hbar\omega_c = \hbar eB/m^*$. If the magnetic field is decreased, the Fermi energy changes from a gap region at $\nu = 2$ to a high density of states area such as $\nu = 2.5$. By percolation, an extended state exists at $\nu = 2.5$ which goes from one boundary of the sample to the other (Fig. 1.3(b)). At contrary, electrons with an energy in the tail of the Landau level describe a close trajectory around close equipotential line (Fig. 1.3(a)). They are localized. In consequence, the impurities decrease the number of states which may carry the current. The net current is nevertheless conserved since the density current near impurities increases due to the potential gradient. In average, the excess current carried by extended state compensates the lack of state due to the localization [22]. A plateau appears in the quantum Hall regime since the localized states are filled up without changing the extended state, i.e. without changing the conductance [23] when the density increases or the magnetic field decreases. These localized states may be seen as a reservoir which allows the Fermi energy to stay inside the Landau gap and far away from extended state.

1.6.2. Edge state picture

Another description of the QHE is based on the edge states picture elaborated by Marcus Büttiker [24–26]. Before explaining what is the edge state, it is necessary to start with the main idea of his transport model. It is not a linear response theory based on Kubo-formula [vii] but it follows the Landauer approach [viii] in which the conduction is treated in terms of transmission

---

[vii] The transport theory was first described via built up current due to an applied electric field. Its formalism is based on linear response and Kubo formulas. By applying a difference of voltage to the sample, an electric field is created which induces a current density inside the conductor: $j(r) = \int dr'\sigma(r,r') \cdot E(r')$. This equation gives a proportional relation (an approximation of the linear response) expressed via a function $\sigma(r,r')$. For a system invariant by translation, $j = \sigma \cdot E$ with $\sigma = V^{-1} \int dr dr' \sigma(r,r')$. The conductivity, σ appears as an intrinsic property of the sample which does not depend on the position of the voltage carrying contacts or the sample geometry. This conductivity should not be confused with the conductance G which is the measured quantity in experiments.

[viii] R. Landauer introduced a new conductance theory for close systems. The applied current is kept constant and creates local electric fields inside the sample. His theory has the advantage that it can be easily adapted to the quantum theory and its interference effects since the Landauer approach is based on a probability of transmitted and reflected electron (analogy with optic wave propagation). The resistance is due to the local electrostatic potential induced by scattering events under neutrality condition. In the presence of current transport, electrons are accumulated on one side of a scatter whereas a lack of electron appears on the other side. A dipole is formed and a local resistance is associated to the potential change around the impurities. A simple consideration gives [27–29]:

$$R = \frac{\pi\hbar}{e^2}\frac{R}{T}. \tag{1.22}$$

The debat concerning the R/T or $1/T$ expression of the resistance is well explained in the book of Imry [30] (see also [31, 32]). To summarize, both equations are in principle valid, but it is the matters of the measuring configurations: $R_{4\text{pts}} = \frac{\pi\hbar}{e^2}\frac{R}{T}$ is for a four-terminal resistance while $R_{2\text{pts}} = \frac{\pi\hbar}{e^2}\frac{1}{T} = \frac{\pi\hbar}{e^2}\left(1 + \frac{R}{T}\right) = R_{4\text{pts}} +$

and reflection of electron.

Marcus Büttikker extends the Landauer approach to open systems by inserting contact terminals [33]. The source contact injects charges (I_{net}) to the conductor and the sink contact removes charges ($-I_{net}$) from it. The voltage probes carry no net current ($I_{net} = 0$). The electrons of a terminal j distributed inside one-dimensional channels N_j have a certain probability T_{ji} to go from terminal j to i, and a probability R_{jj} to be reflected. Through the set of equations

$$I_j = \frac{e}{h} \left[(N_j - R_{jj}) \cdot \mu_j - \sum_{i \neq j} T_{ji} \cdot \mu_i \right],$$ (1.23)

for each contact j, it is possible to calculate all the chemical potentials μ_j and to obtain all the resistance $R_{ij,kl} = (V_k - V_l)/e \cdot I_{net}$. In this particular case, the current is applied between the terminal i and j, and the voltages V_k and V_l are probed between k and l.

In the quantum Hall regime, the channels are edge states which are associated in the classical view to the center of the electron skipping orbit in magnetic field. What is meant by edge states ? In high magnetic field, the density of state is quantized in Landau levels (LLs) which bend up at the mesa edges due to the potential confinement (see Fig. 1.4(b)). Around bulk integer filling factors, the Fermi energy lies inside the gap of the bulk area but it crosses the LLs at the mesa edges. At these intersections, extended states [ix] exist at the Fermi level which connects one terminal to the other with probability $T_{ij} = 1$ in the conventional QHE (Fig. 1.4(a)). Due to different sign of the slope of the energy distribution, the direction for the drift velocity is opposite at the two edges (see arrows location in Fig. 1.4(a)). The spatial separation of the conductive channels with the insulation bulk in between suppresses the backscattering from one edge of the mesa to the opposite one. States with different direction of electron propagation are decoupled. Voltage probing contacts located at the same edge own the same chemical potential defined either by the injecting or the sinking contact depending on the magnetic field sign (the skipping orbit effect). Under such a condition the longitudinal resistance is zero and the Hall resistance is quantized with a value proportional to h/e^2 and inversely proportional to the number of Landau level.

With his edge state picture, M. Büttikker describes open systems by including contacts and explains the quantum Hall effect by assuming no backscattering. This picture is a simple single particle picture which does not include electron-electron interaction and does not describe microscopically the QHE even if its formalism is proper. The limitation of this description is marked by its author [34]:

> "The above discussion cannot be used to find the current densities inside the sample: like true charge densities are found only with the help of Poisson's equations,

---

$2R_{\text{contact}}$ includes the contact resistance $R_{\text{contact}} = \frac{\pi \hbar}{2e^2}$ and corresponds to a two-terminal resistance.

[ix] These extended states should not be confused with the extended state of the bulk picture corresponding to a percolation path at half integer filling factors.
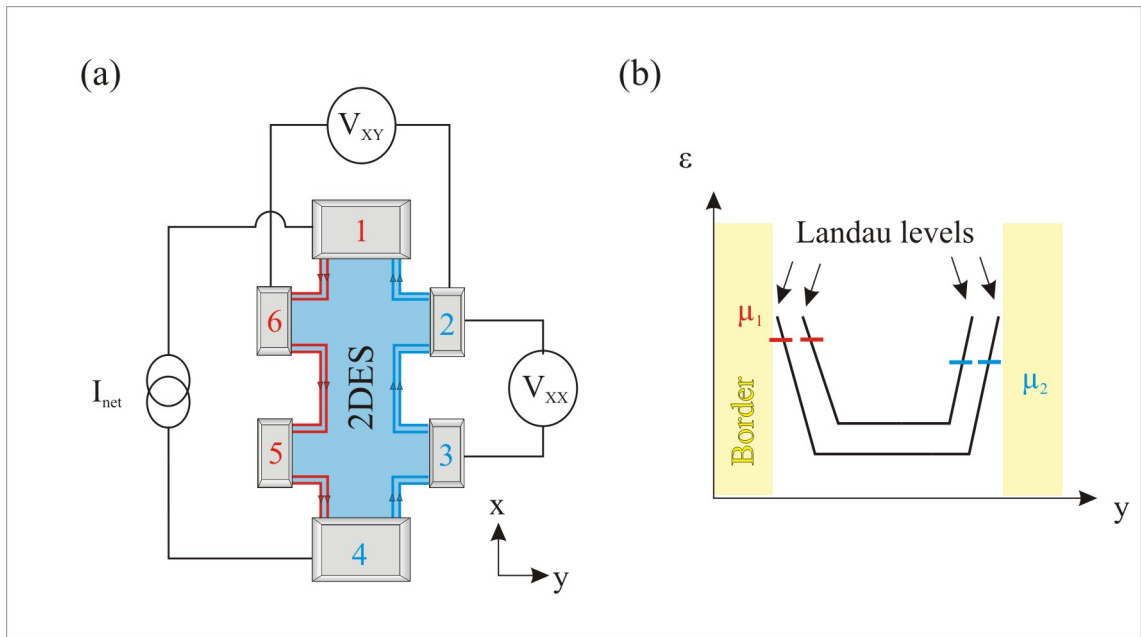
Figure 1.4.: **a)** Hall bar at $\nu = 2$ with two edge states on each side of the mesa. **b)** Energy spectrum in a cross-section view showing the Landau levels bending at the mesa edges.

> *the true current distribution must be found from a self-consistent analysis [35, 36] (which determines the Hall potential)."*

M. Büttiker *et al.*, Physica E 35, p. 33 (2003).

The approach proposed by S. Komiyama and H. Hirai [36] includes only at the first order the effect of the electrostatic potential inside the edge state picture.

1.7. Compressible and incompressible strips in the depletion region of a 2DES

1.7.1. Electrostatic model from Chklovskii, Shklovski, and Glazman (CSG)

All the pictures presented in the previous sections omit an important ingredient: the electrostatic screening of the potential due to the electron-electron interaction. This effect is known to change drastically the microscopic properties of the 2DES by avoiding large variation of the electron density. First theoretical works from S. Luryi [37] and A.L. Efros [38] on inhomogeneous 2DES bulk show that the screening at high magnetic field splits the 2DES into

compressible and incompressible regions due to the Landau gap in the density of states. The compressible region is a region with a high density of states at the Fermi energy which allows a redistribution of the electrons and induces a perfect screening of the electrostatic potential. The incompressible region behaves like an insulator with the Fermi energy inside the energy gap and therefore with poor screening properties [x]. At the edges of Hall bar, screening effect of the electrostatic potential has specially to be included otherwise the electron density in high magnetic field will have an unrealistic step-like profile with a large B-dependent dipole charges. Such unrealistic situation comes from the edge state picture and it is illustrated at $\nu = 2$ in figure 1.5(b) and (c). The electron density at the mesa edges jumps from $2n_L$ to n_L due to the potential confinement since only one Landau level is left when the second Landau level cross the constant electrochemical potential $\mu_{\text{elch}} = \mu_{\text{ch}}(n_{\text{s}}) - eV_{\text{conf}}$. To go from one Landau level to the second one, the electrons should give a large chemical potential energy of $\hbar\omega_c$. C.W.J. Beenakker [39] and A.M. Chang [40] applied qualitatively the compressible and incompressible picture of S. Luryi and A.L. Efros to the edge state picture of M. Büttiker. They associated the extended edge states to compressible strips separated in between by incompressible strips. The description of the edges in terms of these compressible and incompressible strips was similar for the two authors but their interpretations concerning the current flow were drastically diverge. C.W.J. Beenakker assumed that the current is flowing inside the compressible strips. On the other side, A.M. Chang argued that the compressible strips cannot carry a net current due to the perfect screening of the electrostatic potential inside these strips, only the incompressible strips in which $\nabla V \neq 0$ propagate current.

In 1992, Chklovskii, Shklovski and Glazman (CSG) analytically and quantitatively calculate the electron density and the electrostatic potential of a 2DES confined by split gates [41]. Their electrostatic approach, which includes the non linear screening effect occurring at high magnetic field, describes one 2DES edge [xi] with its inhomogeneous electron density [42]. They used a one dimensional model for the 2DES and the screening is assumed to be perfect - i.e. $V = 0$ if the 2DES is present. In the first step, they determine the electron density profile $n_s(y)$ at $B = 0$ by solving the electrostatic Laplace equation with defined boundary conditions: $V(y) = V_g$ at the gate position ($y < -l$) and $V(y) = 0$ at the 2DES position ($y > l$). For $y > l$, the electron

---

[x] The screening length defined by

$$\lambda_s = \frac{4\pi\epsilon_0\epsilon}{e^2}\frac{\partial\mu_{\text{ch}}}{\partial n_s}, \qquad (1.24)$$

is a relevant parameter to describe these two different regions: λ_s is zero for compressible region (perfect screening i.e. metal-like behavior) but infinite for incompressible region (insulator-like).

[xi] Later, the model is extended to the gate-confined narrow channel [42]. The treatment of both edges is important to analyze the current distribution.

density profile at one edge has a half-domelike shape if $T = 0$ and $B = 0$:

$$n_s(y) = n_0 \cdot \sqrt{\frac{y - l}{y + l}} . \tag{1.25}$$

n_0 is the density of the homogeneous positive background charges and $2l$ the electron depletion length at the mesa edge. The smooth electron density profile $n_s(y)$ at $B = 0$ will determine the position of the incompressible strips in high magnetic field since such profile is nearly conserved at high magnetic field (the Landau gap is assumed to bring small perturbation). The results for the potential and electron density at the mesa edge are shown in figure 1.5 (e) and (f). Far away from the edge in the bulk region, the 2DES is compressible with two and half levels occupied ($\nu = 2.5$): the electron density changes smoothly and the potential is flat since
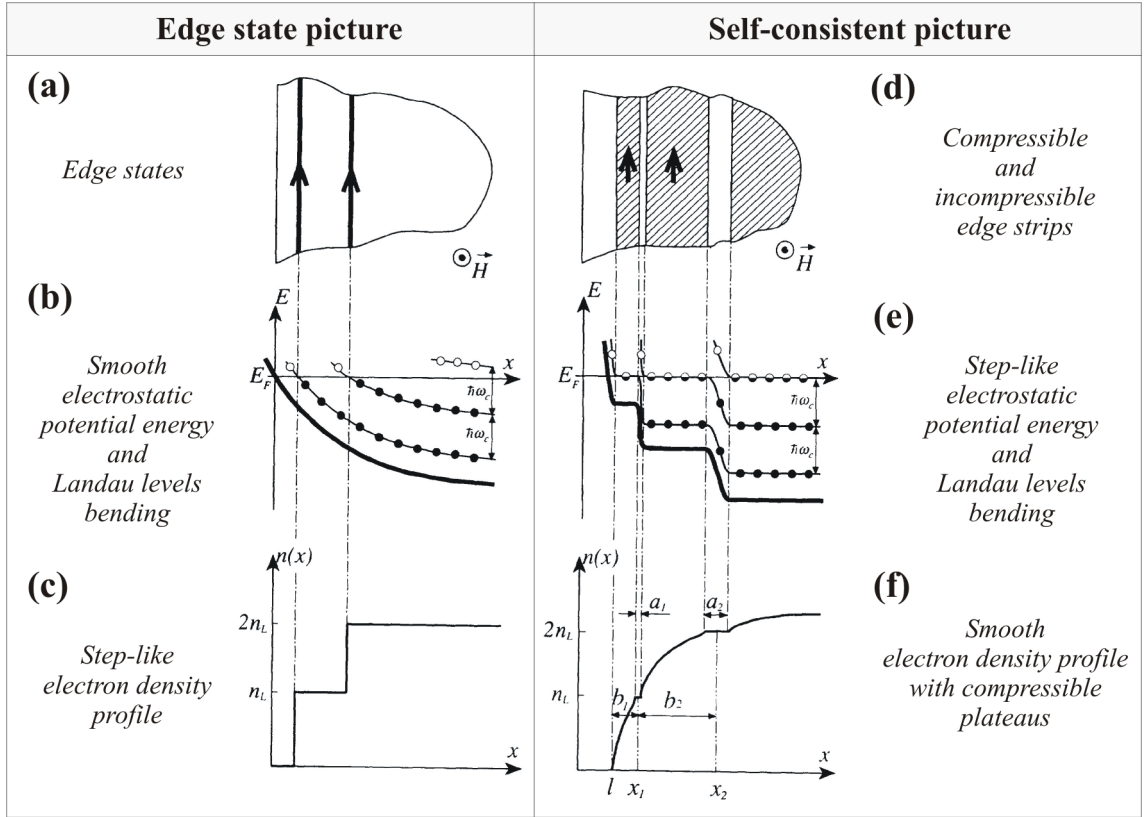
Figure 1.5.: Single particle picture versus electrostatic approach (adapted from [41]). **a-c)** *Edge state picture*. Under high magnetic field extended edge states conduct current at the mesa edge (a). These states are located at the crossing between the Landau levels and the Fermi energy (b). The density profile is step-like (c). **d-f)** *Self-consistent picture*. The 2DES edge consists of compressible (CS) and incompressible strips (IS) (d). The potential is flat inside CS and varies in IS (e). Smooth electron density profile with flat region at the IS position (f).

there is no confinement potential ($V_{\text{conf}} = 0$). Coming closer to the edge, confinement potential is present ($V_{\text{conf}} \neq 0$) and the electron density for energetically reason prefers to stay quantized at $n_s = 2n_L$ for a certain width. The confinement is therefore not screened and the energy of the Landau level increases. This increasing occurs until the higher Landau level (number two in the picture) reaches the electrochemical potential level. At this stage, the electronic state at the Fermi level becomes again compressible: the potential of confinement is perfectly screened. The electron density starts to decrease until a new incompressible region is recovered, i.e. $n_s = n_L$.

Chklovskii, Shklovski and Glazman quantitatively calculated the position of the pth incompressible strip via the equation $n(y_p) = p \cdot n_L$. They obtained

$$y_p = l \cdot \frac{\nu^2 + p^2}{\nu^2 - p^2} \,. \tag{1.26}$$

They also shows that the width of the incompressible strips a_p are much narrower than the compressible ones. The width of the pth incompressible strip is given by

$$a_p^2 = \frac{16\epsilon\epsilon_0\hbar\omega_c}{\pi e^2} \cdot \left(\frac{dn_s}{dy_{y=y_p}}\right)^{-1} \,. \tag{1.27}$$

For strips in between two spin splitting Landau levels, $\hbar\omega_c$ has to be replaced by $g^*\mu_B B$. Following this equation, a smooth variation of potential dn_s/dy will give a broad incompressible strip. This result will be used in the last chapter 6 of this PhD thesis.

1.7.2. Self-consistent approach

The approach of Chklovskii, Shklovski and Glazman is an electrostatic calculation which does not include the electrochemical equilibrium condition and the effect of finite temperature. Moreover this approach fails to determine the current distribution. Further theoretical works have been done in these directions by R.R. Gerhardts and coworkers [4, 5, 43–45]. For instance, K. Lier and R.R. Gerhardts [44] proposed a numerical but quantitative self-consistent calculation. They keep the CSG electrostatic approach to obtain the potential profile (analytic treatment of the Poisson equation gives the potential seen by the 2DES in term of a certain electron density n_s). However they used the local Thomas Fermi approximation to self-consistently determine the density in thermal equilibrium:

$$n_s^{\text{TFA}}(y) = \int d\varepsilon D(\varepsilon) f(\varepsilon - \mu_{\text{elch}} - e \cdot V(y)) \,. \tag{1.28}$$

At $T = 0$, the Fermi-Dirac distribution is $f(\varepsilon - \mu_{\text{elch}} - e \cdot V(y)) = \theta(\varepsilon_F - \varepsilon + e \cdot V(y))$ and at $B = 0$, the density of states is $D(\varepsilon) = D_0\theta(\varepsilon)$. It follows:

$$n_s^{\text{TFA}}(y) = D_0[\varepsilon_F + e \cdot V(y)]\theta(\varepsilon_F + e \cdot V(y)) \,. \tag{1.29}$$

The magnetic field is then included via the DOS:

$$D(\varepsilon) = \frac{1}{\pi l_{\mathrm{B}}^2} \sum_{n=0}^{\infty} \theta\left(\varepsilon - \hbar\omega_{\mathrm{c}}(n + \frac{1}{2})\right) . \qquad (1.30)$$

Results of K. Lier and R.R. Gerhardts does not show a large quantitative difference from CSG calculation but the existence of compressible and incompressible strips naturally appears. By avoiding the assumption of a perfect screening, the 2DES starts where the potential energy crosses the electrochemical potential energy level as it should be in equilibrium condition [xii]. In consequence, the determination of the compressible and incompressible strip's position is relevant. Their approach allows also to include temperature effect: the potential inside compressible strip is not zero but linearly varies by an amount of $k_{\mathrm{B}}T$ while the width of incompressible strips is thinner under finite temperature and broader if the temperature goes to zero [xiii].

1.8. Scanning Force Microscopy gives Hall potential distribution

A cryogenic $(1.4\,\mathrm{K})$ scanning force microscope working at high magnetic field (Fig. 1.6(a)) has already demonstrated its ability to provide the Hall potential profiles of 2DES embedded few tens of nanometers below the surface [1–3, 46–49]. The measurement of potential variation allows us to obtain a microscopic picture of the integer quantum Hall effect. For the integer quantum Hall effect developed inside a $50\,\mathrm{m}^2/\mathrm{Vs}$ mobility Hall bar, the Hall potential linearly varies across the sample width (profile I). Such a linear profile is similar to a classical Hall regime. Entering the Hall plateau from high magnetic fields, the profile type II is found for the filling factors between $\nu = 1.96$ and $\nu = 2.04$. In this profile, the potential variation is exclusively distributed in the bulk. Above $\nu = 2.04$ (profile III), the Hall potential shows an equal drop at the two edges of the mesa. The potential is flat in the mesa bulk with an intermediate value, however it starts to show a slope with increasing filling factor.

Figure 1.7 shows the Hall potential distribution for a broader magnetic field range covering several integer filling factors. The color scale illustrates the strength of the Hall potential: blue for low and red for high potential. The plots of the Hall and longitudinal resistance are added to provide a direct comparison between the macroscopic transport and the microscopic information obtained from the local potential distribution. A clear correspondence between transport and potential distribution is visible since the same Hall potential profiles are recovered at around each integer filling factor. In addition, the three different profiles shown in figure 1.6(b) are found for each interval between two integer filling factors.

[xii] Indeed the depletion length $2l$ is calculated from the equality $V(2l) = \varepsilon_{\mathrm{F}}$.
[xiii] The width converges to the CSG value.

The location of Hall potential drops have been compared with the position of incompressible strips. The position of these drops corresponds to the position of the innermost incompressible strips (see Fig. 1.7(b)). As a consequence, the bias current which is driven by the potential gradient is expected to flow without dissipation along innermost incompressible strips. For the profile I, the bias current flows with an uniform distribution like in the classical Hall effect. For the profile II, the non dissipative current has a complex distribution inside the bulk area, which strongly depends on the scan position and magnetic field. For the profile III, the non dissipative current are equally distributed at the incompressible strips located at the edges. The figure 1.7(b) also shows how the innermost incompressible strip located at the mesa edges becomes the incompressible bulk when the center of the Hall plateau is approached (see section 1.9 for complement information). Further measurements performed close to the contact areas (see Fig. 1.8) reveal that the slope of the potential associated to the presence of the innermost incompressible strip is maintained along the borderline between 2DES and ohmic contacts which act as potential probes. Such voltage distribution clearly visible at $\nu = 2$ (Fig. 1.8(a)) is the result from a regular electron depletion in front of ohmic contacts [2].
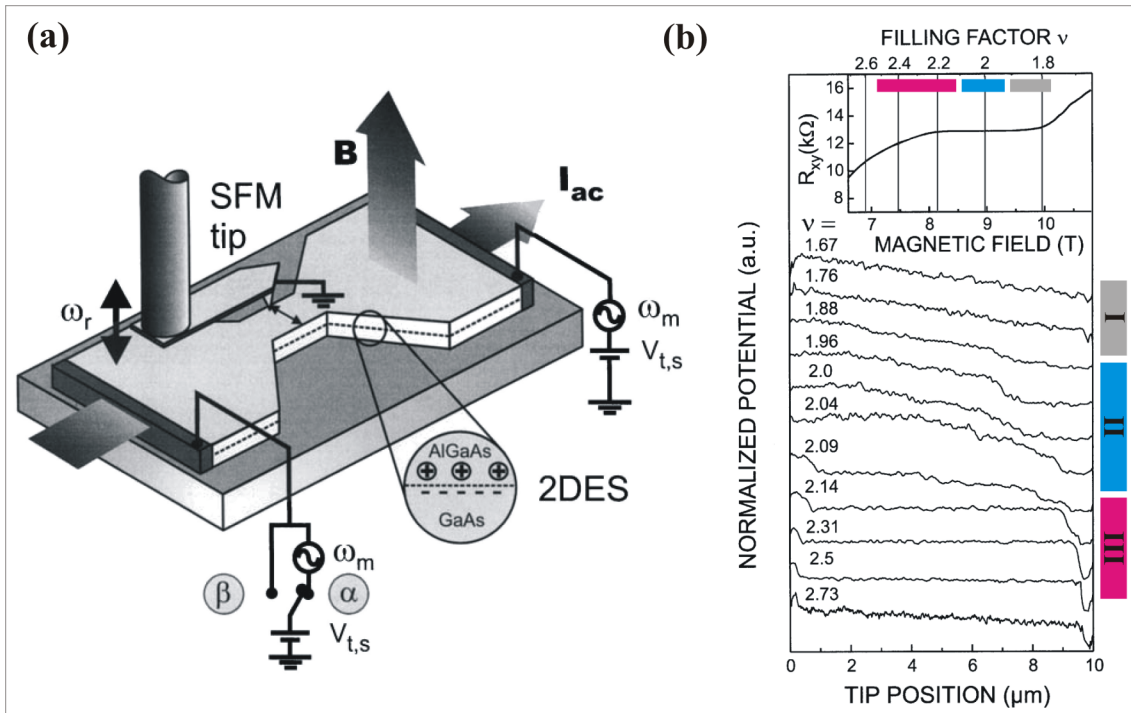
Figure 1.6.: Adapted from the PhD thesis of E. Ahlswede [3]. **a)** Sketch of the scanning force microscope above a 2DES Hall bar. **b)** Cross-section of the Hall potential distribution across a $10\,\mu$m wide Hall bar with a mobility of $50\,\text{m}^2/\text{Vs}$. Each plotted line is obtained at a different filling factor. Three types of Hall potential profile are visible (see text).
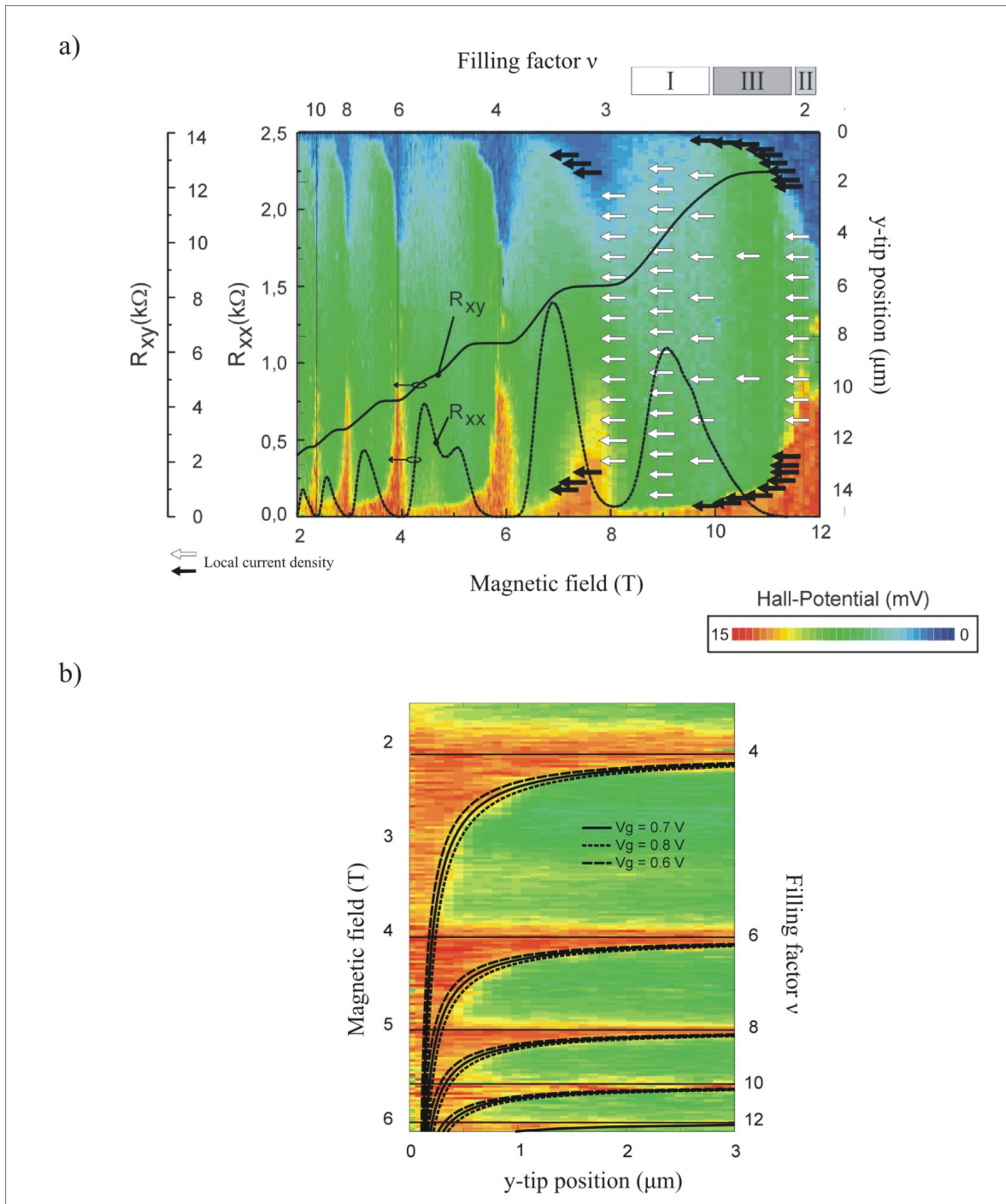
Figure 1.7.: Adapted from the PhD work of E. Ahlswede [3]. **a)** Hall potential profiles at various magnetic fields for a $50\,\mathrm{m^2/Vs}$ mobility Hall bar of 15 μm width. The Hall potential is high (red) at the lower mesa edge ($y = 0$) and low (blue) at the upper edge ($y = 15$). Together with the color plot of the potential distribution, the Hall and longitudinal resistance (R_{xx} and R_{xy} respectively) are added. The arrows represent the distribution of the biased current through the sample: for the profile III the non dissipative current is located at the mesa edge and for the profile II (i.e. for filling factor around the integer value) this current spread inside the bulk. **b)** Fit from equation (1.26) of the position of the innermost incompressible strips.
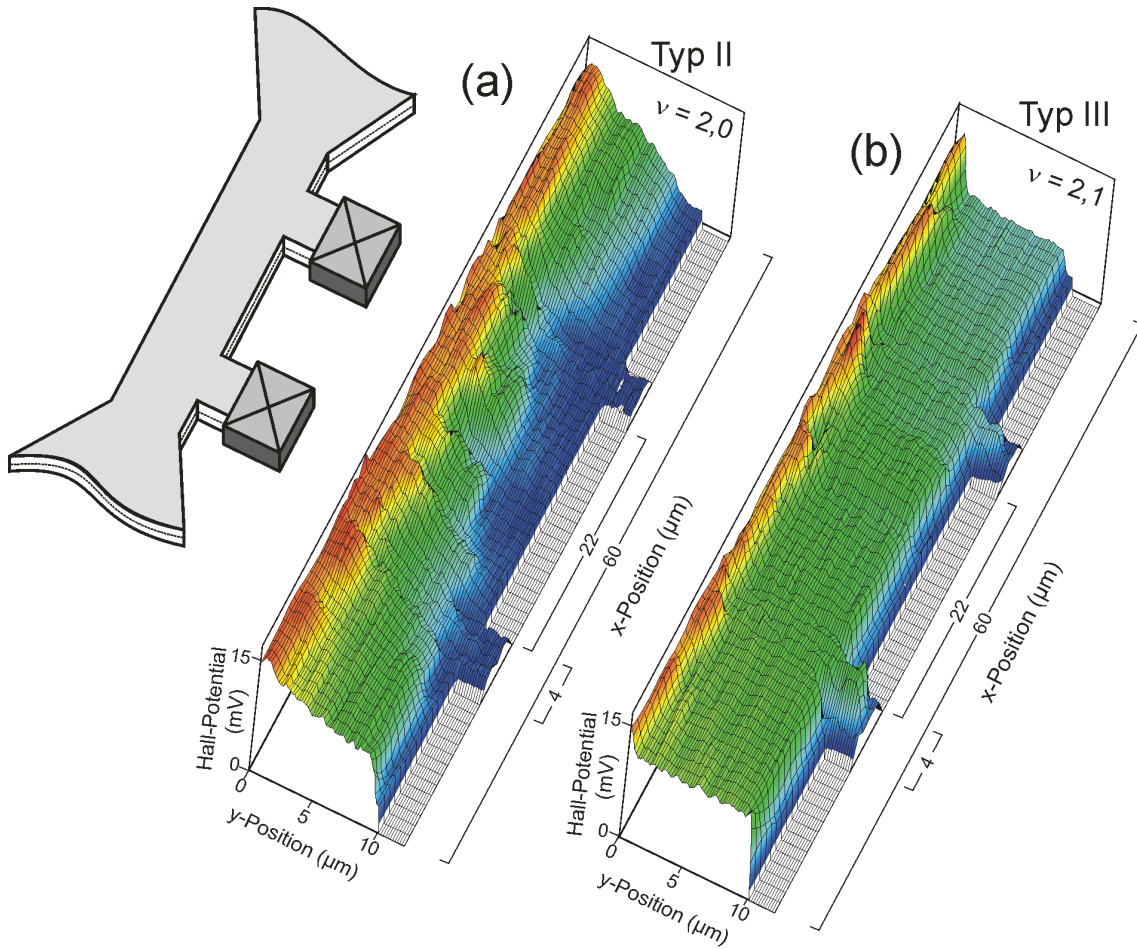
Figure 1.8.: Hall potential distribution at $\nu = 2$ (a) and $\nu = 2.1$ (b) in a four-terminal Hall bar with a mobility of $50\,\mathrm{m}^2/\mathrm{Vs}$. The incompressible strips (see the variation of the potential) are not transmitted into the voltage probing contacts. Adapted from E. Ahlswede PhD thesis [2].

Following the self-consistent approach, A. Siddiki [6] was able to simulate the Hall potential as shown in Fig. 1.9. Its calculated distribution is similar to what we describe in the section 1.8. To recover the three different profiles and the current distribution, the width of the wave function is included in a quasi-Hartree approximation. Errors due to Thomas-Fermi approximation are avoided. Non-local effects on the conductivity along incompressible strips are also simulated by a spatially averaging procedure [4]. This process allows to calculate the Hall and the longitudinal resistance as continuous functions of the magnetic field. The incompressible strips with perfect insulating properties appear to exist only at certain magnetic field intervals. In these intervals, the Hall resistance is found to be quantized. The simulation clearly shows how the QHE results from the possibility of the current to flow without dissipation inside incompressible strips. Note that from this theory, it is not necessary to include disorder. The disorder only broadens the Hall plateau in the higher magnetic field direction.
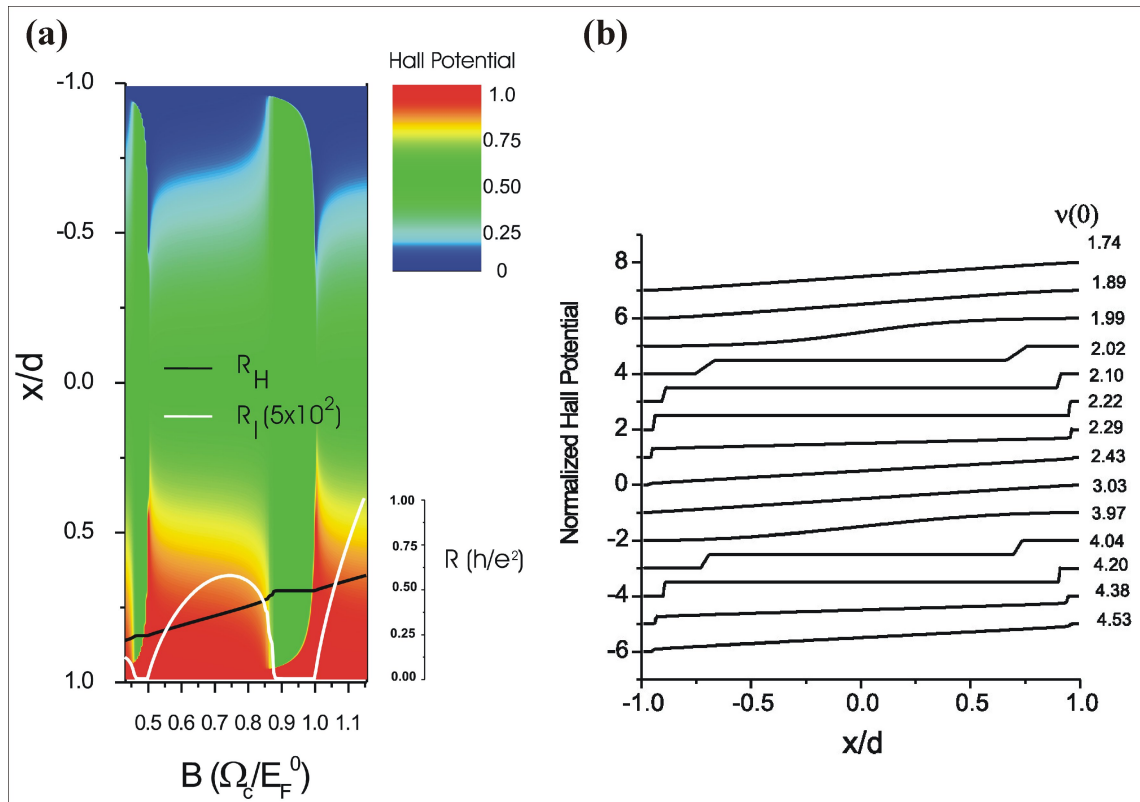
Figure 1.9.: Hall potential calculation adapted from A. Siddiki PhD thesis [6]. **a)** Color plot of scaled Hall potential. **b)** Cross-section view of the scaled Hall potential for selected values of magnetic field B.

1.9. The present microscopic picture of QHE

A picture of the QHE based on compressible and incompressible strips follows from the self-consistent theory and experiment shown in the previous sections [17]. The present section describes the distribution of these strips along the four-terminal Hall bar as a function of the filling factor. Their evolution due to the change of the magnetic field is treated via the presentation of three situations with different bulk filling factors [xiv]: $\nu = 3$, $\nu = 2.5$ and $\nu = 2$ (see Fig. 1.10). All compressible areas are drawn with a gray color which symbolizes an arbitrary fixed electrochemical potential in the equilibrium situation (the electrochemical potential is the same everywhere). Depending on the electron density variation, compressible and incompressible strips follow the shape of the Hall bar boundaries. As shown in figure 1.8, the strips do not enter to the contacts since the electron density at this area is lower than that at the bulk area [xv].

For integer filling factor $\nu = 2$ and $\nu = 3$, the bulk is mainly incompressible (white) with a constant electron density. Compressible droplets in the incompressible bulk are also added in order to include disorder and its associated fluctuations of potential. When the average value of the bulk filling factor reaches $\nu = 2.5$, the bulk becomes compressible (gray) with a flat density profile (see the cross section of the electron density shown at the right side in Fig. 1.10(b)). Closer to the mesa border the drop of the electron density associated to the potential confinement induces an alternate of compressible and incompressible strips. Each time the electron density corresponds to an integer number of completely filled Landau level, an incompressible strip exists. For instance in Fig. 1.10(a), two incompressible strips (white lines) on each mesa border and one large incompressible bulk (white area in the mesa center) corresponds to $\nu = 3$. Note that the self-consistent theory of R.R. Gerhardts et al. predicted that the inner compressible strips are too thin to survive a spatially averaging procedures mimicing a finite extension of the wavefunction.

By increasing the magnetic field (i.e. decreasing the bulk filling factor) the cyclotron gap between Landau levels is enlarged and the degeneracy of these energy levels is enhanced. The redistribution of the charges in this new energy profile drives the evolution of the compressible and incompressible areas. From $\nu = 3$ to 2.5, the bulk transits from an insulator-like incompressible phase with the Fermi energy in the Landau gap to a metal-like compressible phase with the Fermi energy inside the Landau level. The thickness of the strips at the two mesa edges get broader (see Fig. 1.10(b)).

[xiv] The bulk filling factor ν refers to the measured bulk density of the Hall bar.

[xv] Such a regular electron depletion at the interface between the 2DES and the alloyed contacts might be explained by a difference of work-function between the metallic contact and the 2DES.
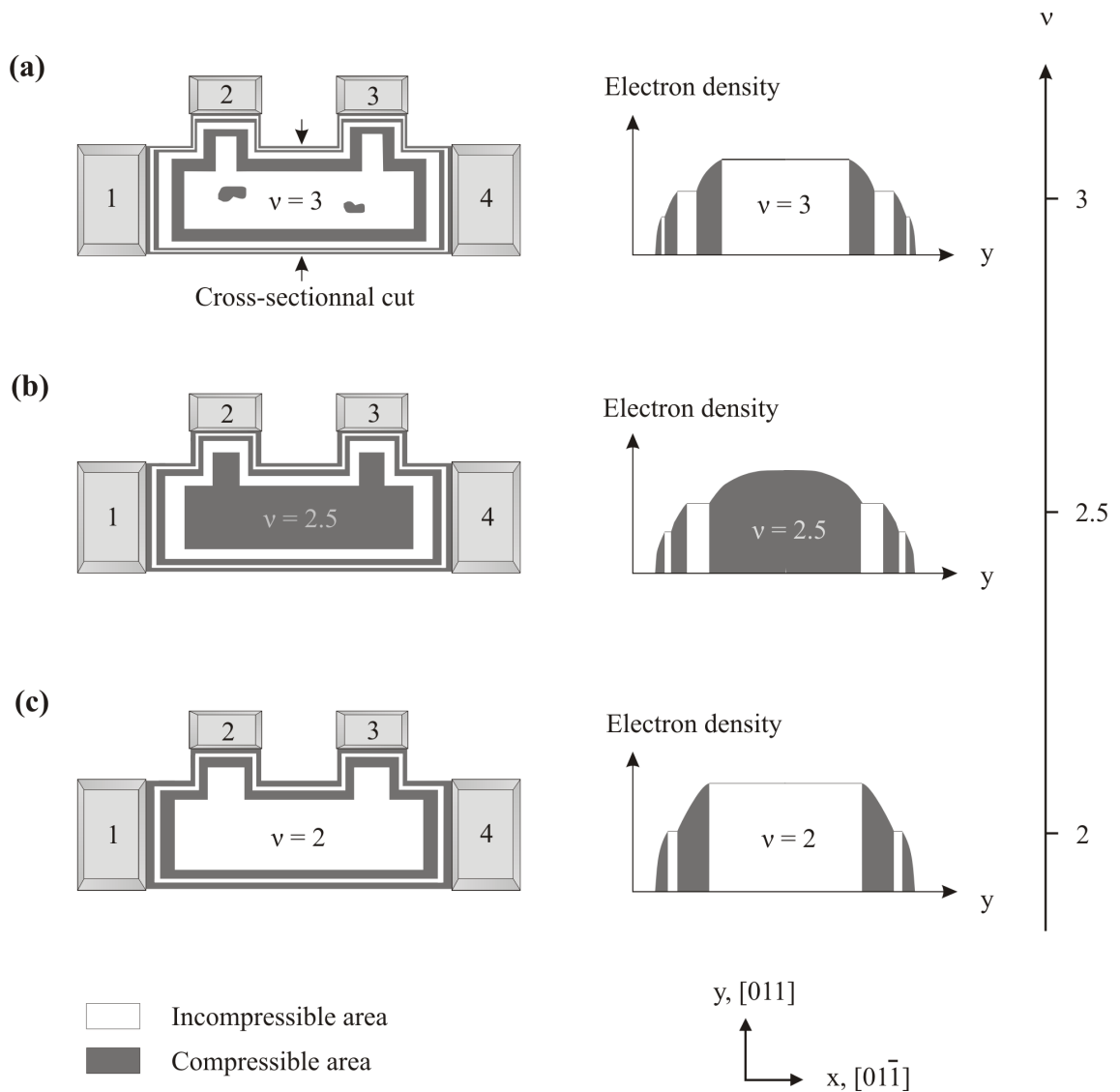
Figure 1.10.: **a-c)** Qualitative picture showing the distribution of the incompressible (white) and compressible (gray) strips in 2DES in a four-terminal Hall bar for $\nu = 3$ to $\nu = 2$. The schematics on the right side depict the corresponding cross-section of the electron density profiles along the sample's width.

1.10. Conclusion

The microscopic description of the quantum Hall effect has changed the last years thanks to local Hall potential probing [17]. With perfect agreement with self-consistent calculations, the measurements have triggered a microscopic picture of the quantum Hall effect which is based on compressible and incompressible strips instead of the single particle edge states picture. Some points stay under investigation. For instances, how to include the effect of the electron depletion in front of alloyed contacts in this self-consistent picture ? What is the effect of the spin on the strips distribution [xvi] ? Is it possible and how to adapt the compressible and incompressible picture to the fractional quantum Hall effect or to its breakdown ? This PhD thesis will focus on how the compressible and incompressible strips picture explains the observation of adiabatic transport features in the quantum Hall regime and their corresponding potential distributions.

Bibliography

[1] E. Ahlswede, P. Weitz, J. Weis, K. Klitzing, and K. Eberl, Physica B **298**, 562 (2001).

[2] E. Ahlswede, P. Weitz, J. Weis, K. Klitzing, and K. Eberl, Physica E **12**, 165 (2002).

[3] E. Ahlswede, Potential- und Stromverteilung beim Quantum-Hall-Effekt bestimmt mittels Rasterkraftmikroskopie, PhD thesis, Max-Planck-Institut für Festkörperforschung / University of Stuttgart (2002).

[4] A. Siddiki and R. Gerhardts, Phys. Rev. B **70**, 195335 (2004).

[5] A. Siddiki and R. Gerhardts, Phys. Rev. B **68**, 125315 (2003).

[6] A. Siddiki, Model calculation of current and density distributions in dissipative Hall bar, PhD thesis, Max-Planck-Institut für Festkörperforschung / University of Würzburg (2005).

[7] T. Ando, A. Fowler, and F. Stern, Rev. Mod. Phys. **54**, 437 (1982).

[8] K. Klitzing, G. Dorda, and M. Pepper, Phys. Rev. Lett. **45**, 494 (1980).

[9] N. Aschcroft and N. Mermin, *Solid state physics* (Saundres College, Orlando, 1976).

[10] D. Tsui, Rev. Mod. Phys. **71**, 891 (1999).

[11] D. Tsui, H. Störmer, and A. Gossard, Phys. Rev. Lett. **48**, 1559 (1982).

[12] H. Störmer, Rev. Mod. Phys. **71**, 875 (1999).

[xvi] Some works on the exchange energy have been done in this direction with a density functional approach [50,51].

[13] R. Laughlin, Rev. Mod. Phys. **71**, 863 (1999).

[14] R. Laughlin, Phys. Rev. Lett. **50**, 1395 (1983).

[15] K. Klitzing, Physica B **184**, 1 (1993).

[16] T. Ando, Physica B **201**, 331 (1994).

[17] K. Klitzing, R. Gerhardts, and J. Weis, Physik Journal **4**, 37 (2005).

[18] B. Huckestein, Rev. Mod. Phys. **67**, 357 (1995).

[19] B. Kramer and A. MacKinnon, Rep. Prog. Phys. **56**, 1469 (1993).

[20] E. Abrahams, P. Anderson, D. Licciardello, and T. Ramakrishnan, Phys. Rev. Lett. **42**, 673 (1979).

[21] P. Lee and T. Ramakrishnan, Rev. Mod. Phys. **57**, 287 (1985).

[22] R. Prange and S. Girvin, *The quantum Hall effect* (Springer, address, 1987).

[23] R. Prange, Phys. Rev. B **23**, 4802 (1981).

[24] M. Büttiker, Semiconductors and semimetals **35**, 191 (1992).

[25] M. Büttiker, Phys. Rev. B **38**, 9375 (1988).

[26] J. Davies, *The physics of low dimensional semiconductors* (Cambridge University Press, Cambridge, 1998), Chap. 9.

[27] R. Landauer, IBM J. Res. Develop. **1**, 233 (1957).

[28] R. Landauer, IBM J. Res. Develop. **32**, 306 (1988).

[29] R. Landauer, IBM J. Res. Develop. **44**, 251 (2000).

[30] Y. Imry, *Introduction to mesoscopic physics* (World Scientific Press, Singapour, 1986).

[31] Y. Imry, in *Physics of mesoscopic systems*, edited by G. Grinstein and G. Mazenko (World Scientific, Singapore, 1986), Vol. 45, p. 101.

[32] A. Stone and A. Szafer, IBM J. Res. Develop. **32**, 384 (1988).

[33] M. Büttiker, Y. Imry, R. Landauer, and S. Pinhas, Phys. Rev. B **31**, 6207 (1985).

[34] M. Büttiker, P. Samuelsson, and E. Sukhorukov, Physica E **20**, 33 (2003).

[35] T. Christen and M. Büttiker, Phys. Rev. B **53**, 2064 (1996).

[36] S. Komiyama and H. Hirai, Phys. Rev. B **54**, 2067 (1996).

[37] S. Luryi, edited by G. Landwehr (Springer, Berlin, 1988), Vol. 71, p. 16.

[38] A. Efros, Solid State Communications **67**, 1019 (1988).

[39] C. Beenakker, Phys. Rev. Lett. **64**, 216 (1990).

[40] A. Chang, Solid State Communications **74**, 871 (1990).

[41] D. Chklovskii, B. Shklovskii, and L. Glazman, Phys. Rev. B **46**, 4026 (1992).

[42] D. Chklovskii, K. Matveev, and B. Shklovskii, Phys. Rev. B **47**, 12605 (1993).

[43] A. Siddiki and R. Gerhardts, Phys. Rev. B **67**, 115327 (2003).

[44] K. Lier and R. Gerhardts, Phys. Rev. B **50**, 7757 (1994).

[45] J. Oh and R. Gerhardts, Phys. Rev. B **56**, 13519 (1997).

[46] K. McCormick, M. Woodside, M. Huang, M. Wu, P. McEuen, C. Duruoz, and J. Harris, Phys. Rev. B **59**, 4654 (1999).

[47] P. Weitz, E. Ahlswede, J. Weis, K. Klitzing, and K. Eberl, Appl. Surf. Sci. **157**, 349 (2000).

[48] P. Weitz, E. Ahlswede, J. Weis, K. Klitzing, and K. Eberl, Physica E **6**, 247 (2000).

[49] P. Weitz, Untersuchungen zum Verlauf der Hall-Spannung in einem zweidimensionalen Elektronensystem unter den Bedingung des Quanten-Hall-Effekts mittels eines Raster-Kraft-Mikroskops, PhD thesis, Max-Planck-Institut für Festkörperforschung / University of Hamburg (1999).

[50] S. Ihnatsenka and I. Zozoulenko, Phys. Rev. B **74**, 075320 (2006).

[51] S. Ihnatsenka and I. Zozoulenko, Phys. Rev. B **73**, 075331 (2006).

2. Scanning Force Microscope: A tool for local Hall potential probing

A Scanning Force Microscope (SFM) is used in this PhD work as a tool sensitive to the electro-statics [1]. To study the Hall potential distribution in the quantum Hall regime, our SFM has the specificity to be operated at 1.4 Kelvin and in high magnetic field up to 13 Tesla. The system is first configured as a SFM in contact mode to spatially located the Hall bar structure on the sample surface. Afterward, the microscope is switched to non contact mode. The tip away from the sample surface (around 50 nm) probes the electrostatic potential variations while scanning. As the two-dimensional electron system is buried few tens of nanometer below the surface, a certain calibration technique is required to obtain Hall potential profiles.

In this chapter, the principles and the relevant working parameters of scanning microscopy are reviewed. Different measurement techniques such as contact and non contact mode - including AM- and FM-detection, are compared in order to understand the calibration technique which is used to measured the Hall potential in this PhD thesis.

Contents

2.1. The principles of Scanning Probe Microscopy

2.1.1. Scanning Tunneling Microscopy (STM) versus Scanning Force Microscopy (SFM)

Our goal is to measure microscopic properties of 2DES embedded in an AlGaAs/GaAs heterostructure. For this purpose, we will use a local probe integrated inside a scanning probe microscope (SPM). The SPM technology starts in the 80's with the invention of the scanning tunneling microscope [i]. The STM works on the exponential dependence of the tunneling current with respect to the distance between a metallic tip and a conductive sample. The tunneling current allows either to perform surface topography or to process energy spectroscopy to determine the local electronic density of states. The STM principle limits its applications to conductive surfaces. This restricts the measurement to specific sample such as 2DES located at the InAs surface [4–6]. It is difficult to access the information of 2DES which are buried few tens of nanometer below non conductive GaAs and AlGaAs layers. The invention of the scanning force microscope as the atomic force microscope (AFM) by G. Binning, F. Quate and Ch. Gerber in 1986 [7] offers the possibility to perform local measurement on insulators as well. Instead of the tunneling current, the SFM uses a force-sensing cantilever which probes nano- or even picoNewton forces between the tip and the sample surface.

2.1.2. Different SFM working modes

Depending on the distance between the sample and the tip, different forces are felt and different modes of measurement may be operated by SFM: contact, tapping or non-contact mode (see table 2.1 and Fig. 2.1). These modes are analytically modeled via the description of a cantilever in term of a loading mass m_{eff} attached to a spring (Fig. 2.2). Such mass corresponds to the inertial properties of the cantilever. The spring constant characterizes its elasticity [ii].

Mode	Force	Cantilever state
Contact mode	Strong repulsive force	Static cantilever
Non Contact mode	Weak attractive force	Oscillating cantilever
Tapping mode	Strong repulsive force	Oscillating cantilever

Table 2.1.: Various probed forces allow different SPM modes.

---

[i] For the fabrication of the first STM with atomic resolution, Gerd Binning and Heinrich Rohrer shared the Nobel prize of physics in 1986 [2, 3] with the inventor of the scanning electron microscopy (SEM), Ernst Ruska.

[ii] The elasticity expressed by the Young modulus (E) shows the ability to return to the equilibrium position after displacement without any deformation.
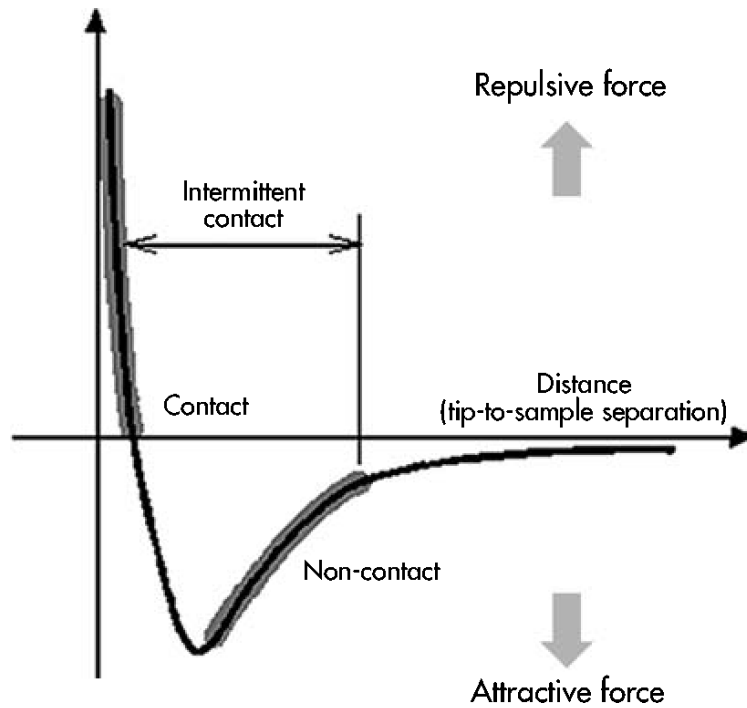
Figure 2.1.: Force versus tip-to-sample distance. Adapted from the Practical Guide of SPM edited by Park Scientific Instruments.
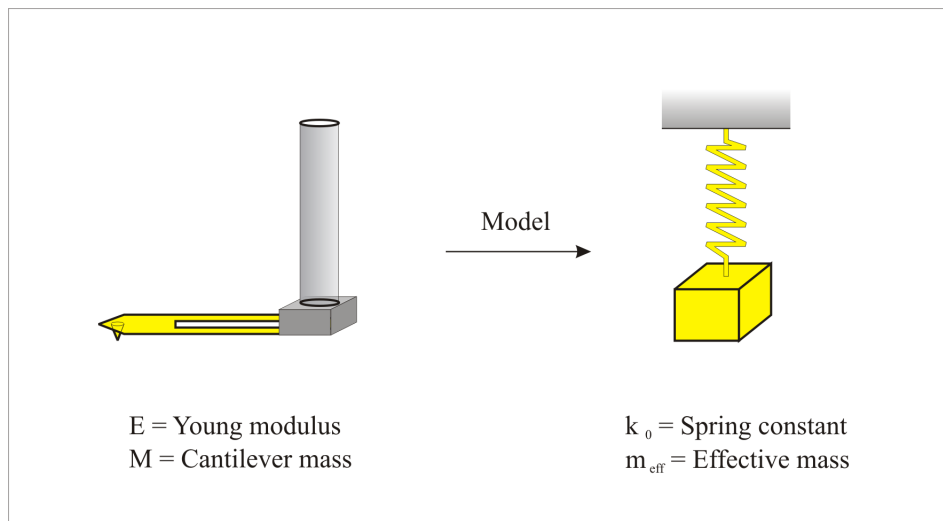

Figure 2.2.: A mass attached to a spring is a conventional model to describe the dynamics of a cantilever. The spring constant k and the loading mass m_{eff} are associated to the mass M and to the elasticity E of the cantilever, respectively.

2.1.2.1. Contact mode and tapping mode

In *contact mode*, the tip is in direct contact with the sample. An interatomic repulsive force of few nanoNewtons bends the cantilever's end with respect to the initial position $z(0)$. The new position $z(t) = z(0) - F/k$ is determined by the balance between the force of contact and the elastic reaction of the cantilever defined by the spring coefficient k. During the scanning, the bending induced by the force is kept constant via a feedback loop which regulates either the position of the sample or the position of cantilever's foot attached to a piezotube. This adjustment is recorded as the topographic signal. Due to the flexibility of the cantilever, the tip or the sample surface is not damaged [iii]. In our work, the contact mode is used to find the position of the Hall bars on the sample's surface.

Another technique is the *tapping mode* or amplitude modulation atomic force microscopy (AM-AFM) which is commercially applied to obtain surface topology. This technique is a dynamical AFM mode where the tip periodically touches the surface to limit damages. The cantilever is brought to oscillations very close to the surface with a high amplitude. A feedback loop drives the cantilever at a constant oscillation amplitude by continuously adjusting the distance between the sample and the cantilever. The distance variation offers a topographical map of the surface. In spite of its advantages, the tapping mode cannot be used in our system since the technique requires a cantilever with large spring constant to avoid the snap to the surface whereas our force detection need a soft cantilever.

2.1.2.2. Non contact mode

To probe only the contribution of the large range electrostatic force, the *non contact mode* has to be used. The cantilever dynamics in this mode may also be treated with the spring model. We start with free oscillations of a cantilever damped by the Helium gas environment. In consequence, there is no contribution from the sample in this particular case. The role of the environment on the oscillating motion is introduced to the dynamic equation via the addition of a friction force with viscous properties. In our system which contains helium exchange gas, the Reynolds number is much smaller than one and the friction force is taken as linear with respect to the speed: $\vec{F}_{\text{visc}} = -b \cdot \vec{v}$ (b as the phenomenological drag coefficient). The quality factor Q which depends on the damping mechanisms acting on the cantilever parameterizes this effect. The bending of the cantilever $z(t)$ follows

$$\ddot{z}(t) + 2\gamma \cdot \dot{z}(t) + w_0^2 \cdot [z(t) - z(0)] = 0 \tag{2.1}$$

[iii] To achieve best sensitivity, soft cantilevers characterized by a very small spring constant are usually used. They gives the highest deflection and therefore the maximum ratio cantilever deflection/force. For a contact force being in the order of nanoNewton, a spring constant of 0.1 N/m offers a detectable cantilever bending of few nanometers.

with $w_0^2 = k/m_{\text{eff}}$ the fundamental natural frequency and $\gamma = b/2m$ the damping coefficient. Such equation corresponds to a harmonic oscillator with damped oscillations due to the dissipation of its energy in the environment. Three different regimes are distinguishable depending of the value of w_0 compared to γ: periodic ($\gamma << w_0$), pseudo-periodic ($\gamma < w_0$) or aperiodic ($\gamma \geq w_0$). In the pseudo-periodic regime, the equation gives the damped oscillation $z(t) = z_0 \cdot \cos(w \cdot t + \phi_0) e^{-\gamma \cdot t}$ with $w = \sqrt{w_0^2 - \gamma^2} = w_0 \cdot \sqrt{1 - 1/4Q}$. The environment has then two effects: (1) shift the resonance frequency by a term which depends on the quality factor Q and (2) damp the oscillations on a time scale given by γ.

To compensate the dissipative effect, the cantilever is mechanically forced to oscillate at a constant amplitude via a time dependent oscillating force, $F(t) = F \cdot \cos(w_{exc} \cdot t)$. The dynamical equation becomes:

$$\ddot{z}(t) + 2\gamma \cdot \dot{z}(t) + w_0^2 \cdot [z(t) - z(0)] = F \cdot \cos(w_{exc} t) . \qquad (2.2)$$

The answer of the cantilever is $z(t) = A(w_{\text{exc}}) \cdot \cos(w_{\text{exc}} t + \phi)$ with a phase shift of ϕ and an amplitude given by

$$A(w_{\text{exc}}) = \frac{F}{k} \cdot \frac{Q}{\sqrt{Q^2 \cdot \left[1 - (w_{\text{exc}}/w_0)^2\right]^2 + (w_{\text{exc}}/w_0)^2}} . \qquad (2.3)$$

The amplitude is maximum at $w_{\text{exc}} = w_0 \cdot \sqrt{1 - 1/2Q^2} = w_{\text{res}}$ which is the resonance frequency of the system. The amplitude value at the resonance is then

$$A(w_{\text{res}}) = \frac{F}{k} \cdot \frac{Q}{\sqrt{1 - \left(\frac{w_{res}}{w_0}\right)^2}} . \qquad (2.4)$$

In vacuum or under helium exchange gas [iv], the quality factor is very high. As a consequence $w_{\text{res}}/w_0 \ll 1$ and the development of the amplitude becomes in the first order directly proportional to the force strength and to the quality factor: $A(w_{res}) \sim F \cdot Q/k$. In our system, the cantilever oscillations are in fact not excited by an oscillating force but stimulated at its foot by the motion of the piezoelectrical tube with an amplitude a. The cantilever's answer is netherless similar: $A(w_{res}) \sim a \cdot Q$.

The cantilever tip feels a gradient of electrostatic force if it oscillates few tens of nanometer above the surface. This gradient will shift the resonance frequency. The reason of this effect is simple. For an inhomogeneous force in height, Taylor series gives

$$F(z(t)) = F(z(0)) + \frac{\partial F}{\partial z(t)} \cdot [z(t) - z(0)] + \ldots$$

[iv] We remind that our cantilever is located in chamber with low pressure (10^{-3} mbar).

The first term is a static force which simply induces a correction to the equilibrium position whereas the second term resembles a change of the effective spring constant. This can be seen by

$$[z(t) - z(0)] \cdot k_0 = F(z(0)) + \frac{\partial F}{\partial z(t)} \cdot [z(t) - z(0)] \,,$$

$$[z(t) - z(0)] \cdot \left(k_0 - \frac{\partial F}{\partial z(t)} \right) = F(z(0)) \,,$$

$$[z(t) - z(0)] \cdot k_{\text{eff}} = F(z(0)) \,.$$

It follows that $k_{\text{eff}} = k_0 - \partial F / \partial z(t)$ and the resonance frequency is changed from $w_0^2 = k/m_{\text{eff}}$ to $w_{\text{eff}}^2 = k_{\text{eff}}/m_{\text{eff}}$. During the scanning, this change of the resonance frequency due to the force gradient $\partial F / \partial z(t)$ is

$$\Delta w = w_{\text{eff}} - w_0 = w_0 \cdot \left(\sqrt{1 - \frac{\partial F / \partial z(t)}{k_0}} - 1 \right) \simeq -\frac{w_0 \cdot \partial F / \partial z(t)}{2 \, k_0} \,. \qquad (2.5)$$

In the present PhD work, the frequency shift is recorded via a slope detection in the phase signal. This signal is used as an information concerning the gradient of the electrostatic force. Frequency Modulation-AFM technique will also be possible to directly measure the frequency shift. Such technique has the advantage to separate the dissipation effect from the frequency shift and to avoid the time delay found in AM-AFM [v].

---

[v] In the Amplitude Modulation-AFM, the answer to the change of the tip-sample interaction is not instantaneous and depends on the Q factor on the time scale $\tau \simeq 2Q/f_0$. In vacuum, this time scale can be very large. The FM-AFM solves this problem since it is by a factor $2Q$ faster ($\tau \simeq 1/f_0$).

2.2. Local probing of the Hall potential by SFM

2.2.1. General description of Scanning Force Microscope

Local probe working at low temperature and in high magnetic fields is needed to locally study the electronic properties of 2DES in the quantum Hall regime. Peter Weitz developed in our laboratory a homemade scanning force microscope incorporated inside a vacuum chamber where
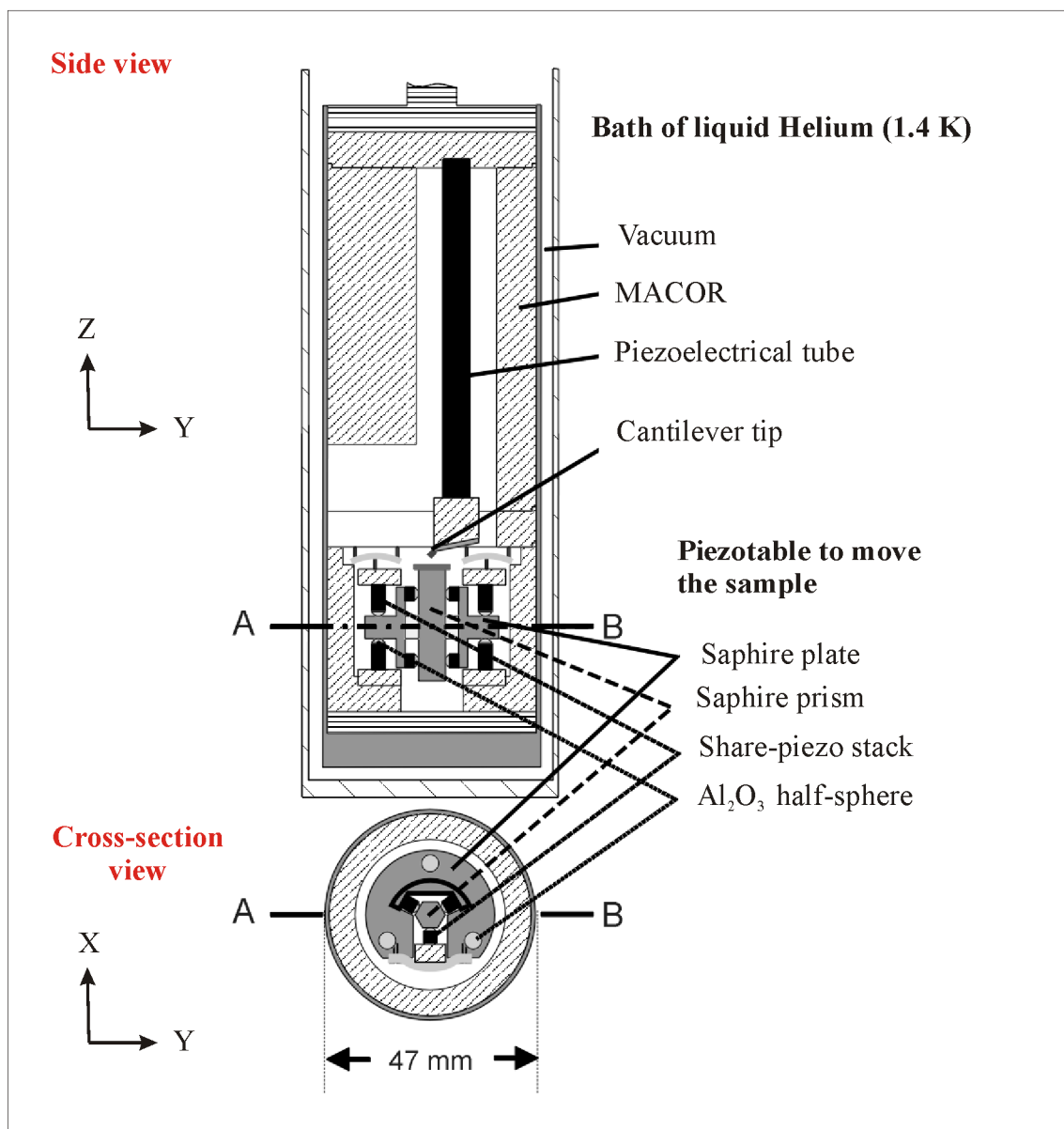

Figure 2.3.: Sketch of the cryogenic scanning force microscope built in the von Klitzing group. Adapted from P. Weitz PhD work [8].

exchange gas is added for better cooling. The system operates at 1.4 Kelvin and in magnetic field up to 13 Tesla [1]. There are only few systems which can operate under these extreme environments. The head of the microscope is shown in figure 2.3. It is integrated in a Macor frame [vi] which has a diameter of 47 mm space in order to fit inside the variable temperature insert of an Oxford He^4 cryostat. The local probe is a metalized tip located on a piezoresistive cantilever. This cantilever is attached to piezoelectric tubes which perform z correction and scan the tip over a 20×20 μm^2 area. At the end of the tube, a piezoelectrical plate allows to excite the cantilever to its resonance frequency. The sample is positioned below the tip via the integration of a piezoelectric table moving over several millimeters. For controlling the SFM and acquiring the data, an electronic from Omicron company is used. The resonance frequency shift of the piezoelectric cantilever is measured via the unbalanced voltage of a Wheatstone bridge and additional hardware serves to do the feedback loop (further information can be found in [8]).

2.2.2. Piezoresistive silicon cantilever as a force detector

Local probing via SFM is based on the resonance frequency shift of a cantilever by a force gradient. The force gradient is measured either via an extrinsic[vii] or an intrinsic system. The extrinsic detection is easy to realized in air or in liquid. Simple to adjust, the optical method with laser interferometry or beam-bounce is usually used in commercial AFM [9]. The challenge to process several tips at the same time, to scan large samples or to work in extreme environment conditions encourage to apply intrinsic detection which are based on the changes of the physical property of the cantilever - i.e. its piezoresitivity [i] or its piezoelectricity [ii]. For instance our scanning force microscope is working at low temperature and a detection based on a piezoresistive cantilever instead of the conventional laser beam detection [10–13] has been installed. This system has the advantage to cancel the difficulty to align a laser beam inside the cryostat.

[vi] Macor material has the advantage to be non magnetic, easily to be structured and it has a small thermal expension coefficient.

[vii] The detection device may be a STM which probes the tunneling current through the conductive backside of the cantilever, a metallic plate which measures the change of capacitance between the plate and the cantilever, a fiber optic which records the interference produced by the optical cavity formed by the distance between the cantilever and the end of the fiber, or a laser beam reflected to a photosensitive detector. Tunneling tip, optic fiber and plate capacitor have to be integrated close to the cantilever tip. This close spacing limits the oscillations amplitude and the scanning over a large area.

[i] Piezoresitivity is a physical property of certain materials changing their electrical resistance when a stress is applied to them. Piezoelectric quartz tuning fork is used for dynamics AFM since it is very stable over time and over temperature variations and it has very low dissipation. Its main problem is the large size. Piezoelectric sensors with higher piezoelectric coefficient than quartz (such as ZnO) was thought to overcome this size problem. Unfortunately, those materials show high internal dissipation and high frequency instability.

[ii] Piezoelectricity is the physical property of certain materials to build an electrical field when a stress is applied to them.

In addition, it avoids light source on our studied semiconductor samples which are extremely disturbed by light. Our piezoresistive cantilever is a silicon [viii] cantilever with a highly doped layer using as a conductive current path (hatched area in Fig. 2.4). The silicon cantilever is asymmetrically doped on one surface (Fig. 2.5(c)) to assume a net resistance change due to the piezoresistive effect during the cantilever bending. This change is measured via a Wheatstone bridge. A Wheatstone bridge is an electrical circuit made from four resistance which allows very sensitive measurement of resistance variation (the schematic is presented in Fig. 2.4). If the equal current which flows through the two branches of the circuit is detuned due to different resistances between the two branches, a potential appears at the bridge corners and informs on a resistance variation.
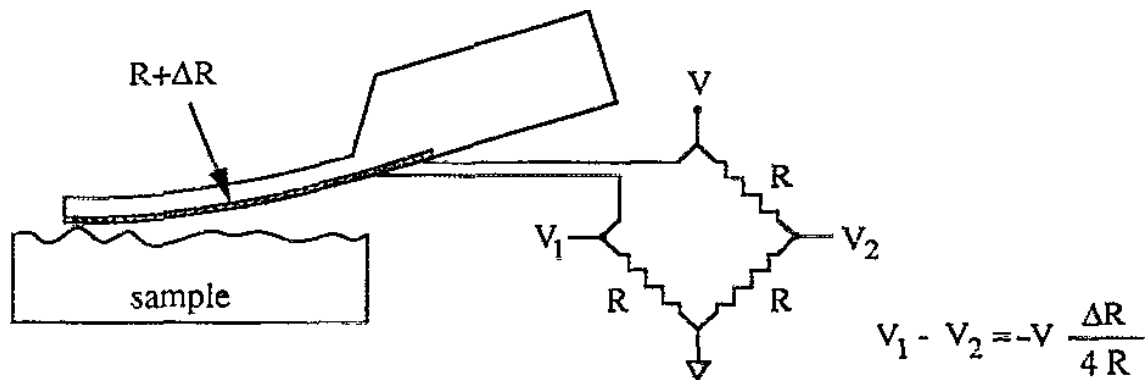
Figure 2.4.: Schematic of a SFM detection system based on a piezoresistive cantilever. The piezoresistive element is integrated to a Wheatstone bridge. Adapted from M. Tortonese [10].

[viii] The materials in which the cantilever are made varies with the application. For its physical properties (Young modulus, density, hardness) and for micromachinery reason, the cantilevers are often built from silicon nitride or single crystal silicon. Oxidation process produces very sharp tip with very high aspect ratio when the silicon dioxide SiO_2 is removed by HF solution. Diamond tip is also produced for scratching process and carbon nanotube tips for high resolution measurements.

2.2.3. The objective of tip metalization

The silicon piezoresistive cantilever has to be metalized since a magnetic field has a strong effect on the silicon but few effect on metalized tip. The tip can also be grounded and used as reference potential. Figure 2.5(a) represents the schematic of its package with the ceramic holder. The free standing cantilever and the static cantilever used as a reference resistance are integrated in a conductive circuit which forms the Wheatstone bridge. The spread of an insulating polyamide layer allows to evaporate gold/palladium without creating electrical short cut. Nevertheless the metalization of the tip brings other disturbances. For an electrostatic point of view, the metalized cantilever located above semiconductor surface can be treated as plate capacitor (Fig. 2.6). The metallic tip and the 2DES are the two plates of the capacitor. These

Figure 2.5.: **a)** Ceramic plate on which the electrical circuit containing the cantilevers is integrated. Insulating polyamide layer (blue) protects the electrical circuit from the evaporated AuPd thin layer used to ground the tip. **b)** Zoom in the freestanding cantilever tip. **c)** Cross section of silicon cantilever system after metalization.
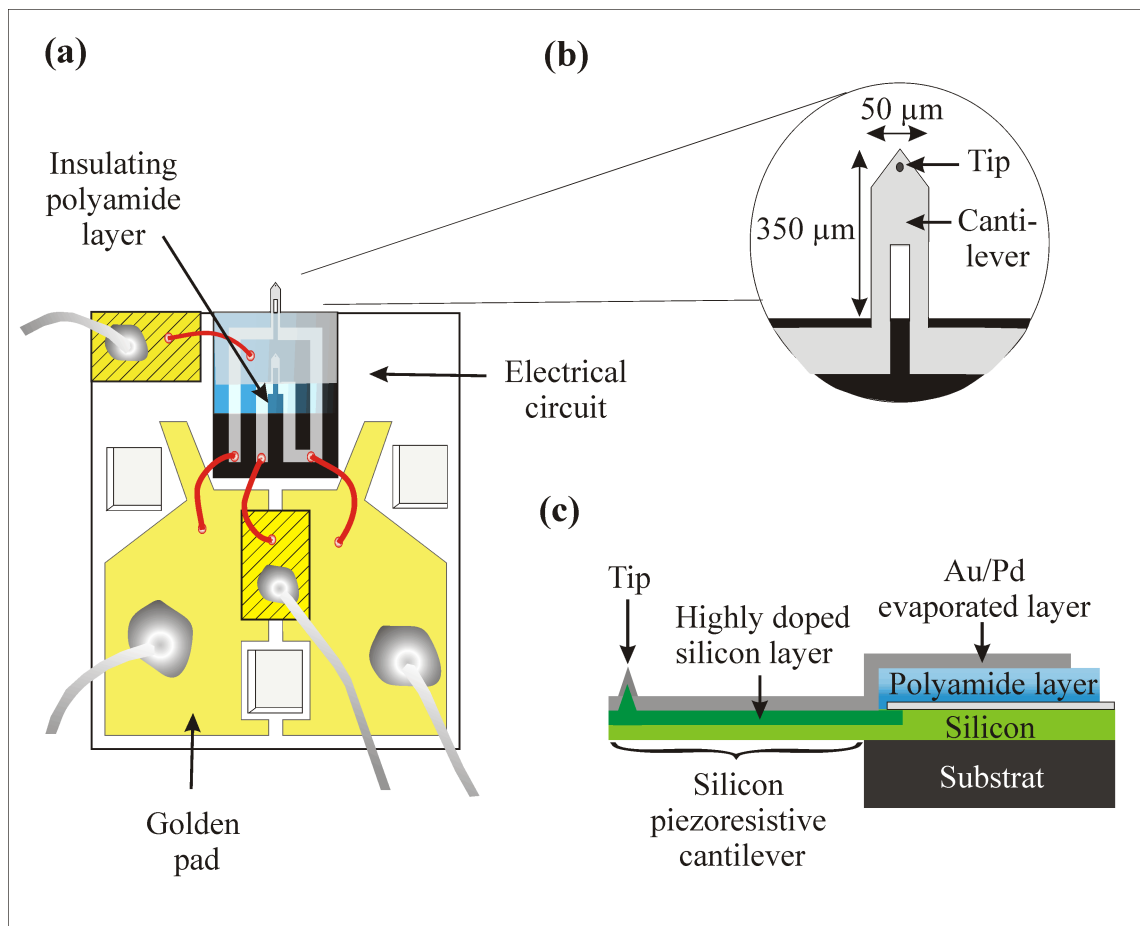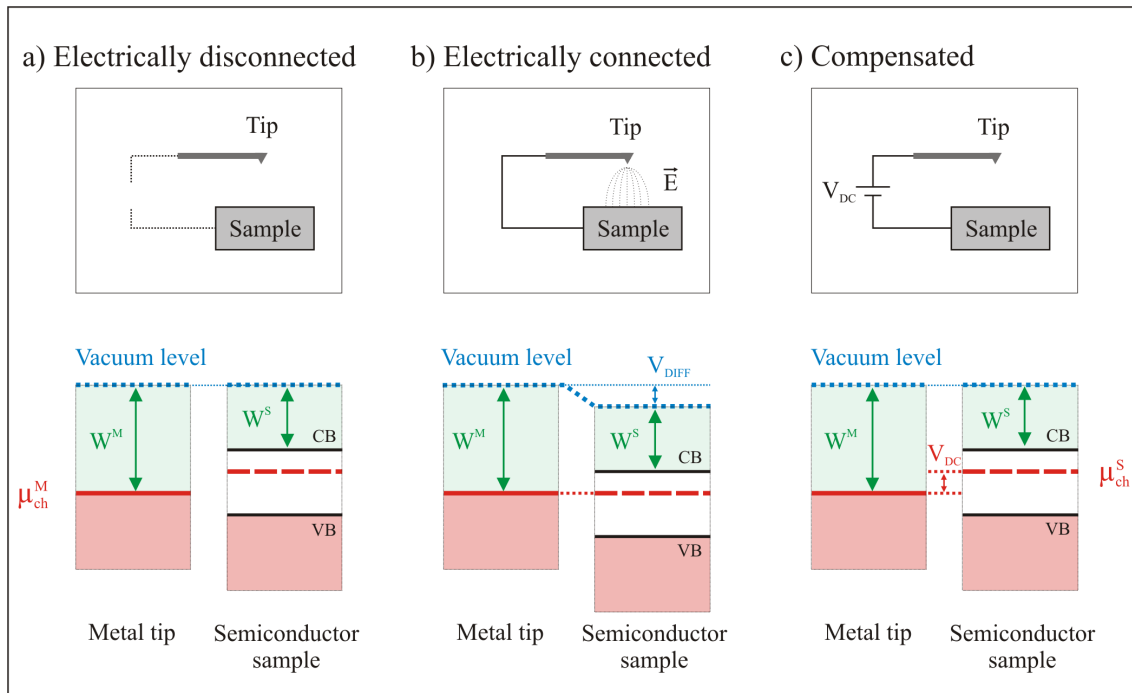
Figure 2.6.: **a)** Metallic tip and semiconductor sample with different work functions. **b)** If the tip and the sample are electrically connected, the difference of work function between the metallic tip and the semiconductor induced an electrical field. **c)** The electric field is compensated by a biased voltage.

plates being electrically connected (see Fig.2.6(b)), a charges transfer due to the difference of work functions between the tip and the sample induces a local electric field. Such electric field may partly deplete the 2DES. DC voltage is applied to compensate for it (Fig.2.6(c)).

2.2.4. Tip approaching with an AC voltage excitation

Tip and sample mounted on piezoelectric tube and table respectively are inserted inside the VTI of the cryostat. After reached to 1.4 K, a series of high voltage ramp is applied to the piezo-electric table [ix] in order to move the sample step by step near the tip. This approach stops if the static piezoelectric cantilever creates a voltage at the Wheatstone bridge which corresponds to a cantilever bending by a force of 10 nN. Before the approach, the voltage offset of the Wheatstone bridge is adjusted to zero by adding parallel resistances and capacitances to the circuit. To avoid tip crash, the Wheatstone bridge is electrically excited at few hundred millivolts with a very fast signal at 110 kHz (see fig 2.7(a)). The bending of the cantilever will modulate this

---

[ix] The poor efficiency of the piezoelectrical properties at low temperature forces to use high voltage.
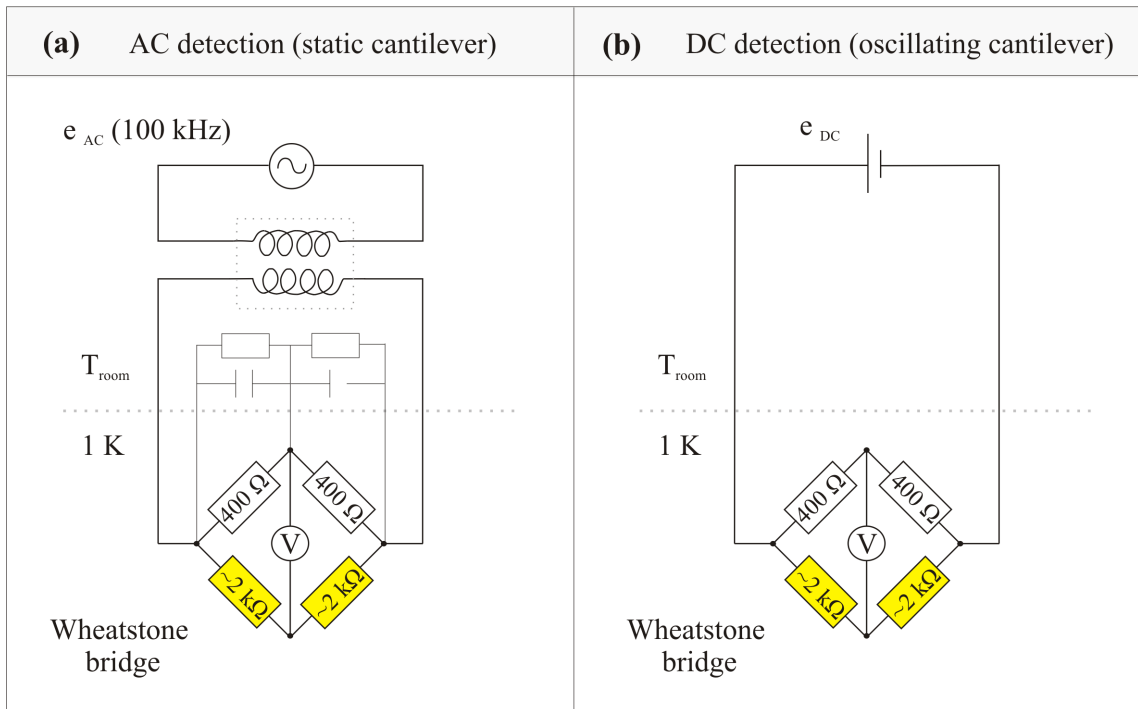
Figure 2.7.: Detection system with a Wheatstone bridge. **a)** AC configuration for tip approaching. The resistance around $2\,\mathrm{k\Omega}$ correspond to a piezoresistive cantilever. **b)** DC configuration for potential measurement.

signal by few microvolts [x]. When the tip touches the sample surface, topography is performed in contact mode and the tip is positioned above the Hall bar. The position adjustment is rather large since the cooling process and setup installation usually misaligns the tip and the mesa by few tens of micrometers.

---

[x] To be detected the signal is first amplified with a low noise preamplifier and recorded via lock-in technique.

2.2.5. Compensation of the work function difference via an applied DC voltage

The next step is to compensate the difference of work function between the metallic tip and the semiconductor sample by applying a DC voltage V_{DC} between tip metallization and 2DES. It avoids that the difference of work functions - named contact potential difference, depletes the 2DES. To find the correct DC voltage, Kelvin probe technique is used (see appendix B). The setup is switched to non contact mode with a DC voltage applied to the Wheatstone bridge (see Fig.2.7(b)). The amplitude versus excitation frequency is measured for different DC voltage
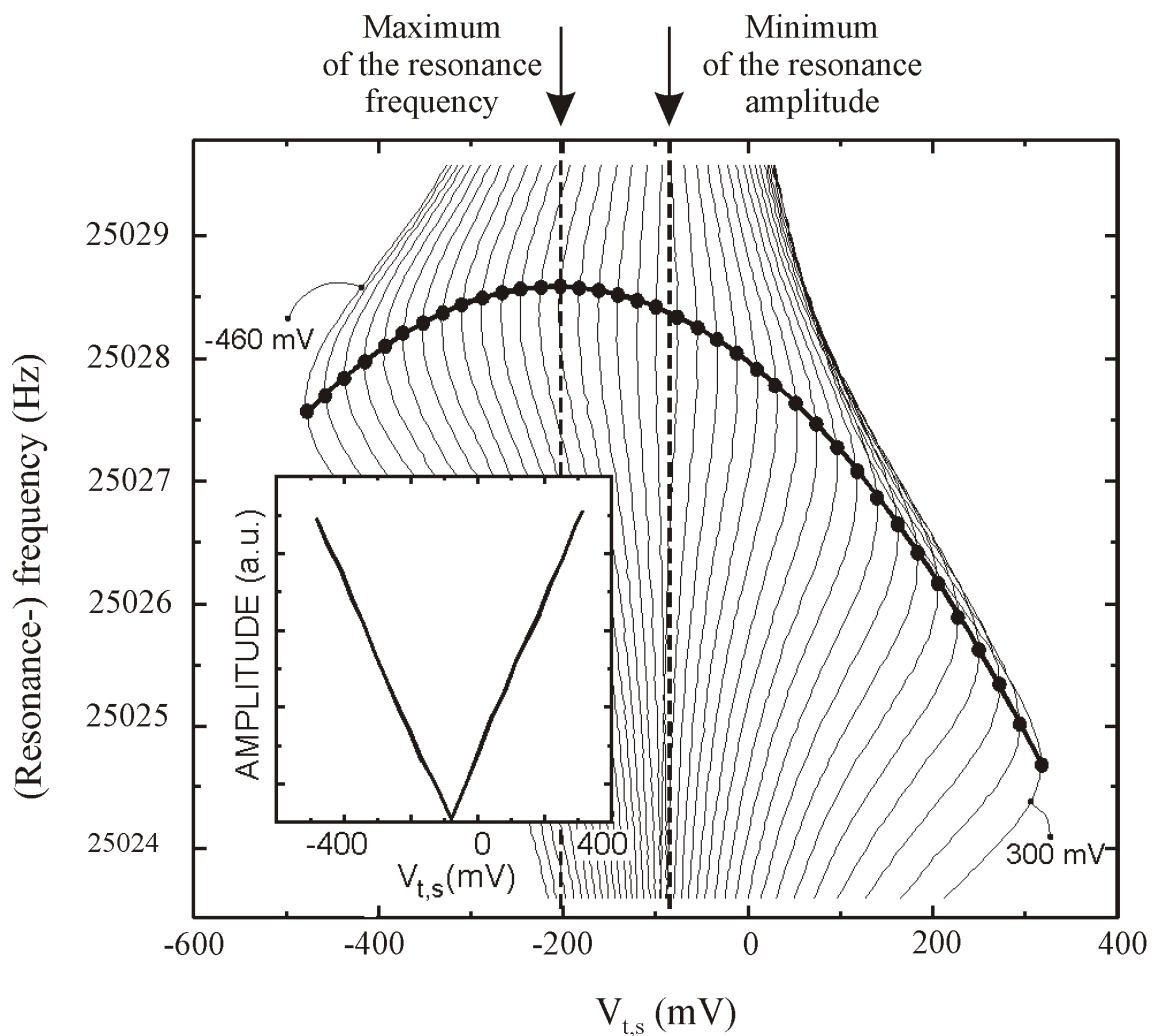
Figure 2.8.: Kelvin probe measurement to access to the voltage point contact. The frequency spectrum is measured for different biased voltage between the tip and the 2DES. Adapted from E. Ahlswede [14].

applied between the grounded tip and the 2DES (see different vertical curves in Fig. 2.8). On one hand, the resonance frequencies for different V_{DC} show a quadratic dependency with respect to the bias voltage. On the other hand, the maximum of the amplitude obtained at the resonance frequency changes linearly with the voltage and has a minimum at the voltage which corresponds to the contact potential difference (see the inset of the figure 2.8). Typically found around -100 mV, this voltage is applied to the 2DES during the Hall potential measurement in order to avoid electron depletion. Different to the minimum of frequency shift located around -200 mV, such voltage value is a good working point since a small variation of potential corresponds to a measureable variation of frequency shift.

2.2.6. The calibration technique to measure Hall potential profiles

Our measurements need to be only sensitive to the long range electrostatic force. For this purpose, the SFM tip is scanned in non contact mode around 50 nm above the surface. Nevertheless, the potential of 2DES being located few tens of nanometer below the heterostruture surface cannot be measured directly. Surface charges might interfere. A calibration technique is used to remove this disturbing contribution. The Wheatstone bridge in this case is in DC configuration (Fig 2.7(b)). To understand the principle of the calibration technique, we first describe a model for the electrostatic force. The system tip/vacuum gap/2DES is seen in first order like a capacitor in which some charges are added in between. Precisely, three different contributions to the electrostatic energy are expected:

- A capacitor term $C_{t,s}(z)$ coming from the voltage difference between the tip and the sample.

- Trapped charges at the surface of the sample.

- Charges in the donor layer.

These contributions create an electrical field at the tip surface and induce charges on the tip via image effect. The electrostatic energy is written as:

$$W(z) \propto \frac{1}{2}C_{t,s}(z) \cdot \triangle\phi_{t,s}^2 + Q_t(z) \cdot \triangle\phi_{t,s} + W_{\text{ion}}(z) \qquad (2.6)$$

with

$$\triangle\phi_{t,s} = \phi_{\text{2DES}} - \phi_{\text{tip}} = V_{t,s} + \mu_{2DES}^{\text{ch}}/e - \mu_{\text{tip}}^{\text{ch}}/e = V_{t,s} + \Delta\mu_{t,s}^{\text{ch}}/e$$

and

$$V_{t,s} = V_{\text{DC}} + V_{\text{AC}} \cdot \sin(w_{\text{m}} \cdot t)\,.$$

ϕ_{tip} and ϕ_{2DES} are tip and 2DES electrostatic potential respectively. $Q_t(z)$ is the total charge image on the tip due to the donor layer and surface charges. $W_{\text{ion}}(z)$ is the energy due to the

interaction of the donors and the surface charges. Both of them contain a $x-y$ dependency since they correspond to local event in the space area of the scanning measurement. The electrostatic
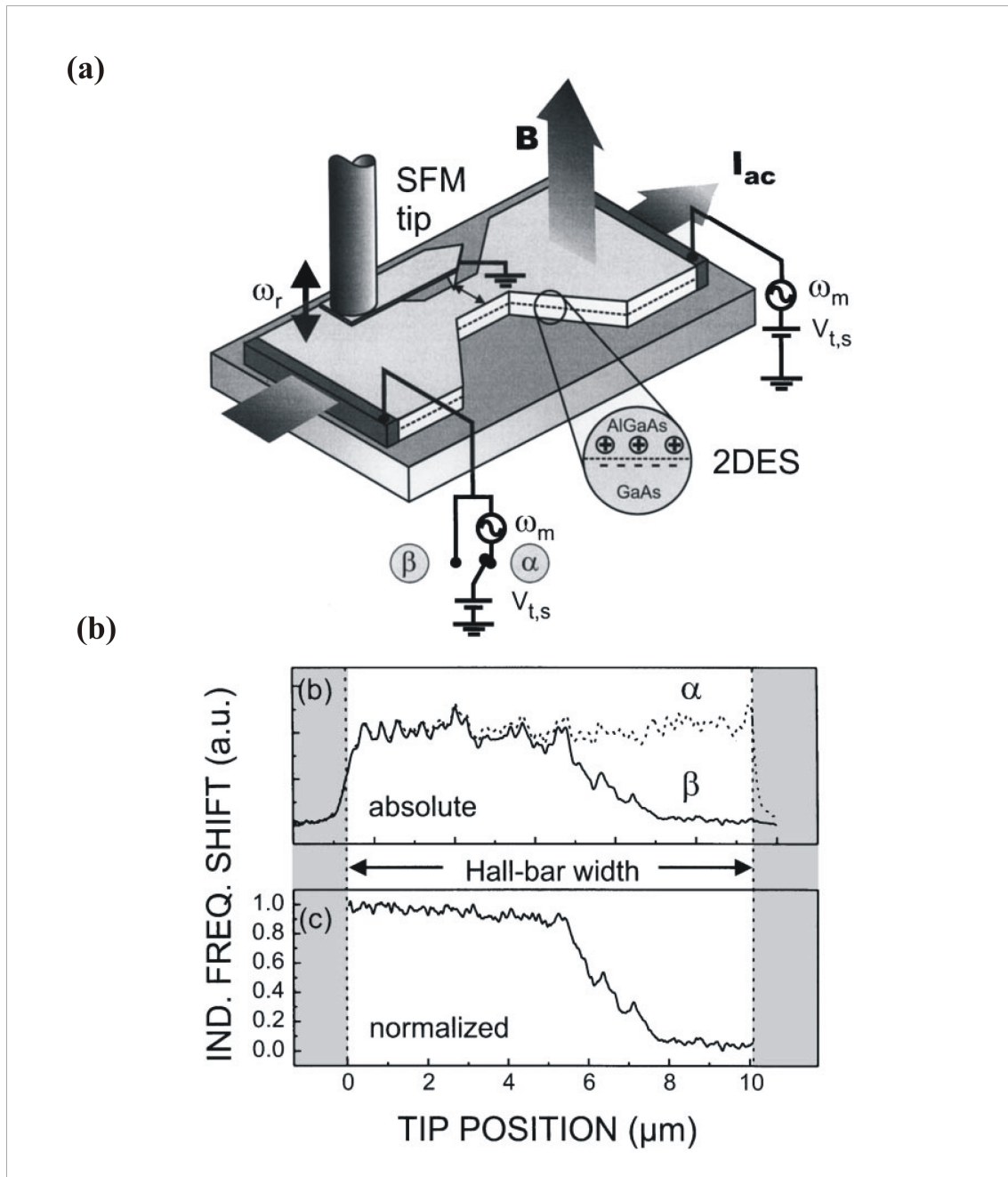

Figure 2.9.: **a)** SFM above a 2DES Hall bar. The electrical connections correspond to the calibration technique configuration (see text). **b)** Example of potential measurements: absolute data with the switch on α or β, and normalized data corresponding to the ratio β/α. Adapted from E. Ahlswede [14].

force

$$F(z) = \frac{\partial W}{\partial z} \propto \partial_z \, C_{t,s}(z) \cdot [V_{t,s} + \triangle\mu_{t,s}^{ch}/e]^2 + \partial_z \, Q_t(z) \cdot [V_{t,s} + \triangle\mu_{t,s}^{ch}/e] + \partial_z \, W_{ion}(z)$$

induces a shift of the frequency (see equation 2.5) measured by lock-in modulation detection at $w_m = 2\pi \cdot 3.4$ Hz [xi]:

$$\triangle\omega \propto \partial_z \, F_w(z) \propto \left\{ \partial_z^2 \, C_{t,s}(z) \cdot [V_{DC} + \triangle\mu_{t,s}^{ch}/e] + \partial_z \, Q_t^2(z) \right\} \cdot V_{AC}(x,y) \,. \qquad (2.7)$$

In a first time, the scan is processed with only one contact at $V_{t,s} = V_{DC} + V_{AC} \cdot \sin(w_m \cdot t)$ via the switch in β position (Fig. 2.9(a)). Current is flowing through the 2DES and Hall potential is built. The frequency shift is

$$\triangle^\beta\omega \propto \left\{ \partial_z^2 \, C_{t,s}(z) \cdot [V_{DC} + \triangle\mu_{t,s}^{ch}/e] + \partial_z \, Q_t^2(z) \right\} \cdot V_{AC}(x,y) \,. \qquad (2.8)$$

To remove the term in the bracket of the equation 2.8, the potential is probed at the same scan line but with two contacts at $V_{t,s} = V_{DC} + V_{AC} \cdot \sin(w_m \cdot t)$. In this configuration, the switch is at the α position. There is no current, the system is in equilibrium. The shift of frequency corresponds to a constant distribution of modulation amplitude V_{AC} weighted by same spatial unwanted contributions:

$$\triangle^\alpha\omega \propto \left\{ \partial_z^2 \, C_{t,s}(z) \cdot [V_{DC} + \triangle\mu_{t,s}^{ch}/e] + \partial_z \, Q_t^2(z) \right\} \cdot V_{AC} \,. \qquad (2.9)$$

By doing the ratio $\mathrm{Trace}(\beta)/\mathrm{Trace}(\alpha) = V_{AC}(x,y)/V_{AC}$ of these two signals, it becomes possible to access to the normalized Hall potential and to remove the unwanted contributions.

2.2.7. Electrostatic potential from the electrochemical potential

The SFM measurements record the change of electrostatic potential with respect to an equilibrium situation. The model presented in this PhD dissertation is based on the electrochemical potential μ_{elch}. For the qualitative point of view, these two quantities have the same spatial dependency. Figure 2.10 illustrates this idea. The first draw displays the spatial dependency of the energy spectrum along the Hall bar width for a bulk filling factor at $\nu = 2.5$ (Fig. 2.10(a)). The black lines correspond to the Landau levels and they bent up at the mesa's boundaries due to the potential of confinement. The Landau levels are flat at the metallic-like compressible strips whereas they display a variation at the position of the incompressible strips. In equilibrium, all the compressible strips have the same electrochemical potential. When a voltage is applied to the contacts at the extremities of the Hall bar, the electrochemical potential of the compressible strips situated at its edges follows either the low (blue) μ_{elch} of the grounded contact or the

---

[xi] Due to the lock-in detection, only the term on w_m in the force should be kept. The excitation V_{AC} applied to the 2DES is around 15 mV. Lower excitation values give the same potential profiles with larger noise.
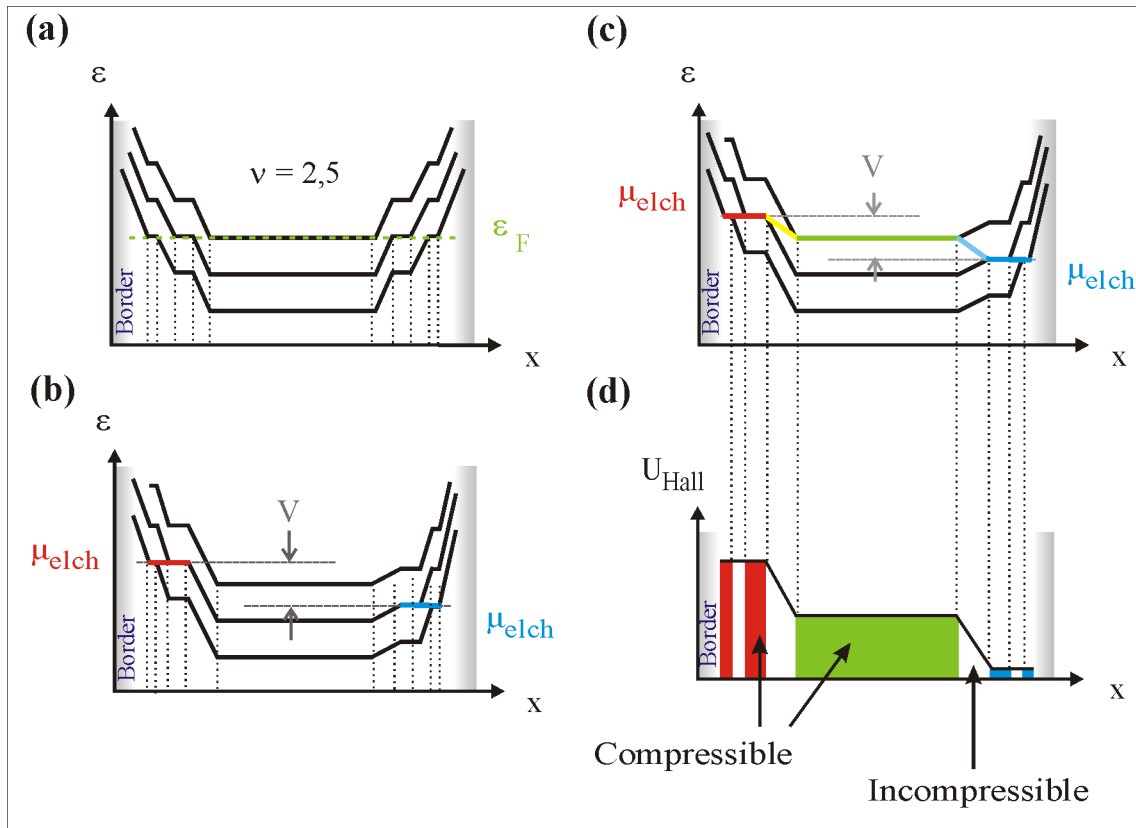
Figure 2.10.: **a)** Landau level energy at $\nu = 2.5$ and for equilibrium situation. **b)** Out of equilibrium case when a voltage V is applied at the mesa's boundaries. One mesa's edge follows the lower energy (blue) whereas the other edge has higher energy (red). **c)** The Landau level inside the bulk of the Hall bar is balanced to an averaged energy (green). Potential drops (yellow and light blue) occur at the mesa edges. **d)** Hall potential energy.

high (red) μ_{elch} of the voltage excited contact (Fig. 2.10(b)). The metallic-like bulk also adjusts its electrochemical potential to an intermediate constant value (green in Fig. 2.10(c)). Due to their metallic behavior, the variation of potential is screened at these compressible strips and the electrostatic potential is constant similar to the electrochemical potential (Fig. 2.10(d)). In consequence, the drop of potential presented in the figure 2.10(c) only happens at the position where the electrochemical potential changes (yellow and light blue in Fig. 2.10(c)).

Bibliography

[1] P. Weitz, E. Ahlswede, J. Weis, K. Klitzing, and K. Eberl, Appl. Surf. Sci. **157**, 349 (2000).

[2] G. Binnig, H. Rohrer, C. Gerber, and E. Weibel, Phys. Rev. Lett. **49**, 57 (1982).

[3] G. Binnig and H. Rohrer, Rev. Mod. Phys. **56**, 615 (1987).

[4] M. Morgenstern, J. Klijn, C. Meyer, M. Getzlaff, R. Adelung, R. A. Römer, K. Rossnagel, L. Kipp, M. Skibowski, and R. Wiesendanger, Phys. Rev. Lett. **89**, 136806 (2002).

[5] M. Morgenstern, J. Klijn, C. Meyer, and R. Wiesendanger, Phys. Rev. Lett. **90**, 056804 (2003).

[6] M. Morgenstern, D. Haude, V. Gudmundsson, C. Wittneven, R. Dombrowski, and R. Wiesendanger, Phys. Rev. B **62**, 7257 (2000).

[7] G. Binnig, C. Quate, and C. Gerber, Phys. Rev. Lett. **56**, 930 (1986).

[8] P. Weitz, Untersuchungen zum Verlauf der Hall-Spannung in einem zweidimensionalen Elektronensystem unter den Bedingung des Quanten-Hall-Effekts mittels eines Raster-Kraft-Mikroskops, PhD thesis, Max-Planck-Institut für Festkörperforschung / University of Hamburg (1999).

[9] B. Bhushan, *Handbook of Nanotechnology* (Springer, Berlin, 2004).

[10] M. Tortonese, R. Barrett, and C. Quate, Ann. Phys. (Leipzig) **62**, 834 (1993).

[11] M. Tortonese, H. Yamada, R. Barrett, and C. Quate, IEEE Proceedings of transductors **91 CH2817-5**, 448 (1991).

[12] M. Tortonese and M. Kirk, Proceedings of SPIE **3009**, 53 (1997).

[13] M. Tortonese, *Force sensors for scanning probe microscopy* (UMI dissertation services, Standford University, 1993).

[14] E. Ahlswede, Potential- und Stromverteilung beim Quantum-Hall-Effekt bestimmt mittels Rasterkraftmikroskopie, PhD thesis, Max-Planck-Institut für Festkörperforschung / University of Stuttgart (2002).

3. Adiabatic transport features in the Quantum Hall regime

The mean free path l_{mfp} of charge carriers is used to characterize a conductor. Depending on its value with respect to the spatial length L of the conductor, one distinguishes between diffusive ($l_{\mathrm{mfp}} \ll L$) and ballistic ($l_{\mathrm{mfp}} \gg L$) regime. For a two-dimensional electron system (2DES) under high magnetic field, a third category has been introduced - named as adiabatic transport regime. Typical adiabatic transport features are the disappearance of peaks in the Shubnikov-de Haas oscillations, the extension of quantum Hall plateaus to lower magnetic fields and the existence of non-local resistances. The main idea of adiabatic transport is reviewed in this chapter and its experimental signatures are described. In the literature, the adiabatic transport regime is usually described as a non-equilibration of the chemical potentials between adjacent edge states running in parallel along the mesa edge. In the further course of my PhD thesis, this description has to be adapted due to my and previous scanning probe results. The more recent microscopic picture in terms on compressible and incompressible edge strips will be applied. Including the contribution from the electrostatic potential, this picture uses the electrochemical potential instead of the chemical potential. To emphasize, this chapter uses the term "chemical potential" since it is the language presented in Büttiker work. In retrospect – due to our scanning probe results – it requires another description based on the electrochemical potential which is later presented in Chapter 6.

Contents

3.1. Review of the adiabatic transport within the edge state picture

3.1.1. Adiabatic transport as a maintained local non equilibrium between edge states

Under magnetic field, the energy spectrum of 2DES is discretized in Landau levels which are bended up at the mesa's edges by the potential confinement. So-called edge states are formed at these mesa's edges where the Fermi level and the different Landau levels are crossing. Each of the edge states is an one-dimensional extended state which connects the contact terminals of the Hall bar. This number of edge states close to each edge is equal to the bulk filling factor, $\nu = n_{el} \cdot \phi_0 / B$. The microscopic picture of the quantum Hall effect (QHE) introduced by Marcus Büttiker is described in terms of such states (see [1] and chapter 1). In this picture, the source (drain) contact acts as a reservoir of charges which fills (empties) the edge states with respect to chemical potential of the contact. Biasing the sample with a net current I_{net}, the contacts adjust the value of their chemical potentials in order to fulfill the fixed current condition (later on, in a self-consistent picture, the description in term of electrochemical potential is preferred since it includes the contribution of the electrostatic potential).

In the edge states picture of the usual QHE, each edge state i is transmitted through the Hall bar and through the contacts with a probability of one ($T_i = 1$). It follows that states located at the same mesa edge have the same chemical potential over the complete length of the Hall bar. Figure 3.1(a) illustrates this case at filling factor $\nu = 2$ for a two-terminal device (the four states are represented by colored lines). For the magnetic field sign depicted in this figure, the states in the left border of the mesa have a low (blue) chemical potential μ_{ch} defined by the drain contact 2. The states in the right side have a high (red) chemical potential μ_{ch} defined by the source contact 1. The chemical potential of states located at the same mesa edge is equal between each other since states are equilibrated. The chemical potential difference $\Delta\mu_i^{\text{ch}}$ of the ith Landau level from the left edge to the right one is therefore independent of i: $\Delta\mu_i^{\text{ch}} = \Delta\mu^{\text{ch}}$. Due to the high chemical potential in the right edge, more electrons are propagating from contact 1 to contact 2 than vice versa on the left edge. The net current I_i carried by each edge state i is $I_i = e^2/h \cdot \Delta\mu_i^{\text{ch}}$. The biased current I_{net} is equally distributed between all the edge states since $\Delta\mu_i^{\text{ch}} = \Delta\mu^{\text{ch}}$. It follows:

$$I_{\text{net}} = \sum_{i=1}^{\nu} I_i = \sum_{i=1}^{\nu} \left(\frac{e}{h} \cdot \Delta\mu_i^{\text{ch}} \right) = \nu \cdot \frac{e}{h} \cdot \Delta\mu^{\text{ch}}.$$

The total conductance $G = I_{net}/U$ is quantized and $G = I_{net} \cdot e/\Delta\mu^{\text{ch}} = \nu \cdot e^2/h$.

Inhomogeneity inside the sample (intrinsic phenomena) or external gate electrodes (extrinsic effect) locally change the electron density. Under such a condition, channel might be reflected.

Its transmission probability becomes different from one ($T_i \neq 1$). For instance, the depletion induced by a gate electrode in figures 3.1(b) and (c) fully reflects the innermost channel, i.e. $T_2 = 0$. As a consequence, the outermost edge state on the right edge carries all the current by an increasing of its chemical potential as depicted in figure 3.1(c) via a change of color from red to lila. This new distribution of the chemical potential shows a strong non equilibrium locating at the right border of the mesa. In high mobility 2DES, such a non equilibrium may be maintained over several tens of micrometer since elastic and inelastic phonon-scattering rates are weak [2]. The maintaining of local non equilibrium between adjacent edge states as drawn in figure 3.1(**b**) is named *adiabatic transport regime*.

For samples with low electron mobility, the local difference of chemical potential between adjacent edge states are equilibrated by a large number of scattering events. Equal chemical potential is rapidly recovered. This situation is depicted in figure 3.1(**c**) in which the higher chemical potential represented by a lila color transits to a lower chemical potential (red color).
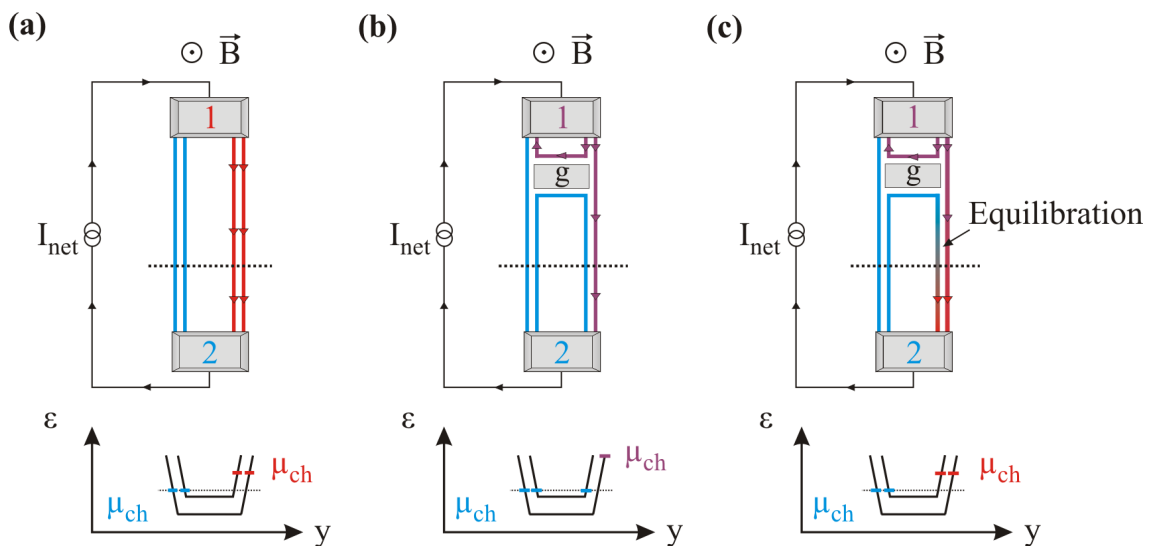
Figure 3.1.: **a)** Edge states picture of the QHE at $\nu = 2$ in a 2DES mesa under a fixed current. On the same border of the mesa the two edge states have identical chemical potential: low (blue) μ_{ch} on the left border and high (red) μ_{ch} on the right border. **b)** The inner edge state being reflected by a gate electrode named g, the outer edge state carries all the current via a higher μ_{ch} (lila) on the right side. The local non equilibrium is maintained along the complete sample length and the transport regime is adiabatic. **c)** Scattering events disturb the local non equilibrium in lower mobility 2DES.

3.1.2. Current carrying contacts showing internal reflection

Besides electron density inhomogeneities, the contacts to the 2DES might not work ideally and might cause reflections of edge states. This was pointed out by Marcus Büttiker [3]:

"Contacts that are made by alloying provide another possibility of contacts with internal reflection. It is possible that the metallic diffusion occurs not deep enough to reach the edge of the two-dimensional electron gas. Entrance and exit of the carriers occurs effectively then through a tunneling barrier. Another possibility is that the two-dimensional electron gas is reached but not near the edge of the sample. In such a situation, the contact again is reached only by tunneling or Mott hopping."

M. Büttiker, Semimetal and Semiconductor 35, p. 244 (1992)

Current injection via non-ideal contacts is expected in all experiment. One question arises: does this affect the measured magneto-resistance values ? Figure 3.2 schematically illustrates such an arrangement which was qualitatively described by M. Büttiker [4] and later quantitatively by S. Komiyama *et al.* [5]. The left (L) and right (R) current carrying contacts inject a fixed net current I_{net} in the mesa. This induces a difference of chemical potentials μ_{L} and μ_{R} between these two contacts. Contacts are metallic and own a continuum of states which have a probability to fill the ν edge channels of the 2DES (multiples lila and light blue arrows). Due to internal reflection at the contact area, the edge states might be differently occupied. For instance in figure 3.2, the inner state of the top edge is not filled by the left contact. To fulfill the current conservation, μ_{L} and μ_{R} are respectively higher and lower than expected (lila and light blue instead of red and dark blue). Such a non equilibrium of chemical potential is transmitted to the edge and smeared out either by equilibration processes along the mesa or by the presence of ideal contacts. The later case is illustrated in figure 3.2. Ideal contacts equilibrate the chemical potential distribution and give an averaging chemical potential μ_{A} or μ_{B}, respectively. The net current becomes equally distributed in between the ν channels since each channel has their states occupied until μ_{A} for the top edge or μ_{B} for the bottom edge. Even if the current carrying contacts performed selective injection, ideal probing contacts along the mesa edges will assume the usual Hall resistance value:

$$R_{\text{H}} = \frac{U_{\text{H}}}{I_{\text{net}}} = \frac{\mu_{\text{A}} - \mu_{\text{B}}}{e \cdot I_{\text{net}}} = \frac{h}{e^2} \cdot \nu^{-1}.$$

In conclusion, the non equilibrium population of the edge states due to the backscattering at the contact interface is not relevant for the quantum Hall effect if scattering between the edge states due to probing contacts or impurities restore equal chemical potential.
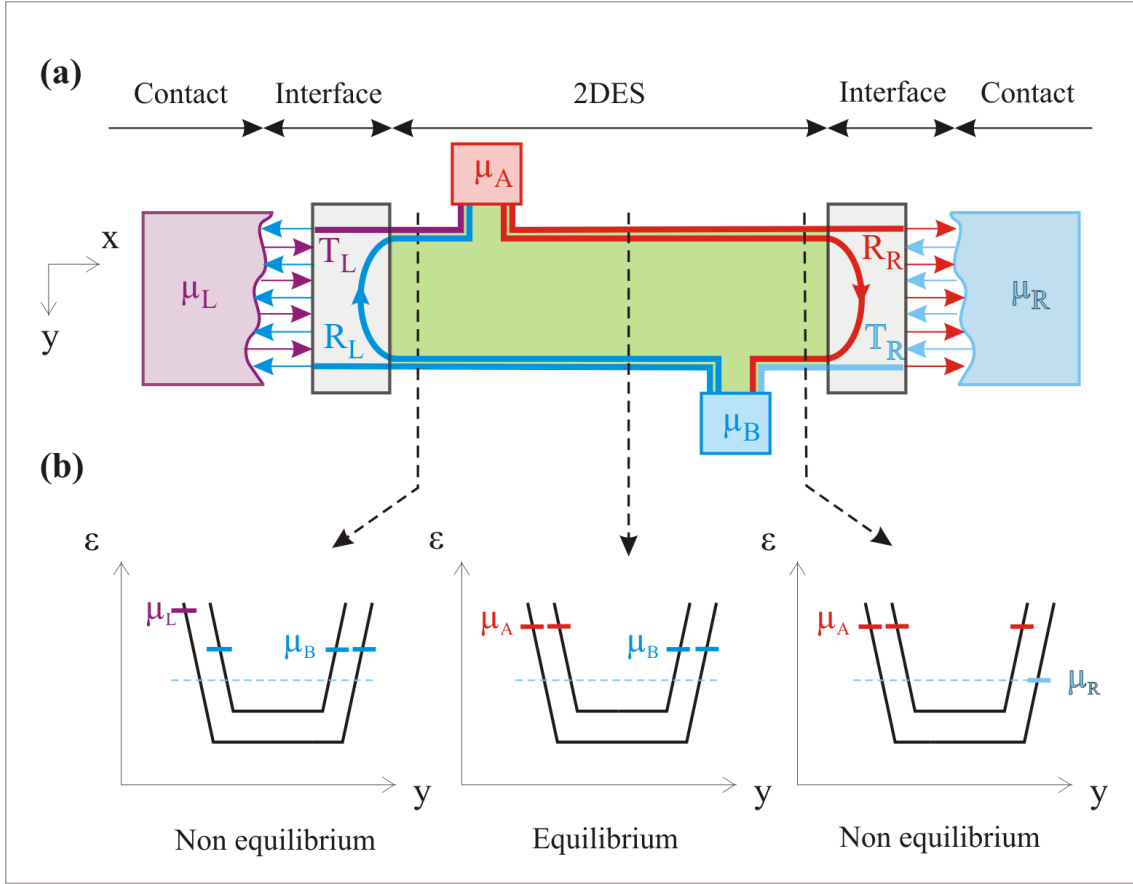
Figure 3.2.: **a)** Edge states distribution at $\nu = 2$ in a Hall bar having ideal voltage probing contacts. The current injection is done via contacts with internal reflection. **b)** Bended Landau levels with the chemical potential distribution at different spatial positions. The edge states at one edge are in non equilibrium or in equilibrium.

3.1.3. Non equilibrium situation probed by non ideal contact

Does the adiabatic transport shows no effect on the measured Hall resistance as it seems from the previous discussion ? If the injected edge states are in equilibrium, an ideal or non ideal voltage probing contact does not change the situation (see figure 3.3 a,b). On the other hand with an injecting edge states in non-equilibrium: an ideal contact equilibrates (c), whereas a non-ideal contact does not (d). Let assume for the latter case, that the injected edge states carry different fraction f_i of the bias current I_{net} - i.e. $f_i \neq \nu^{-1}$. The Hall resistance given by [6]

$$R_{\text{Hall}} = \frac{\Delta \mu_{ch}/e}{I_{net}} = \frac{h}{e^2} \cdot \frac{\sum_i^{\nu} T_i \cdot f_i}{\sum_i^{\nu} T_i}. \tag{3.1}$$

shows anomalous values due to an adiabatic situation. On the contrary, in equilibrium each state carries the same fraction of current $f_i = \nu^{-1}$ and the Hall resistance $R_{\text{Hall}} = \frac{h}{e^2} \cdot \nu^{-1}$ shows the

quantization at the proper integer filling factor whenever the contact has some internal reflection or not, i.e. whenever $\sum_i^\nu T_i \neq \nu$ or $\sum_i^\nu T_i = \nu$.

3.1.4. Summary

In the edge state picture, the adiabatic transport is the maintaining of a chemical potential difference between edge states locating at the same edge of the Hall bar. Such non equilibrium corresponds to an unbalanced distribution of the net current between edge channels. The magneto-resistances are not affected by this non equilibrium until the Hall bar implements sufficient scattering between the edge states on the way of source and drain, or until ideal contacts at the edges guarantee an equilibration of the chemical potential.
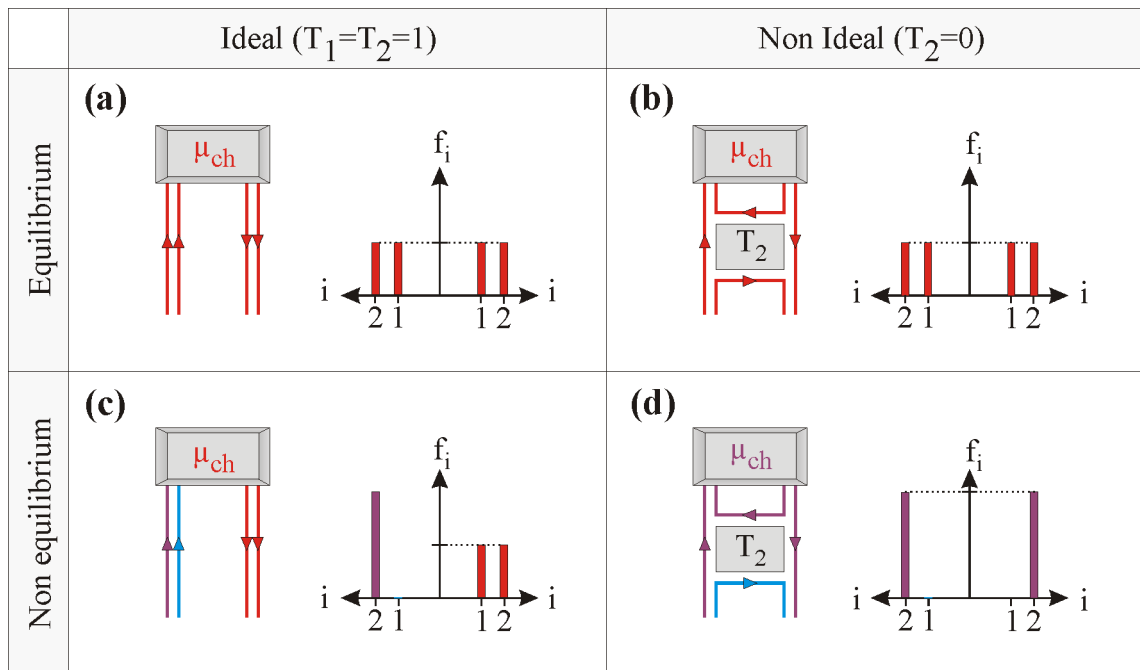
Figure 3.3.: Effect of a voltage probing contact on injected edge states. **a)** Edge states are injected in equilibrium, i.e. all the edge states carry the same fraction f_i of current. This is not changed by an ideal **(a)** or non-ideal contact **(b)**. If edge states are injected in non-equilibrium, either these states are equilibrated inside the contact and the averaged chemical potential is restored (red μ_{ch} in **(c)**), or the perfect reflection of the inner state $i = 1$ with low μ_{ch} induces a chemical potential change (lila μ_{ch} in **(d)**).

3.2. Previous experiments showing adiabatic transport features

In the 90's, several research groups performed measurements in order to study the adiabatic transport. In the following, some of those experiments are presented to illustrate three different features which are interpreted as the effect of an adiabatic transport: the extension of quantum Hall plateaus to lower magnetic fields, the existence of non local resistance and the disappearance of Shubnikov-de Haas peaks.

3.2.1. Anomalous quantum Hall plateaus

In the anomalous quantum Hall effect, the quantization of the Hall resistance depends on the number of detected channels rather than the number of Landau levels in the bulk (see previous section 3.1.3). To perform selective edge state reflection (Fig 3.4(b)), B.W. Alphenaar *et al.* [7] used quantum point contacts (QPCs). In their measurement setup shown in figure 3.4(a), the QPCs defined by gate electrodes are separated by a distance of around hundred of microns [i]. The Hall resistance $R_{\mathrm{H}} = R_{34,52}$ measured without (solid line) and with (dashed line) applied voltage to the gate electrodes is shown in figure 3.4(c). Without depletion by gate electrodes, the contacts behave like ideal probes and the Hall resistance displays the normal quantum Hall effect. When the QPCs are switched on to selectively detect only the outermost edge state, the contact area becomes non ideal and the quantum Hall resistance corresponding to a non spin resolved filling factor $N = 1$ (i.e. $R_{\mathrm{H}} = h/2e$) instead of $N = 2$ (i.e. $R_{\mathrm{H}} = h/4e$) is measured: the Hall plateau $N = 1$ is extended to low magnetic fields. This result was explained by the special behavior of the innermost edge channel which remains strongly decoupled and stays in non equilibrium over a macroscopic distance (more than $80 \, \mu\mathrm{m}$). It was surprising for B.W. Alphenaar *et al.* since non equilibrium was not expected to exist over a distance of the order of the length of the mean free path when the separation between the edge states is not much larger than the magnetic length

---

[i] Such technique was first introduced by B.J. van Wees *et al.* [8] who had a ballistic micrometer structure of two QCPs separated by only $1.5 \, \mu\mathrm{m}$.
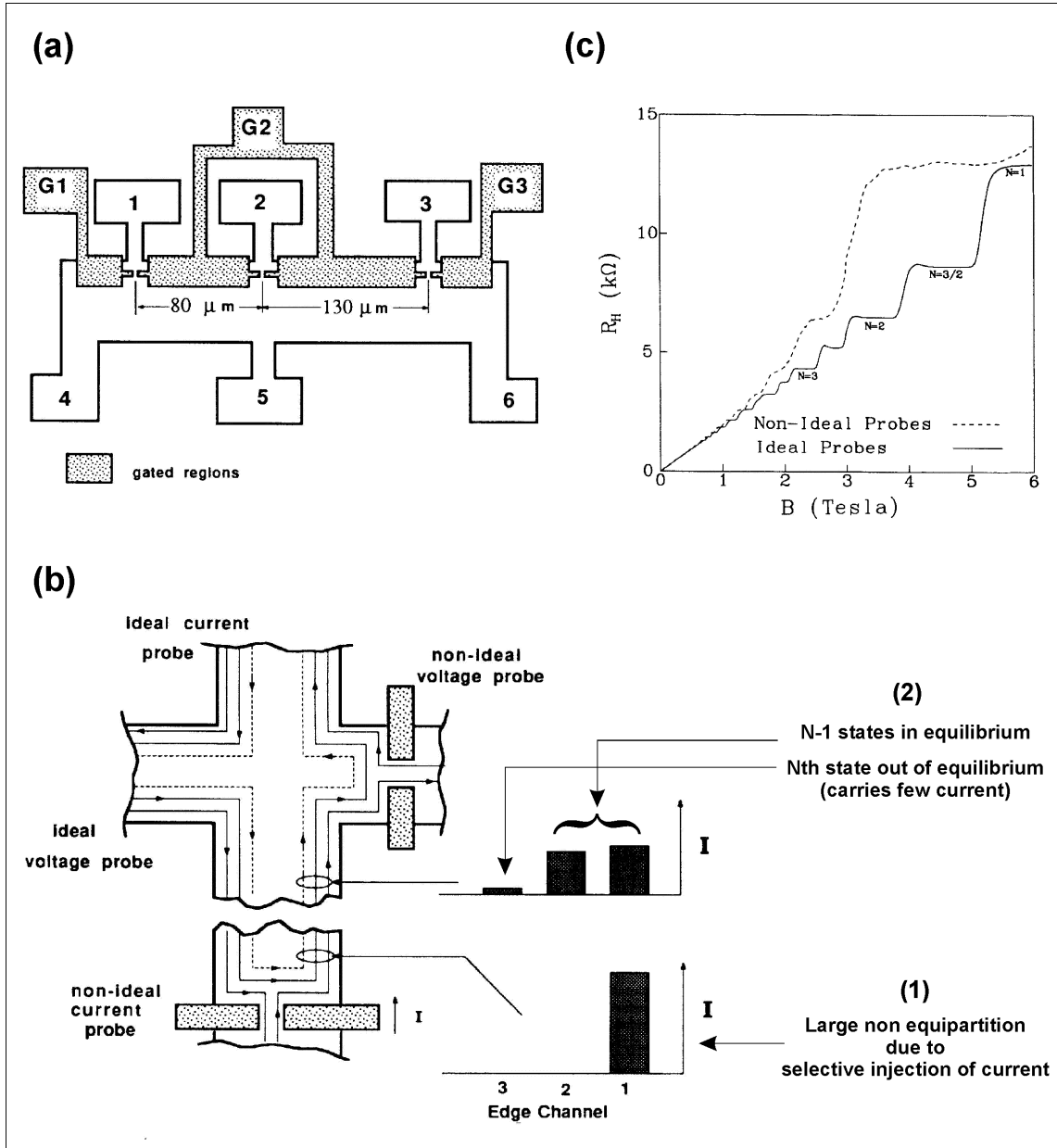
Figure 3.4.: Hall resistance measurement with non-ideal probes (adapted from B.W. Alphenaar *et al.* [7]). **a)** 2DES structure with gate electrodes in front of contacts 1, 2 and 3. **b)** Selective current injection and voltage probing by applying a voltage to the gate electrodes. At the injection (1), the current is exclusively carried by the outermost edge state due to selectively carrier filling. After few microns, the unbalanced distribution of current between the $N - 1$ edge channels is resorbed, except for the innermost one which stays decoupled and carries nearly no current (2). At the voltage probes, the channels are also selectively detected. **c)** Hall resistance measured without and with applied gates voltage (solid and dotted line respectively). In the latter case, the transport curve is extended to lower magnetic fields and a large plateau corresponding to $N = 1$ appears.

3.2.2. Non local resistance

Further features observed on high mobility ungated mesa (Fig. 3.5(a)) were also explained via the assumption of an adiabatic transport. For instance, at a certain value of magnetic field, McEuen *et al.* [9] found a voltage difference between contacts, although these contacts are located far away from the current injecting and sinking contacts (Fig. 3.5(b)). In their device, a non local resistance $R_{37,28}$ (or $R_{37,48}$) is observed if the current is injected via the contacts 3 and 7, and the voltage is probed by the contacts 2 and 8 (or 4 and 6). Following the results of B.W. Alphenaar *et al.* [7] by assuming an adiabatic regime, the transport data is fitted with a network model in which the conductor is divided in different sections (Fig. 3.5(c)). Each section is splitted in two current paths (Fig. 3.5(d) and (e)): the $N - 1$ edge channels which are perfectly transmitted and the decoupled bulk channel. The transmission probability of the bulk channel T_j depends on the disorder and on the magnetic field value. If the longitudinal resistivity associated to the bulk channel is zero, this channel is perfectly transmitted ($T_j = 1$). Otherwise, similar to a barrier (yellow rectangular in Fig. 3.5(c) or (d)), the bulk channel is reflected. In this latter situation, $T_j \neq 1$ depends on the mesa geometry. In agreement with their data, the fit of McEuen *et al.* shows that non equilibrium between edge and bulk currents gives rise to non-local and geometry-dependent behavior of the magneto-resistances.
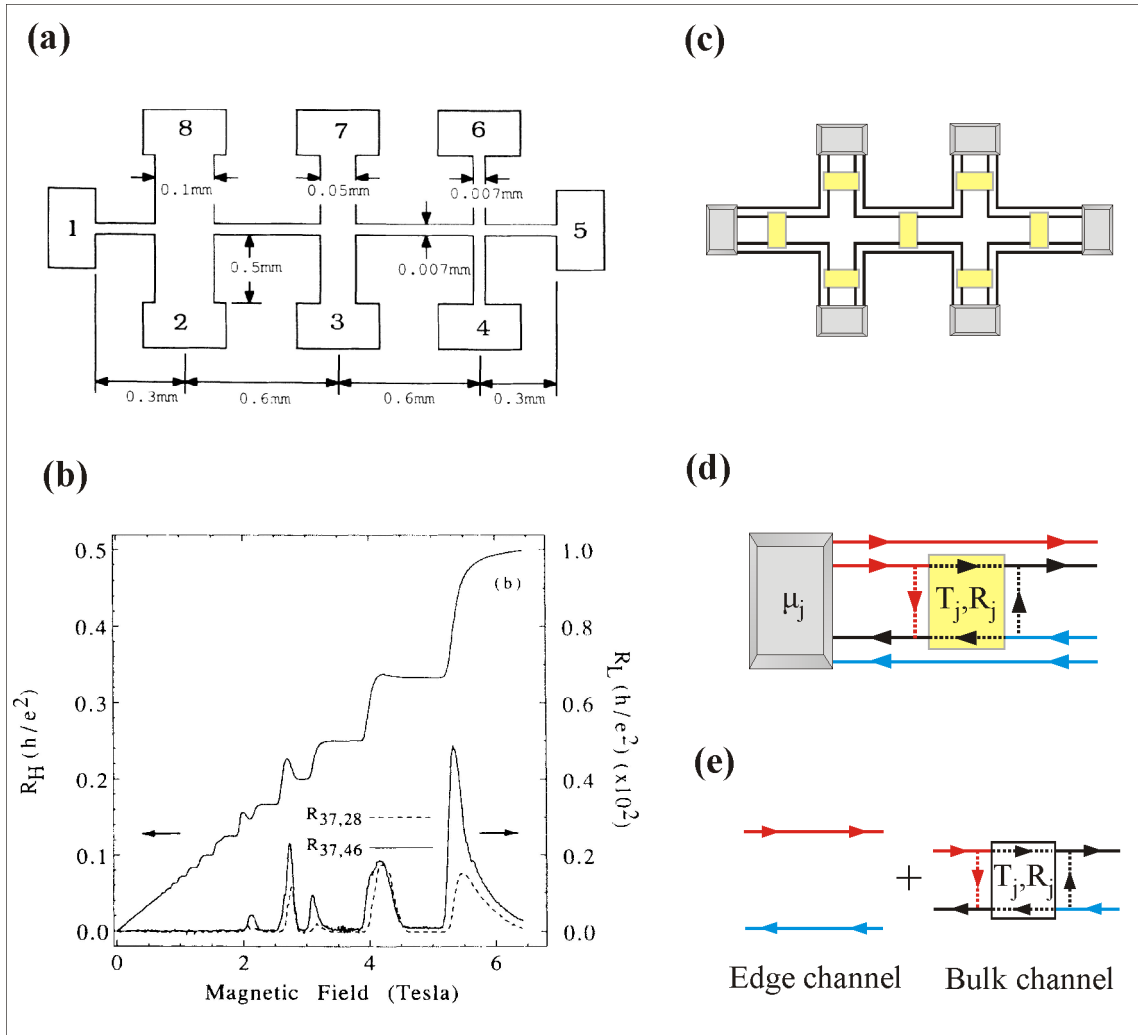
Figure 3.5.: Decoupled network model adapted from McEuen *et al.* [9]. **a)** Geometry of their millimeter size Hall bar. **b)** Measured Hall and non local resistances. **c)** Model of the Hall bar separated in different sections. The yellow regions correspond to barrier that only backscatters the N_{th} channel. **d)** Focus on one particular section named j. The edge channel are perfectly transmitted whereas the bulk channel might be reflected (R_{j}). **e)** Illustration of the perfect decoupling, i.e. edge and bulk are treated separately.

3.2.3. Disappearance of Shubnikov-de Haas peaks

The model of McEuen *et al.* [9, 10] was further elaborated by S. Komiyama *et al.* [11–13] who have also observed non local resistance (see the second frame in Fig. 3.6(a)). In this part, we will focus on another observation that they did on the longitudinal resistance which has been related to an adiabatic transport phenomena (see the first frame in Fig. 3.6(a)). At the dissipative regime of the QHE, they found that some peaks of the SdH oscillations start to disappear [ii]. The authors associate this phenomena to an adiabatic transport since an increasing of the current (or temperature) -which destroys local non equilibrium- restores these peaks and moreover simultaneously decreases the non local resistance. They propose to model their system in the same way as McEuen *et al.* by assuming a decoupling between the edge and the bulk. In additions, they point out that a bulk decoupling with its backscattering will create a difference of chemical potential between edge and bulk states at the mesa boundaries $x = 0$ and $x = L$: $\mu_{N-1} = \mu_L \neq \mu_N$ or $\mu'_{N-1} = \mu'_R \neq \mu'_N$ in Fig. 3.6(b). In order to recover the same edge and bulk chemical potential, they have introduced additional reflections at the boundaries

---

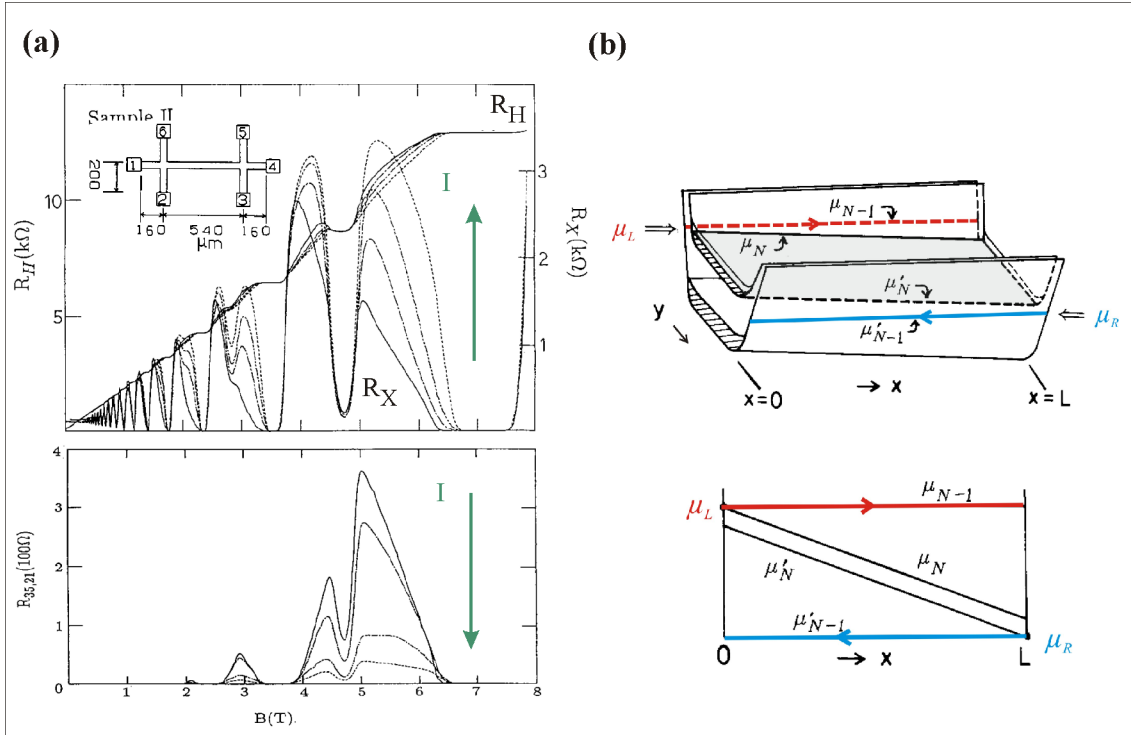[ii] The disappearance of SdH peaks are also observed by other research groups [14–16].

Figure 3.6.: Adapted from S. Komiyama *et al.* [12]. **a)** Magneto-transport measurements on ungated Hall bar. **b)** Distribution of the chemical potential inside a model which assumes a decoupling between bulk and edge.

which are different from the internal reflection of a non ideal contact. Our understanding will propose a physical reason to such boundaries reflection (see last chapter of this thesis).

3.2.4. Conclusion

Several transport features such as the extension of quantum Hall plateaus to low magnetic fields, the existence of a non local resistance and the disappearance of Shubnikov-de Haas peaks have been explained by the assumption of adiabatic transport. Occurring at high magnetic field and in high mobility 2DES, the adiabatic transport is characterized in the edge state picture by a decoupling between edge channels. The decoupling allows to conserve over macroscopic distance a local non equilibrium of the chemical potential at the same mesa edge. The characteristic equilibration length has been intensively studied at the Max-Planck-Institute by G. Müller *et al.* [17] from the experimental side and by Prof. R.R. Gerhardts from the theoretical side.

Two techniques have been used to create adiabatic transport. The first one, working at integer filling factors, selectively populates and detects edge channels via quantum point contacts (QPCs) defined by external gate electrodes (Fig. 3.7(a)). The second technique relies on the intrinsic properties of high mobility 2DES at the transition regime of the quantum Hall effect (Fig. 3.7(b)) in which bulk and edge are decoupled from each other. For local potential probing, the latter technique has the relevant advantage to avoid the disturbance due to a large voltage which would be applied to the gate electrode of QPCs. For this reason, we use the second technique in our voltage probing experiment as it will be described in the next chapters.
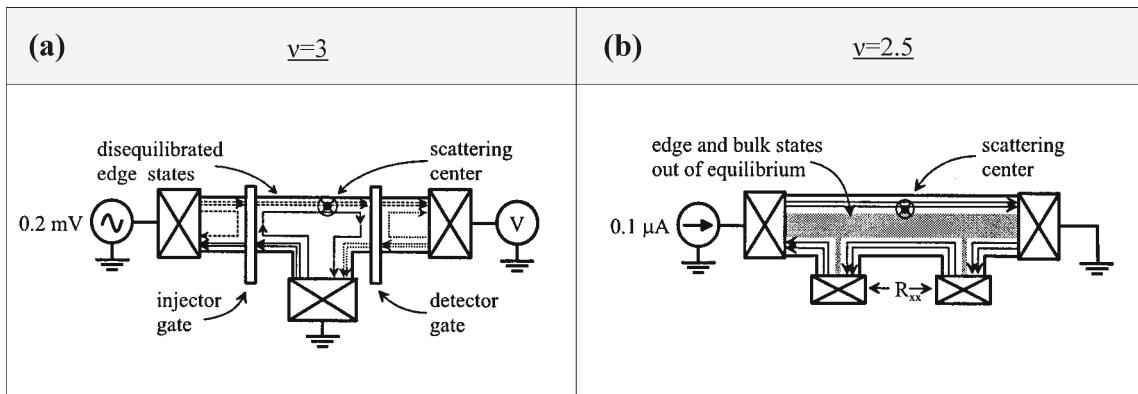

Figure 3.7.: Two different measurement setups which produce adiabatic transport (adapted from *Woodside et al.* [18]). **a)** At the integer filling factor of the QHE, the edge states are reflected by gate electrodes. **b)** At the dissipative regime of the QHE, the bulk and edge states are decoupled due to the intrinsic properties of the sample.

Bibliography

[1] M. Büttiker, Semiconductors and semimetals **35**, 191 (1992).

[2] T. Martin and S. Feng, Phys. Rev. Lett. **64**, 1971 (1990).

[3] M. Büttiker, in *The quantum Hall effect in open conductors* (Academic Press, Orlando, 1992), Vol. 35, p. 244.

[4] M. Büttiker, Phys. Rev. B **38**, 9375 (1988).

[5] S. Komiyama, H. Hirai, S. Sasa, and S. Hiyamizu, Phys. Rev. B **40**, 12566 (1989).

[6] C. Beenakker and H. van Houten, Solid State Physics **44**, 1 (1991).

[7] B. Alphenaar, P. McEuen, R. Wheeler, and R. Sacks, Phys. Rev. Lett. **64**, 677 (1990).

[8] B. van Wees, E. Willems, C. Harmans, C. Beenaker, H. van Houten, J. Williamson, C. Foxon, and J. Harris, Phys. Rev. Lett. **62**, 1181 (1989).

[9] P. McEuen, A. Szafer, C. Richter, B. Alphenaar, J. Jain, A. Stone, R. Wheeler, and R. Sacks, Phys. Rev. Lett. **64**, 2062 (1990).

[10] A. Stone, A. Szafer, P. McEuen, and J. Jain, Annals of the New York academy of sciences **581**, 21 (1990).

[11] S. Komiyama, H. Nii, M. Ohsawa, S. Fukatsu, Y. Shiraki, R. Itoh, and H. Toyoshima, Solid State Communications **80**, 157 (1991).

[12] S. Komiyama and H. Nii, Physica B **184**, 7 (1993).

[13] H. Nii, M. Ohsawa, S. Komiyama, S. Fukatsu, Y. Shiraki, R. Itoh, and H. Toyoshima, Surface Science **263**, 275 (1992).

[14] R. Haug, K. Klitzing, K. Ploog, and P. Streda, Surface Science **229**, 229 (1990).

[15] K. Klitzing, J. Nieder, R. Haug, G. Müller, S. Koch, D. Weiss, and K. Ploog, Semicond. Sci. Technol. **7**, 82 (1992).

[16] B. van Wees, E. Willems, L. Kouwenhoven, C. Harmans, J. Williamson, C. Foxon, and J. Harris, Phys. Rev. B **39**, 8066 (1989).

[17] G. Müller, D. Weiss, S. Koch, K. Klitzing, H. Nickel, W. Schlapp, and R. Lösch, Phys. Rev. B **42**, 7633 (1990).

[18] M. T. Woodside, C. Vale, P. L. McEuen, C. Kadow, K. Maranowski, and A. Gossard, Phys. Rev. B **64**, 041310 (2001).

4. Magneto-resistance measurements showing adiabatic transport features

Adiabatic transport features in the quantum Hall regime are studied in two-dimensional electron systems (2DES) embedded in an AlGaAs/GaAs heterostructure. Hall bars with relatively high mobility and an asymmetrical four-terminal shape are especially investigated. After a brief presentation of the 2DES parameters and the recipe for its contacting, a set of various transport configurations performed on the four-terminal Hall bar are reported in the present chapter. Each of these configurations uses different pairs of current carrying contacts. The results highlight the crucial role played by the orientation of the Hall bar relative to the crystal orientation of the heterostructure.

Contents

4.1. 2DES and geometrical Hall bars parameters

4.1.1. Layer sequence of the AlGaAs/GaAs heterostructure

Two-dimensional electron system studied in this PhD work lies in an epitaxial grown Al-GaAs/GaAs heterostucture (wafer number 102396) which was provided by the group of Werner Wegscheider [i] from the Walter Schottky Institute. AlGaAs/GaAs interface of this wafer is located 60 nm below the surface. At low temperature, electrons coming from silicon donors are accumulated at the interface and they remain confined in a triangular potential [1]. Due to the low electron concentration and the strong confinement, a 2DES is formed (Fig. 4.1 and inset).

---

[i] Now at the university of Regensburg.

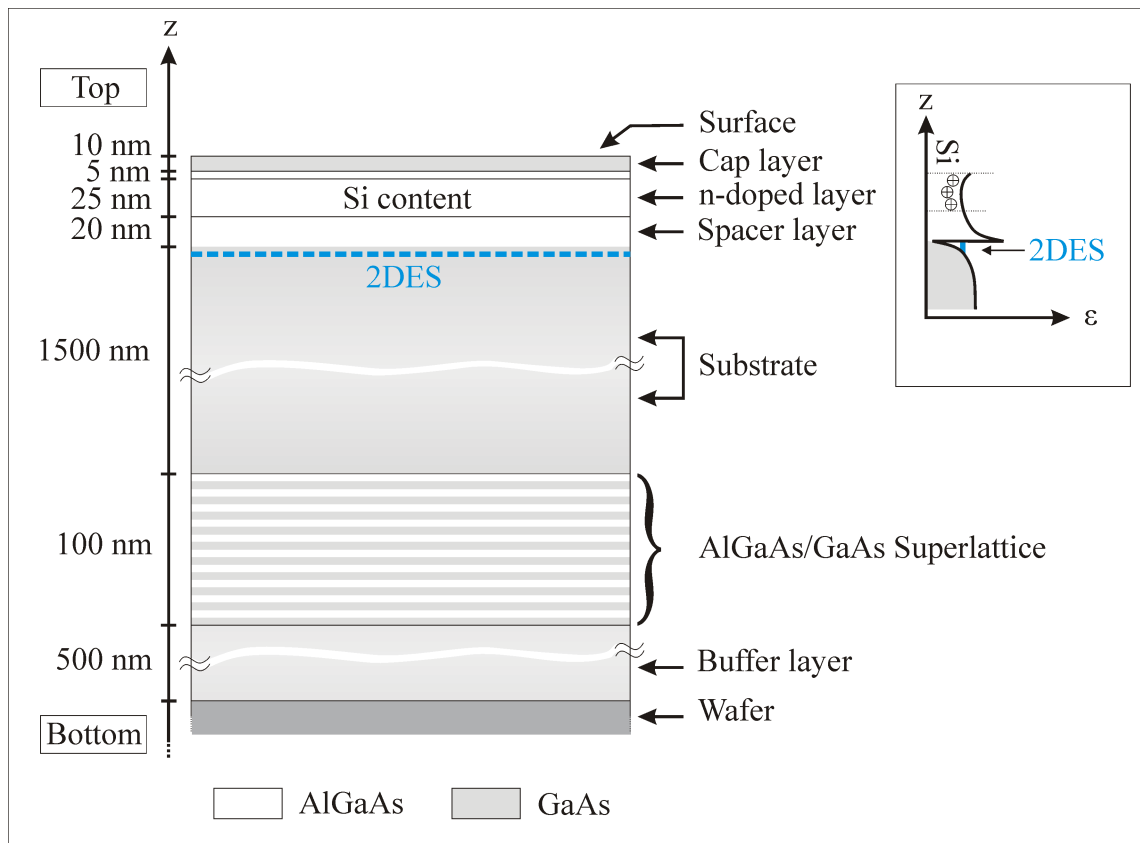Figure 4.1.: Layer sequence of AlGaAs/GaAs heterostructure used in this PhD work. The 2DES lies about 60 nm below the heterostruture surface. For visibility reason the thick GaAs substrate and buffer layers are not in the proper scale. *Insert*: Minimum conduction band energy (ϵ) in the direction of the crystal growth. Electrons are trapped at the AlGaAs/GaAs interface by the triangular shaped confinement.

In this wafer, undoped AlGaAs layer with a thickness of 20 nm is grown to separate the 2DES from the Si-doped AlGaAs layer. Since silicon donors with their positive charges are source of electron scattering, such separation between electron and donors achieves a high electron mobility. A GaAs cap layer at the top of the heterostructure is also added in order to prevent the oxidation of the AlGaAs layer. At the bottom a superlattice of ten AlGaAs/GaAs bilayers suppresses the in-diffusion of wafer impurities. Van der Pauw measurement at $T = 4$ K reveals a carriers mobility of $160\,\mathrm{m^2/V\,s}$ and an electron density of $3.6 \times 10^{15}\,\mathrm{m^{-2}}$ [2, 3] in this wafer.

4.1.2. Hall bar geometries

Hall bar structures are designed by photolithography and wet chemical etching into the heterostructure described in the previous section 4.1.1. The detail of their geometry are depicted in Fig. 4.2. Their width is $10\,\mu$m and their length is $58\,\mu$m (such micrometers size is later required to perform local potential probing since the microscope has a scanning area limited to $20\,\mu$m by $20\,\mu$m). There are two kinds of structures, either with six terminals or four terminals. The six-terminal mesa has two contacts on each side of the Hall bar whereas the four-terminal mesa has two contacts on a single side.
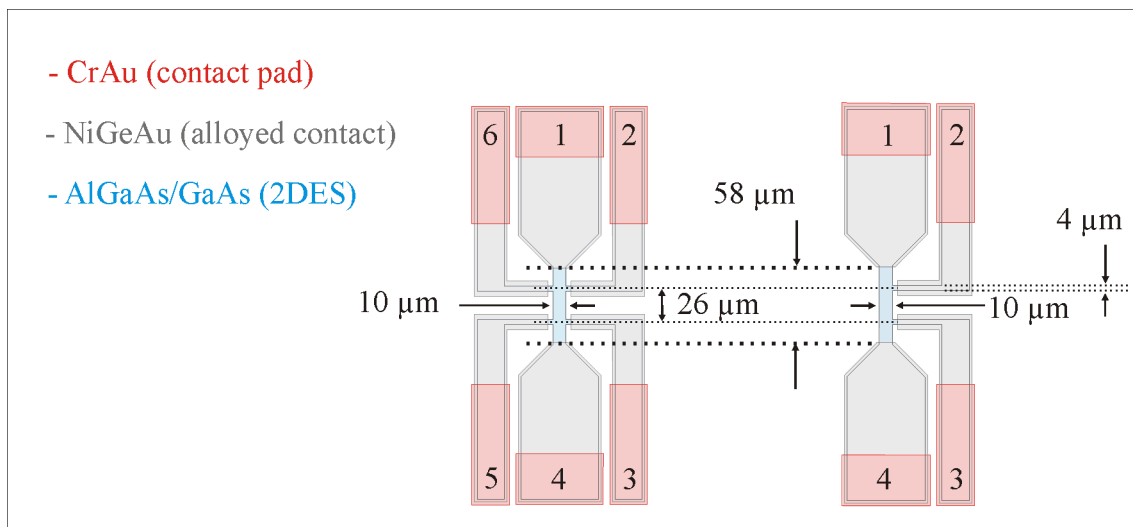
Figure 4.2.: Hall bars with six and four contacts. The AlGaAs/GaAs mesa is etched from the heterostructure (boundaries in blue). NiGeAu contact is alloyed (light blue color). 2DES is remained in the blue area. CrAu pads (red color) are deposited on the top of the contacts to facilitate bonding. The structures have $10\,\mu$m width, $58\,\mu$m length between the contacts 1 and 4, and $22\,\mu$m between the contacts 2 and 3. The contacts 1 and 4 have a borderline with the 2DES of $10\,\mu$m and the contacts 2,3, 5 and 6 have an interface length of $4\,\mu$m.

4.1.3. Recipe to fabricate ohmic contact

The contacts to the 2DES are made by following the recipe of Ulf Graumann *et al.* [4] (see Fig. 4.3) : layers of Au (107.2 nm), Ge (52.8 nm) and Ni (40 nm) are evaporated on the mesa structure and alloyed at $400\,°\mathrm{C}$ during 50 seconds. CrAu pads are added at the end of the contact fabrication to facilitate the bonding to the sample.

To characterize contact's quality, the contact's resistance is extracted via transmission line measurement (TLM) [4–12]. In this method, line structures are fabricated with contacts located at different distances from each other (see Fig. 4.4(a)). I-V characteristics are measured between pairs of contacts in order to determine for every contact pair the two-terminal resistance. This resistance –named also total resistance– has three distinguished contributions as expressed in the following equation:

$$R_{Total}(l) \simeq 2 \cdot R_C + R_{wires} + \frac{\rho_S \cdot l}{W_C}. \tag{4.1}$$

R_C is the resistance of one contact, R_{wires} is the wire resistance of the measurement setup and $R_S = \rho_S \cdot l/W_C$ is the resistance from the 2DES. The set of the two-terminal resistance are plotted versus the corresponding distance between contacts. The two first contributions are not related to the length *l*, only the 2DES resistance does. Therefore the plot of the total resistance versus the distance *l* between contacts should display a linear curve (see Fig. 4.4(b)). By subtracting the wiring resistance and by extrapolating this curve to a virtual zero distance separation, the contact resistance R_C is isolated from the other contributions.
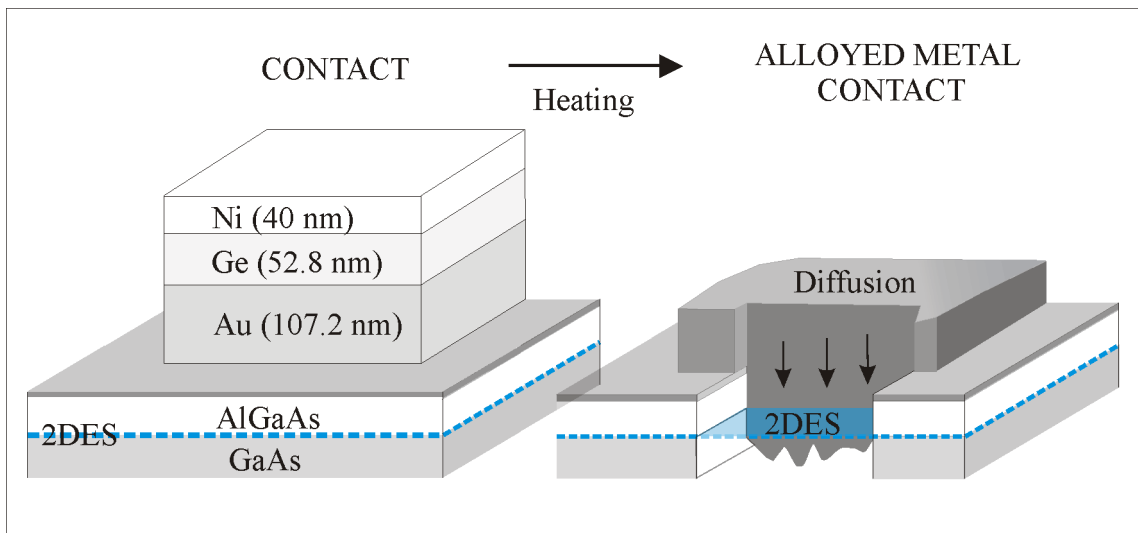

Figure 4.3.: Thin layers of Au, Ge and Ni are evaporated on the AlGaAs/GaAs surface. After heating, the metal mixes with the underlying heterostructure leading to a straight interface lie between the alloyed metal and the 2DES.

Our TLM experimental results are presented in figure 4.5(b) for a $10\,\mu$m wide mesa aligned in [011] or [01-1] crystal direction of the heterostructure (see Fig. 4.5(a)).   Three different samples A, B and C are tested. All these samples are made from the same heterostructure and contact recipe (see section 4.1.4 and 4.1.3). The 2DES located below the contact is suppressed by the NiAuGe contact material. In consequence the contact resistance does not depend on the contact area but it scales linearly with the inverse of the borderline's length between the contact and the 2DES. It will be expressed as $\Omega \cdot$ mm. From these measurements, the contact resistance are found to be ohmic, low resistive and anisotropic: $(0.8 \pm 0.2)\,\Omega \cdot$ mm if the transmission line is oriented in [01-1] direction of the heterostructure and $(0.5 \pm 0.02)\,\Omega \cdot$ mm in the [011] direction. Such anisotropy was already reported by M. Kamada *et al.* [11] and U. Graumann *et al.* [4]. M. Kamada *et al.* find a ratio of 1 to 7 between the contact resistance in [011] direction and the contact resistance in [01-1] direction. The other authors [4] report an anisotropy which might be even much more pronounced with an infinite contact resistance in [01-1] direction although the contact in [011] direction is low resistive. In order to avoid this anisotropy, finger-like contact shape can be used instead of a straight line interface (compared Fig. 4.6(a) to Fig. 4.6(b)). Anisotropy in our contact resistances being low, the contact geometry in this work is intentionally designed in the photolithography mask with a straight line between the contact and the 2DES rather than a finger-like geometry. Later on, in high magnetic field, anisotropy
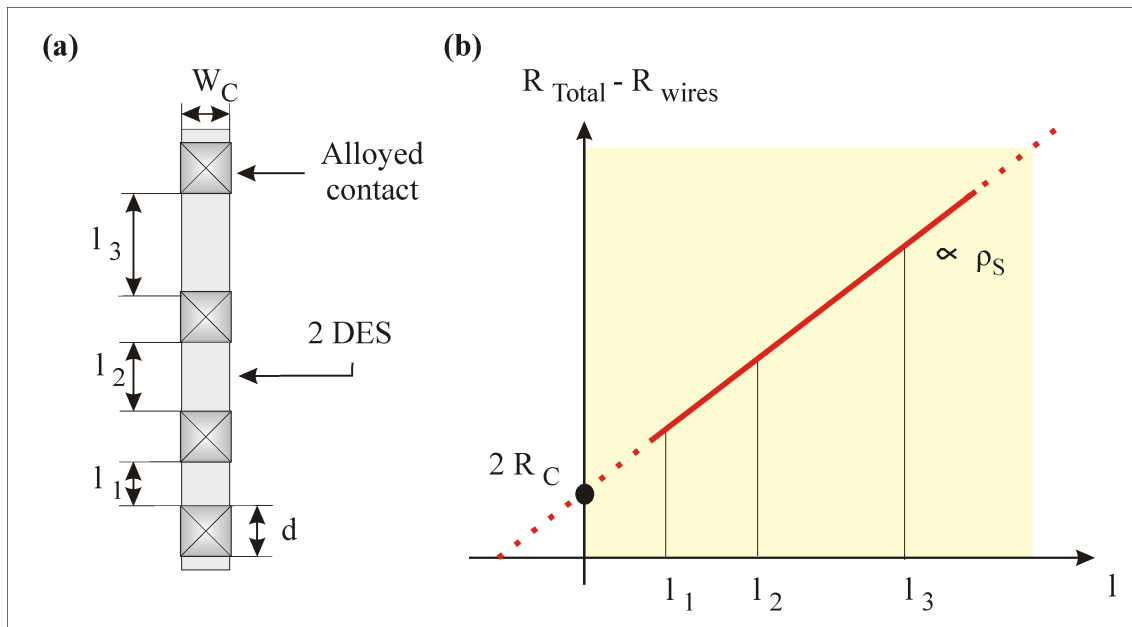

Figure 4.4.: **a)** Setup of transmission line measurement with contacts at different distances from each other. **b)** Expected linear behavior of two-terminal resistance with respect to the contact distance l.
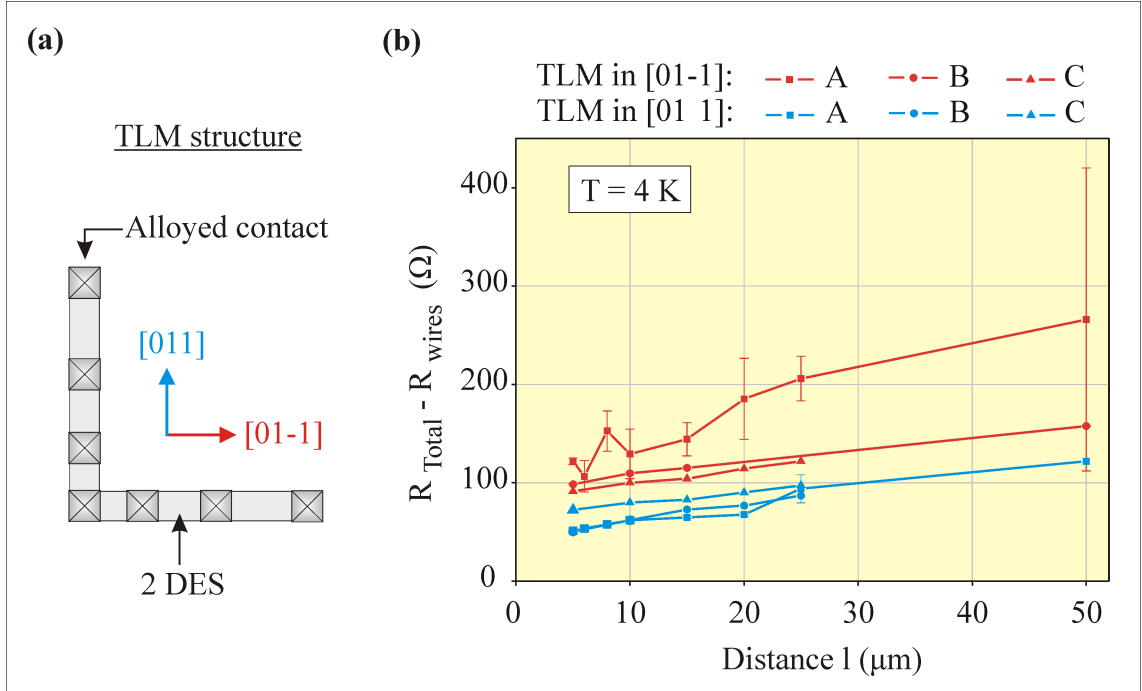
Figure 4.5.: Transmission Line Measurements (TLM) at $T = 1.4$ K performed by Yvonne Boose under my supervision. **(a)** [011] and [01-1] crystal direction are used. **(b)** Total resistance versus contact distance l. Three different samples A, B and C are tested. Each point of this plot corresponds to a linear fit of two-terminal I-V characteristic showing ohmic behavior. An anisotropy of the contact resistance between the two orientations is visible: TLMs show lower contact resistance in [011] direction than in [01-1] direction. The sample A presents broader error bars because the data are averaged over three different cooling processes. A horizontal error bar can be added to account for the uncertainty related to the distance between contacts ($\Delta l \approx 0.4\,\mu$m).

will nevertheless be relevant in our measurements. Finally, as the slope of the TLM curve is proportional to ρ_S/W_C, the sheet resistivity of the 2DES might be extracted from transmission line measurement. With $W = 10\,\mu$m and $\rho_S/W_C \simeq 1550\,\Omega/\mu$m in [011] direction, the sheet resistivity ρ_S is evaluated to $\rho_S \simeq 15\,\Omega/\square$.

4.1.4. Parameters of the 2DES determined at low magnetic field

At low magnetic field, magneto-resistance measurements of structured Hall bars inform on the 2DES sheet density n_s and on its carrier mobility μ (see section 1.2). The six-terminal Hall bar is the most adequate for these purposes since the transversal and longitudinal voltage drops are accessible in a simple geometrical way. Measurements are performed via the injection of
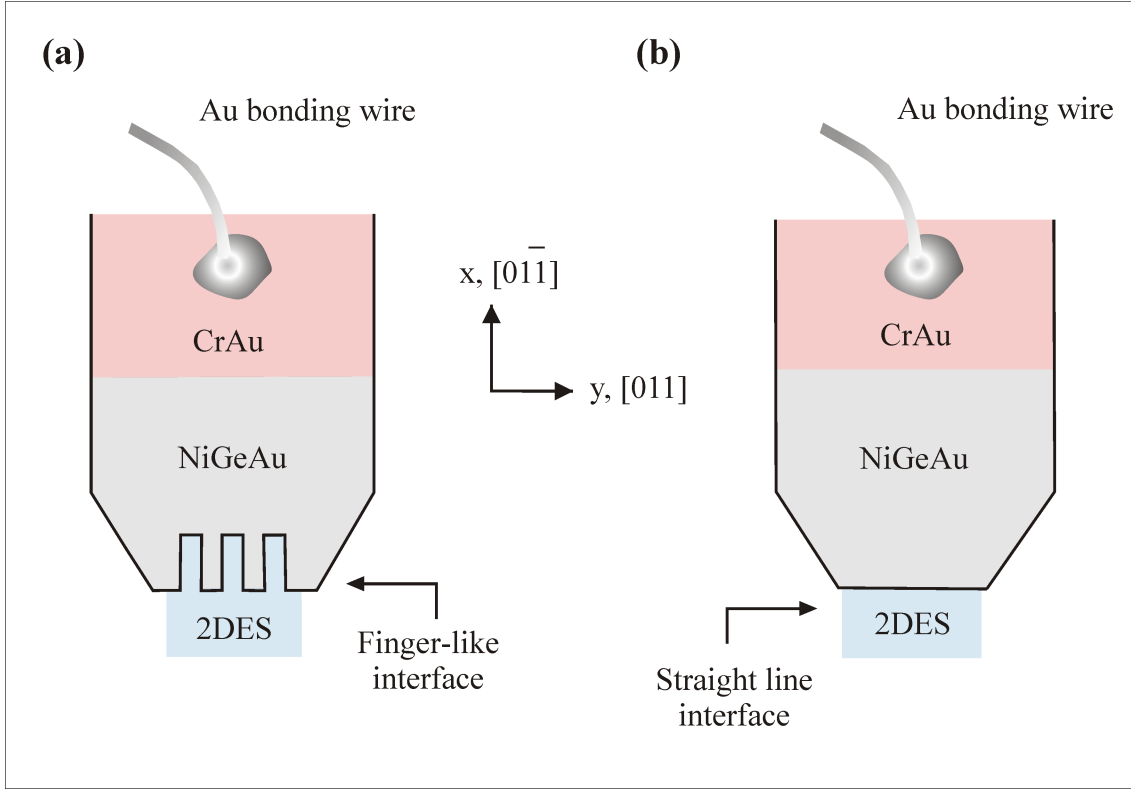
Figure 4.6.: Schematics of NiAuGe contact to the 2DES with CrAu layer on the top in order to attach gold bonding wires. **(a)** To assume low contact resistance in the hard contacting [01-1] direction, finger-like interface might be used which owns a borderline with certain fractions oriented in [011] direction and in [01-1] direction. **(b)** Contact with straight line borderline as used in this PhD work.

net current I to the contacts 1 and 4. The voltage drop is probed between contacts 2 and 6 in the case of Hall resistance, or between 2 and 3 in the case of longitudinal resistance. Measured Hall resistance $R_{14,26} = V_{26}/I$ and longitudinal resistance $R_{14,23} = V_{23}/I$ are presented in the figure 4.7(b). Since $R_{14,26} = \rho_{xy} = B/(n_s \cdot e)$, the linear slope of the classical Hall resistance gives the sheet density n_s:

$$n_s = \left(e \cdot \frac{dR_{14,26}}{dB} \right)^{-1}.$$

This sheet density is found to have a value of $n_s = 3.6 \times 10^{15}\,\mathrm{m}^{-2}$. Depending on cooling processes, n_s value can have a change of 5 %. The carriers mobility is calculated with the Drude model from the longitudinal resistance $R_{14,23} = \rho_{xx} \cdot L/W$ around zero magnetic field:

$$\mu = [n_s \cdot e \cdot \rho_{xx}(B \simeq 0)]^{-1}.$$

In Fig. 4.7, $R_{14,23}(\text{B} \simeq 0) = 36\,\Omega$ which means a sheet resistivity of $\rho_{\text{xx}} = 13.8\,\Omega/\square$ and therefore a carrier mobility of $130\,\text{m}^2/\text{V}\,\text{s}$. The value is consistent with the one found with transmission line measurement in section 4.1.3.

Further parameters of the 2DES can be obtained from the density and the mobility. For instance the Fermi velocity $v_{\text{F}} = \hbar\sqrt{2\pi n_{\text{s}}}/m_{\text{eff}}$ and the scattering time $\tau = (\mu \cdot m_{\text{eff}})/e$. Fermi velocity and scattering time give the mean free path $l_{\text{mfp}} = v_{\text{F}} \cdot \tau = 12\,\mu\text{m}$. This mean free path compared to the sample size allows to estimate the type of transport occurring at zero magnetic field: either diffusive or ballistic. In our sample, the transport is quasi-ballistic at $B=0$ since $W \leq l_{\text{mfp}} \leq L$. The scattering time informs also on which B range the quantum effects start to be relevant: Landau levels and its associated SdH oscillations appear when the cyclotron orbit completes a full circular trajectory without being disturbed by a scattering event, i.e. $\omega_{\text{c}}^{-1} \ll \tau$ (or $B \gg \mu^{-1}$). In figure 4.7, the SdH oscillations start at $B = 400$ mT. At this field, $\hbar\omega_{\text{c}} = 0.7\,\text{meV}$ and $\omega_{\text{c}}^{-1}(= 1\,\text{ps}) \ll \tau(= 48\,\text{ps})$. The measured value of the sheet density is used as the reference number to calculate the Landau level filling factor ν (see section 1.4). Following the equation $\nu = \phi_0 \cdot n_s \cdot B^{-1}$ with $\phi_0 = h/e = 4.1357 \cdot 10^{-15}\,\text{m}^2 \cdot \text{T}$, at each magnetic field value corresponds a precise Landau level filling factor ν for a fixed electron density n_s. In our 2DES, $B_\nu \cdot \nu \simeq 14.5\,\text{T}$ and $\nu = 1$ corresponds to $B_{\nu=1} = 14.5$ T.
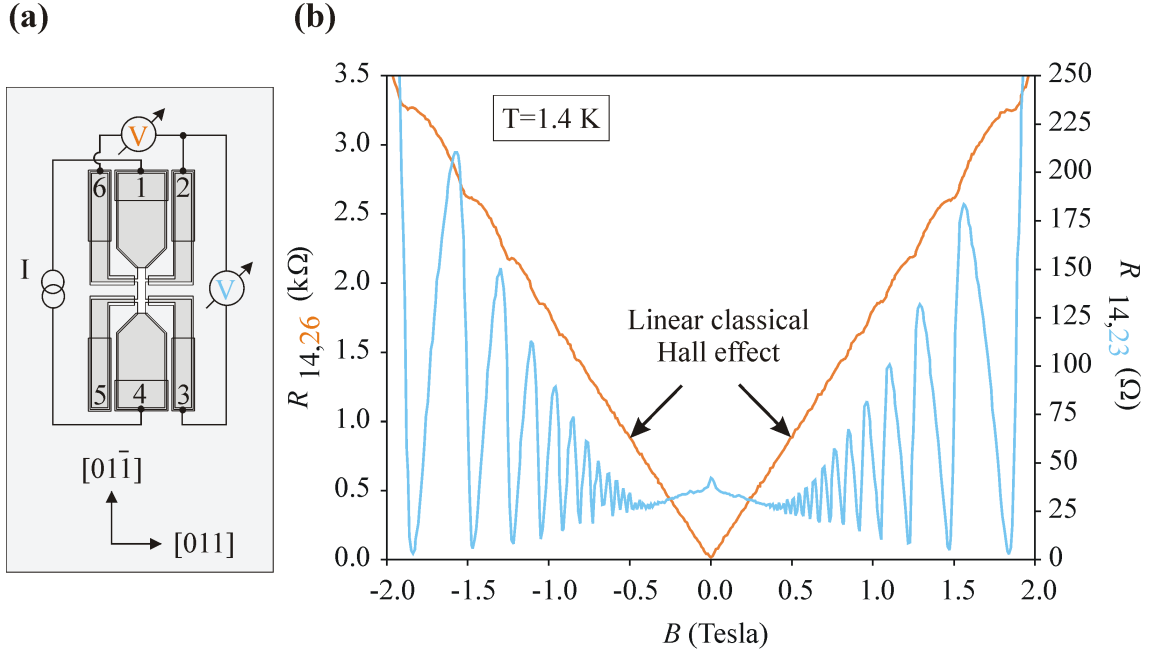
(a) **(b)**

Figure 4.7.: Hall and longitudinal resistances in six-terminal Hall bar. **a)** Setup configuration with current carrying contacts 1 and 4. **b)** At low B, the Hall resistance varies linearly and the longitudinal resistance has three different types of transport regime (see Appendix D).

All parameters of our 2DES are summarized in the table 4.1.

parameter	$n_{\rm s}$	$E_{\rm F}$	$v_{\rm F}$	$\lambda_{\rm F}$	μ	τ	$l_{\rm mfp}$
value	$3.6 \cdot 10^{15}\,{\rm m}^{-2}$	12.8 meV	$2.5 \cdot 10^5 {\rm m/s}$	42 nm	127 ${\rm m}^2/{\rm V\,s}$	48 ps	12 μm

Table 4.1.: Various parameters of the two-dimensional electron system used in this work.

4.2. Magneto-transport measurements

The next part presents transport measurements performed on four- and six-terminal Hall bars. The transport is driven with a 100 nA fixed current. A lock-in is used as a function generator to apply a 1 V excitation at 13.43 Hz through a 0.01 % calibrated 10 MΩ resistance in series with the sample. The input of the lock-in detects the difference of voltage at this frequency.

4.2.1. Comparison of the transport in six- and four-terminal Hall bar

After the same cooling process at $T = 1.4$ K, the magneto-resistances of the six-terminal Hall bar are compared to the magneto-resistances of the asymmetrical four-terminal Hall bar. In both cases, the current is injected via the contacts 1 and 4 (see mesa drawn in figure 4.8(a)). At magnetic fields corresponding to an integer filling factor, the usual quantum Hall effect is observed in the six-terminal Hall bar: the Hall resistance $R^{Six}_{14,26}$ has plateaus with quantized values and the longitudinal resistance $R^{Six}_{14,23}$ is simultaneously null (orange and light blue curves in Fig. 4.8). For the four-terminal Hall bar, Shubnikov-de Haas peaks (SdH) in between $\nu = 2$ and $\nu = 3$ (or $\nu = 4$ and $\nu = 5$) are not present in the longitudinal resistance $R^{Four}_{14,23}$ (dark blue) although they are visible in the six-terminal Hall bar. Such disappearance is reviewed in the literature as an adiabatic effect due to a non equilibrium situation between edge and bulk states (see section 3.2.3). The measurement of the two-terminal resistances $R^{Four}_{14,14}$ also shows anomaly. Hall plateaus are located at lower magnetic field values. For example, the plateau corresponding to $\nu = 2$ is measured around $\nu \simeq 3$. Both features - disappearance of SdH peaks and deviation of Hall plateau, are an intrinsic effect since no external electrode gate is added to the sample. Furthermore these effects are generic since similar results are obtained on other small and high mobility Hall bars contacted with a straight interface between the alloyed metal and the 2DES (see section 4.3).

(a)
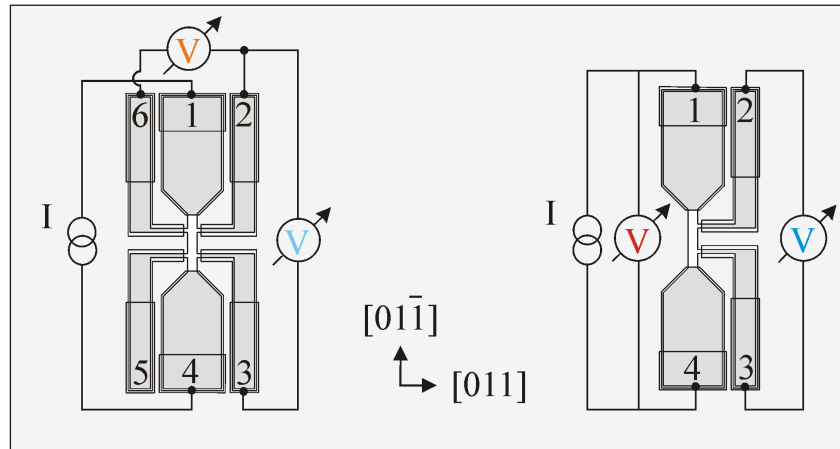
(b)
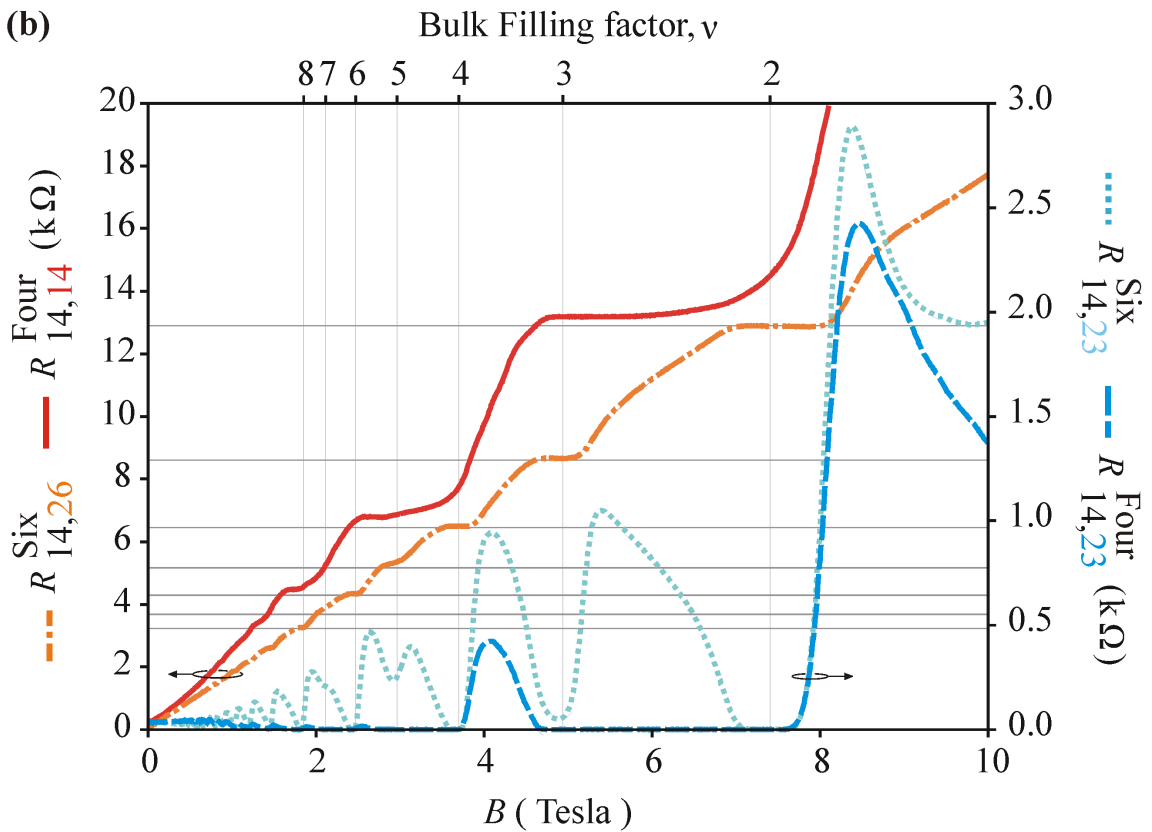
Figure 4.8.: Comparison between magneto-resistances measured at $T = 1.4$ K in a six- and four-terminal Hall bar. **a)** *Setup configuration.* The current is injected in both Hall bars via contacts 1 and 4 and the longitudinal resistance is measured with the contacts 2 and 3. **b)** *Transport results.* Around $\nu = 2.5$, a plateau in the two-terminal resistance $R_{14,14}^{Four}$ (red curve) is visible which is not present in the Hall resistance $R_{14,26}^{Six}$ (orange curve). Simultaneously, SdH peaks are suppressed in the longitudinal resistance $R_{14,23}^{Four}$ (dark blue curve).

4.2.2. Four-terminal Hall bar measured in four different configurations

The disappearance of some SdH peaks and the deviation of the Hall plateaus in the total resistance encourage to characterize in detail the four-terminal Hall bar. The purpose of this section is to present four configurations (Fig. 4.9) which were used to perform transport in the four-terminal Hall bar. Each of these configurations (a)-(d) has different current carrying contacts. These contacts allow to measure different two- and four-terminal resistances:

(a) Current injection via contacts 1 and 4 with a borderline between the contact and the 2DES oriented perpendicularly to the [01-1] direction of the heterostructure. The longitudinal resistance is obtained by measuring the voltage drop between the contacts 2 and 3.

(b) Current injection via contacts 2 and 3 with a borderline oriented perpendicularly to the [011] direction. A four-terminal resistance is measured via recording the voltage drop between
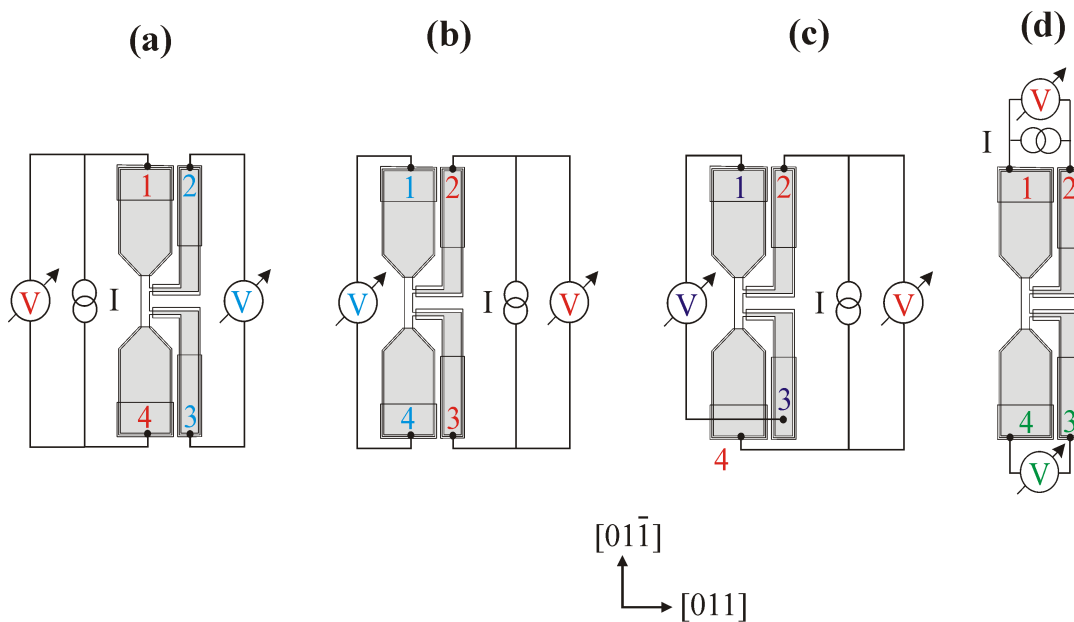
Figure 4.9.: Four configurations used to measure magneto-resistances in the four-terminal Hall bar. The total two-terminal resistances are measured via the contacts labeled with a red number. The four-terminal measurement uses in addition the contacts labeled with a blue color. **a)** Configuration with current carrying contacts 1 and 4 which gives the longitudinal resistance $R_{14,23}$. **b)** Configuration with current carrying contacts 2 and 3 which allow to extract the resistance $R_{14,23}$ with the character of a longitudinal resistance. **c)** Γ-like shape configuration to obtain the atypical Hall resistance $R_{24,13}$. **d)** Probing of the non local resistance $R_{12,34}$.

the contacts 1 and 4. This geometry is special since a C-like shape for the current path is obtained instead of the usual I-like shape used in the case (a). Nevertheless this four-terminal resistance $R_{14,23}$ owns the properties of a longitudinal resistance.

(c) Current injection via contacts 1 and 3. The voltage is probed in between contacts 2 and 4. This arrangement allows to measure a kind of Hall resistance since the voltage drop is probed between two opposite mesa edges where in between the current passes by. Different from the usual cross-like arrangement, this measurement is called as an atypical Hall resistance.

(d) Current injection via the contacts 1 and 2. The voltage is probed with the contacts 3 and 4. The value of $R_{12,34}$ is denoted as non local resistance.

4.2.2.1. Current injected in [01-1] direction

The first measurement corresponds to the arrangement which was compared to the six-terminal Hall bar (see section 4.2.2). It is plotted in figure 4.10(b) for the two magnetic field orientations. The magneto-resistances display similar curves for positive and negative magnetic field. The plateaus corresponding to an even filling factor are not present in the two-terminal resistance $R_{14,14}$ (red curve). In addition, the plateaus related to an odd filling factor are found at lower magnetic fields: the plateau with its value of $h/2e^2 \approx 12.9\,\text{k}\Omega$ appears around $\nu = 3$ instead of $\nu = 2$. The offset of resistance $R_{offset} \approx 400\,\Omega$ above the quantized resistance is due to the two contact resistances ($2 \times 80\,\Omega$) and to the two wire resistances ($2 \times 130\,\Omega$). As expected, this offset is close to the zero field resistance. Concerning the longitudinal resistance (blue curve), some of the peaks in the SdH oscillations are absent. It is visible in between $\nu = 2$ and $\nu = 3$ where the longitudinal resistance stays zero, or in between $\nu = 4$ and $\nu = 5$ where the vanishing is also visible.
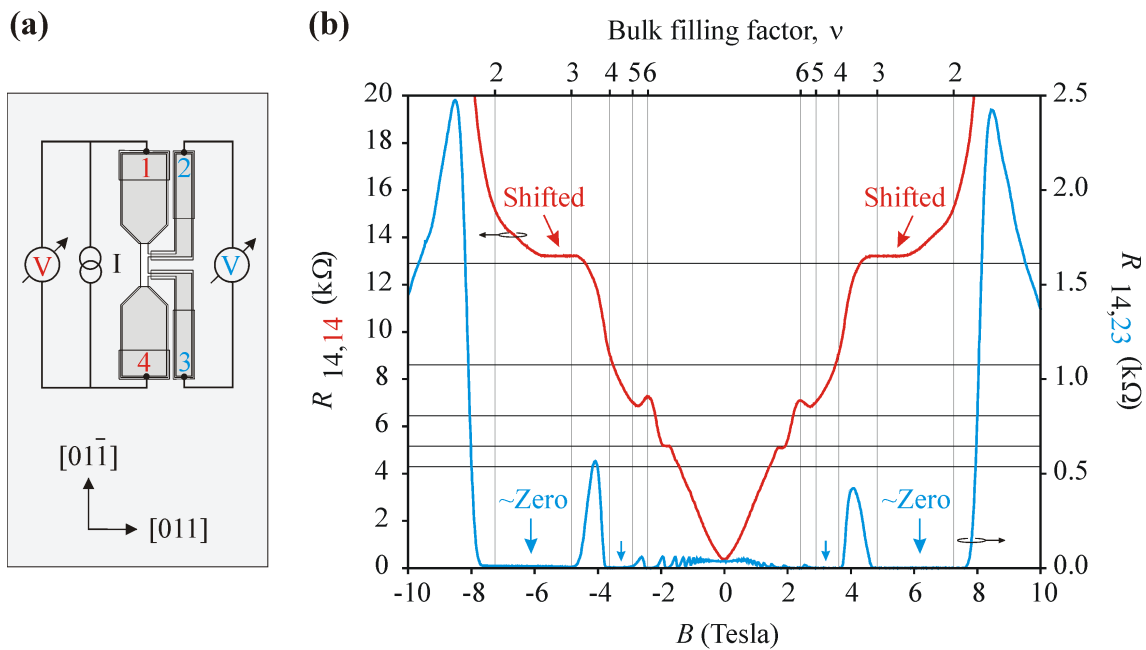

Figure 4.10.: **a-b)** Same measurement data presented in figure 4.8 but for positive and negative magnetic field. The plateaus of the total resistance $R_{14,14}$ are found at lower magnetic fields than expected. In the longitudinal resistance $R_{23,14}$, the SdH peaks disappear in between $\nu = 2$ and 3, and in between $\nu = 4$ and 5.

4.2.2.2. Current injected in [011] direction

The contacts used to inject the current and to probe the voltage in the previous configuration are now interchanged. In this new setup, the current carrying contacts 2 and 3 own a border-line with the 2DES oriented perpendicular to the [011] orientation of the heterostructure. In the previous configuration, the borderline was perpendicular to the [01-1] direction. The two terminal-resistance $R_{23,23}$ shows plateaus at the expected integer bulk filling factor: for example, the Hall plateau with resistance $h/2e^2$ appears at $\nu = 2$ as it is expected from $h/\nu e^2$ (red curve in Fig. 4.11(b)). The four-terminal resistance measured via the voltage difference between the contacts 1 and 4 presents the characteristic of a longitudinal resistance. The same disappearance of SdH peaks as in the previous configuration is found.
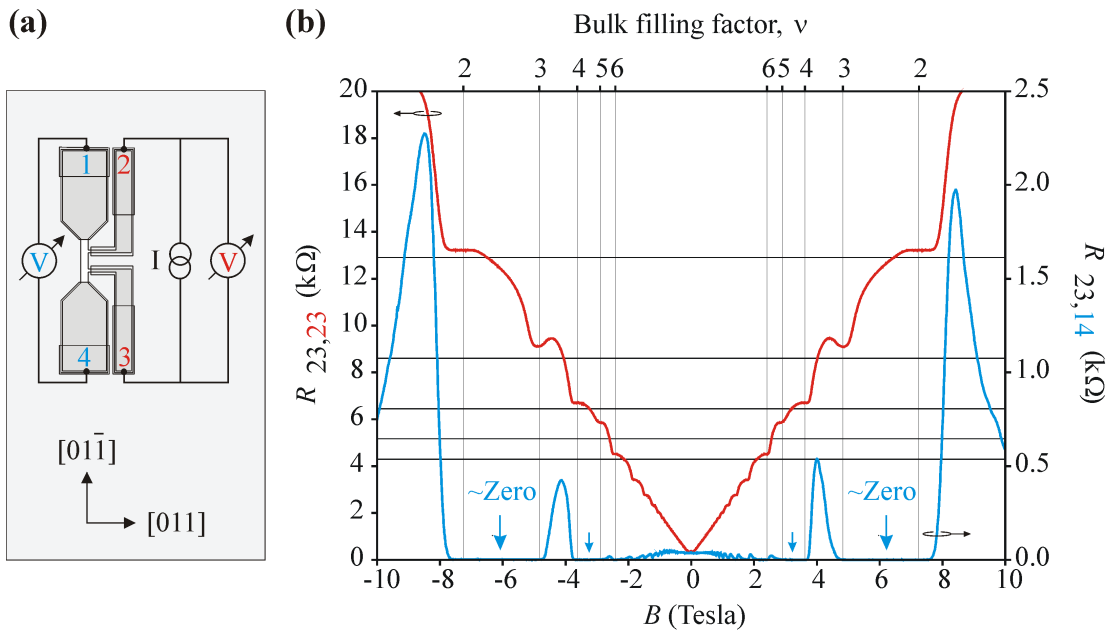
Figure 4.11.: **a)** The current carrying contacts are the contacts 2 and 3. **b)** The plateaus of the total resistance $R_{23,23}$ are located at the expected filling factor corresponding to the averaged bulk density. In the resistance $R_{23,14}$ which has the character of a longitudinal resistance, the Subnikov-de Haas peaks are absent in between $\nu = 2$ and 3, and in between $\nu = 4$ and 5.

4.2.2.3. Atypical Hall configuration

In the third setup –named atypical Hall resistance measurement, the current is injected via the contacts 2 and 4, and the Hall voltage is recorded via the contacts 1 and 3 (Fig. 4.12(a)). The Hall plateaus in the two-terminal resistance $R_{24,24}$ shown a similar deviation as in the configuration with current injection via contacts 1 and 4 (compared red curves in Fig. 4.12(b) and in

Fig. 4.10(b)). The Hall resistance $R_{24,13}$ is different in positive and in negative magnetic field (dark blue curve). An unexpected broad plateau appears for negative magnetic field between $\nu = 3$ and $\nu = 2$. It is not present for positive magnetic field.
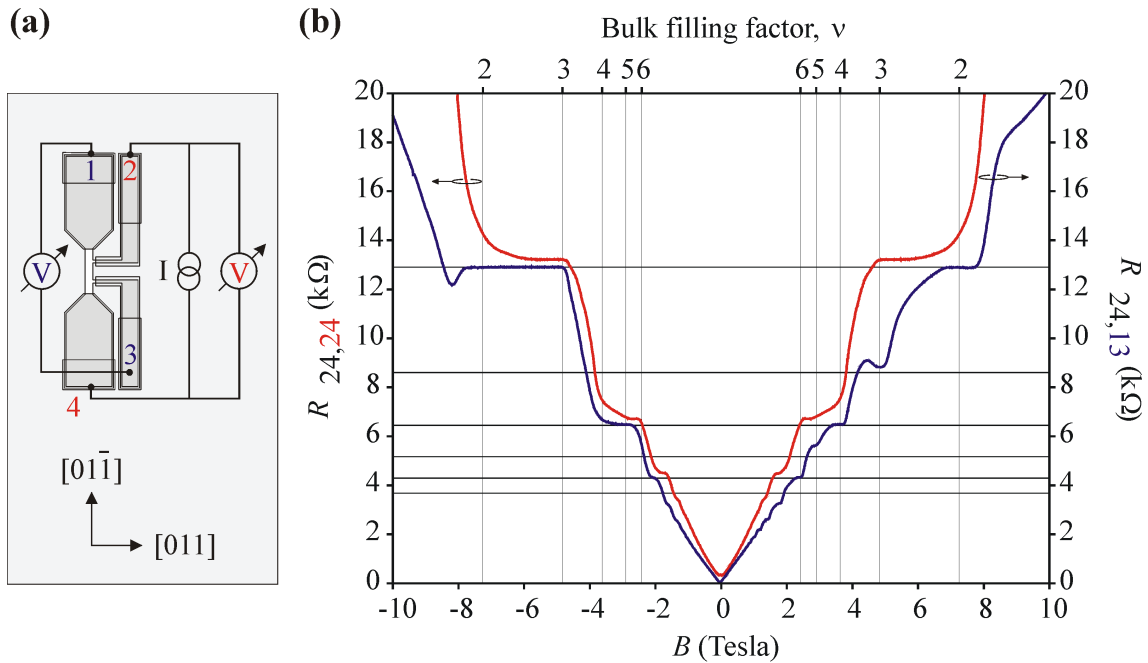
Figure 4.12.: **a)** Atypical Hall configuration. **b)** The plateaus in $R_{24,24}$ are deviated to lower filling factor whereas the Hall resistance $R_{24,13}$ shows an asymmetrical behavior with respect to the magnetic field direction: for negative magnetic field, an unexpected broad plateau is found in between $\nu = 3$ and $\nu = 2$ which is not visible at positive B. This asymmetry persists at higher filling factors.

4.2.2.4. Non local configuration

In the last configuration, the current is injected via the contacts 1 and 2. The potential is probed at the contacts 3 and 4 (Fig. 4.13(a)). The voltage is measured away from the current trajectory expected at zero magnetic field. This configuration corresponds to the measurement of a non local resistance. In the figure 4.13(b), the two-terminal resistance $R_{12,12}$ (red) is deviating from the expectation. The non local resistance $R_{12,34}$ (green) is null at positive B but it does not stay null below -0.7 T.

(a)

(b)
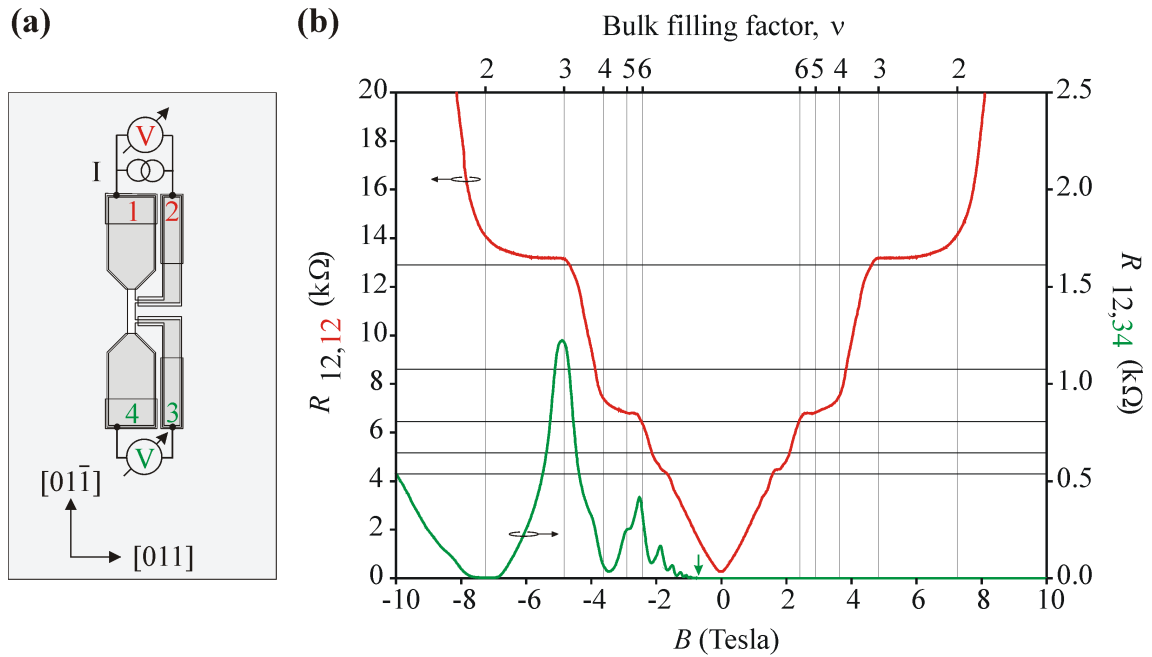
Figure 4.13.: **a)** The four-terminal resistance $R_{12,34}$ is obtained by probing the voltage between the contacts 3 and 4 located away from the current injecting contacts 1 and 2 (non-local configuration). **b)** The plateaus of the total resistance $R_{12,12}$ are found at lower magnetic fields. The value of $R_{12,34}$ is null at positive magnetic field. Near -0.7 Tesla, a non local resistance starts to appear at negative B.

4.2.3. First summary

The measurements performed in the four-terminal Hall bar correspond to adiabatic transport features described in the previous chapter 3. All four-terminal resistances show adiabatic transport, i.e. the disappearance of SdH peaks, a non local resistance and the deviation of Hall plateaus. The two-terminal resistance reveals also an anomalous Hall effect if at least one contact is oriented with its borderline perpendicularly to the [01-1] direction of the heterostructure (red curves in Fig. 4.10(b), 4.12(b), 4.13(b)). Only the two-terminal resistance with current injection in [011] direction does not present deviation in its Hall plateaus (red curve in Fig. 4.11(b)). Such results advertise that the transport is anisotropic with respect to the crystal orientation as it is with the contact resistance (section 4.1.3).

4.3. Further magneto-transport measurements

4.3.1. Magneto-resistance on Hall bars oriented by $90°$ to each other

To confirm the presence of transport which is anisotropic with respect to the crystal orientation of the heterostructure, two similar Hall bar structures oriented by $90°$ to each other are prepared on the same wafer and on the same cooling sample (see pictures in figure 4.14). The transport are performed in a dilution fridge at 26 mK [ii]. The two-terminal resistances are measured by a

_____

[ii] This very low temperature is nevertheless not important.
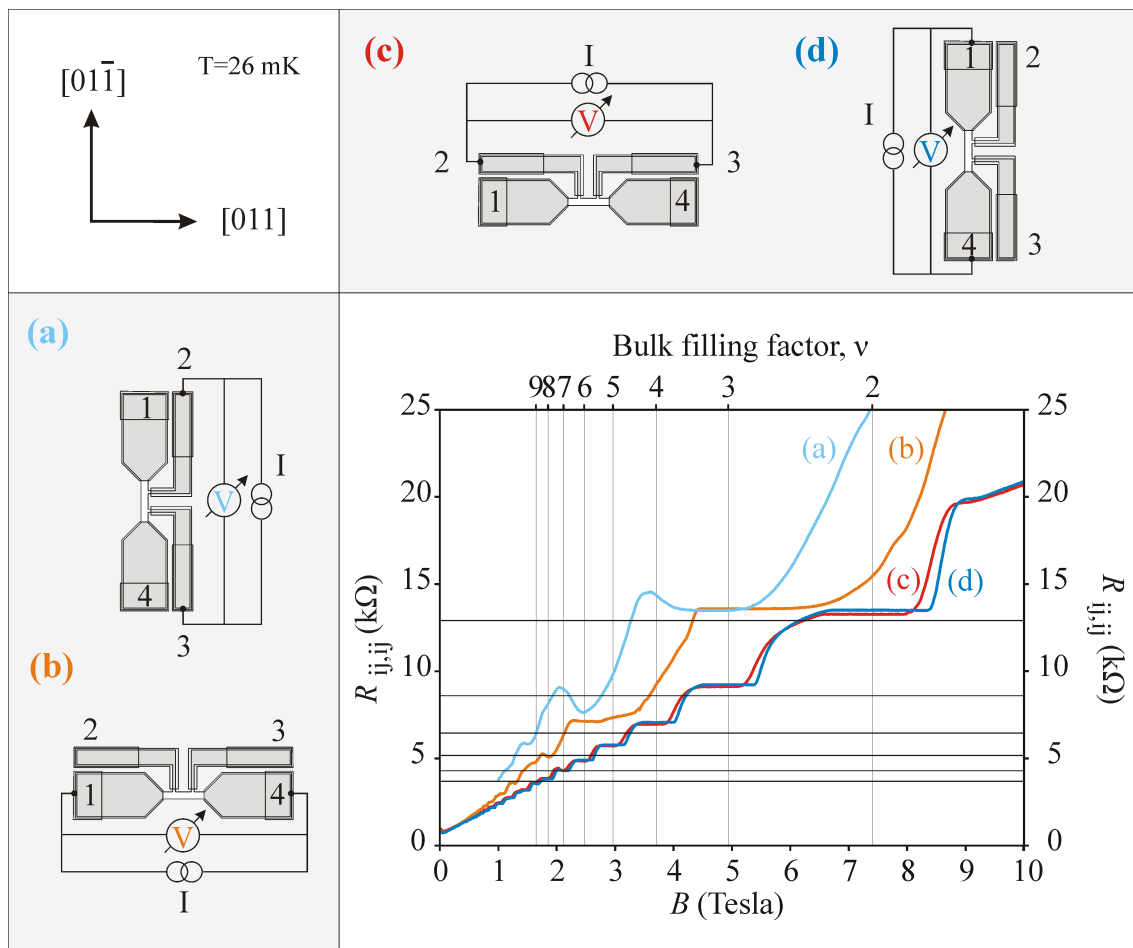
Figure 4.14.: Two-terminal measurements for Hall bar oriented in [011] or [01-1] direction of the heterostructure. If the current is injected and ejected along [011], the plateaus in the two-terminal resistance $R_{ij,ij}$ appears at lower B (case (a) and (b)). In the other case, the resistances show Hall plateaus at the expected bulk filling factors (case (c) and (d)).

current injected either via the contacts 1 and 4 (cases (b) and (d)) or via the contacts 2 and 3 (cases (a) and (c)). If the current is injected and ejected in [011] crystal direction of the heterostructure (curves (c) and (d)), the two-terminal resistance gives the expected quantification. At contrary, the curves (c) and (d) with the current injected and ejected in [01-1] direction display a deviation in the plateaus position to lower B. Turning the Hall bar with respect to the

Figure 4.15.: Two-terminal and atypical Hall resistance for Hall bars oriented by $90°$ to each other. In both cases, the two-terminal resistance (orange or light blue) is deviated to lower magnetic field, whereas the Hall resistance (red or dark blue) shows different curves depending on the magnetic field sign. Broad Hall plateau around $\nu = 2.5$ or around $\nu = 3.1$ is visible only for negative B.

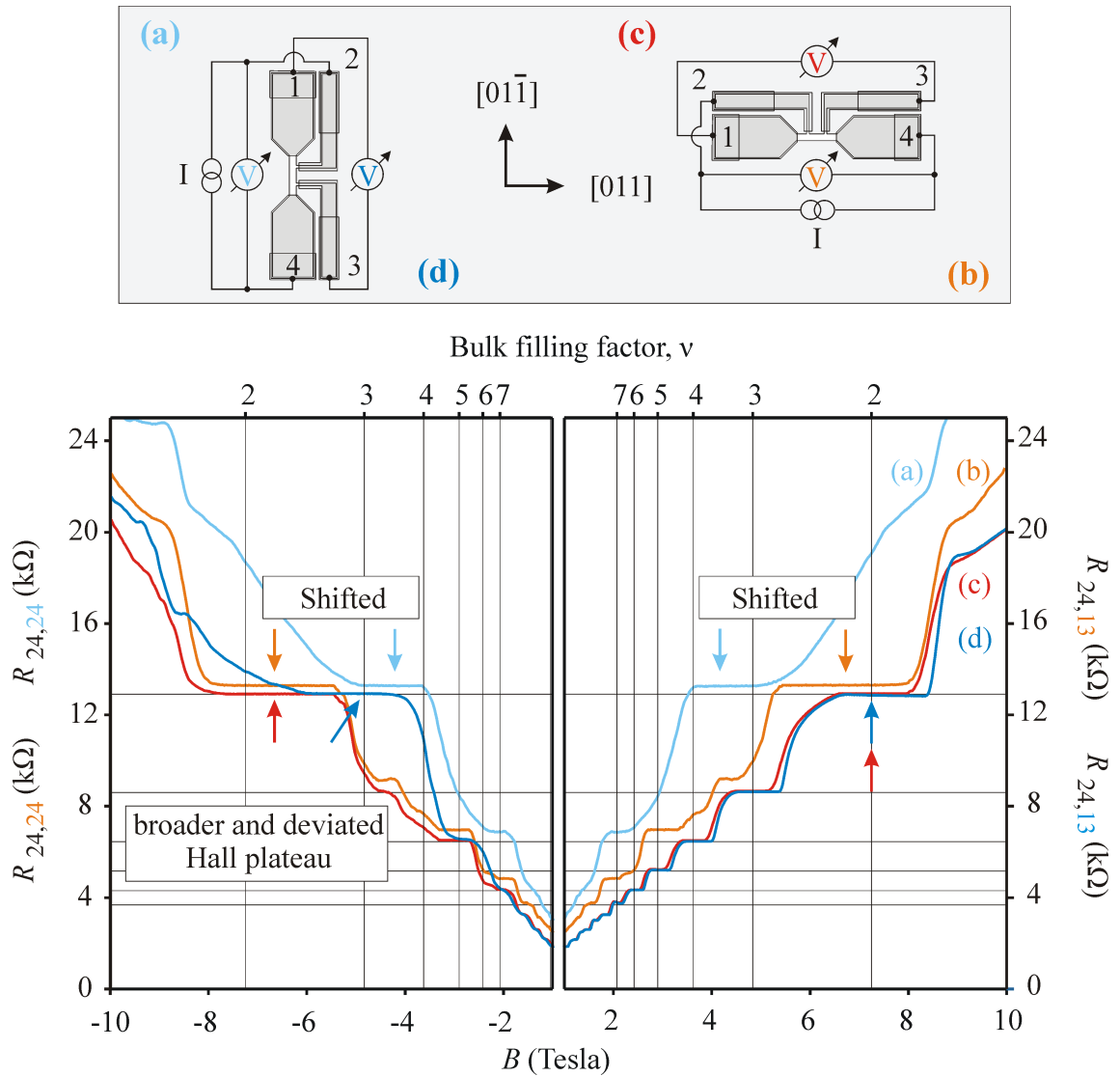crystal axis is in conclusion not equivalent for the two-terminal measurements. These results confirm the importance of the crystal orientation. The next step is to investigate if the adiabatic features exist in these two Hall bars. For this purpose, atypical Hall resistance is performed on both mesas oriented by $90\,^\circ$ to each other. The results are plotted in figure 4.15. Both atypical Hall resistances $R_{24,13}$ (dark blue and red) are different in positive and negative magnetic field. The Hall plateaus at $\nu = 2$ are also broaden and deviate to lower negative B. In conclusion, adiabatic features are present as they were found in the transport measurements of the previous sample (section 4.2.2.3).

4.3.2. Five-terminal Hall bars

Hall bars owning three contacts along the mesa edge are also tested (Fig. 4.16(a)). *All* contact junctions have $10\,\mu\mathrm{m}$ width. In this new geometry, adiabatic properties are still visible: the SdH peaks between $\nu = 2$ and $\nu = 3$ disappear in the longitudinal resistance $R_{15,24}$ (light blue) and the Hall resistance $R_{14,25}$ (dark blue) is asymmetrical with respect to the magnetic field sign (see broad plateau between -5 and $-8\,\mathrm{Tesla}$ in figure 4.16(b)). These features are similar to the ones observed and described in section 4.2. The results prove that the length ($10\,\mu$m or $4\,\mu$m) or
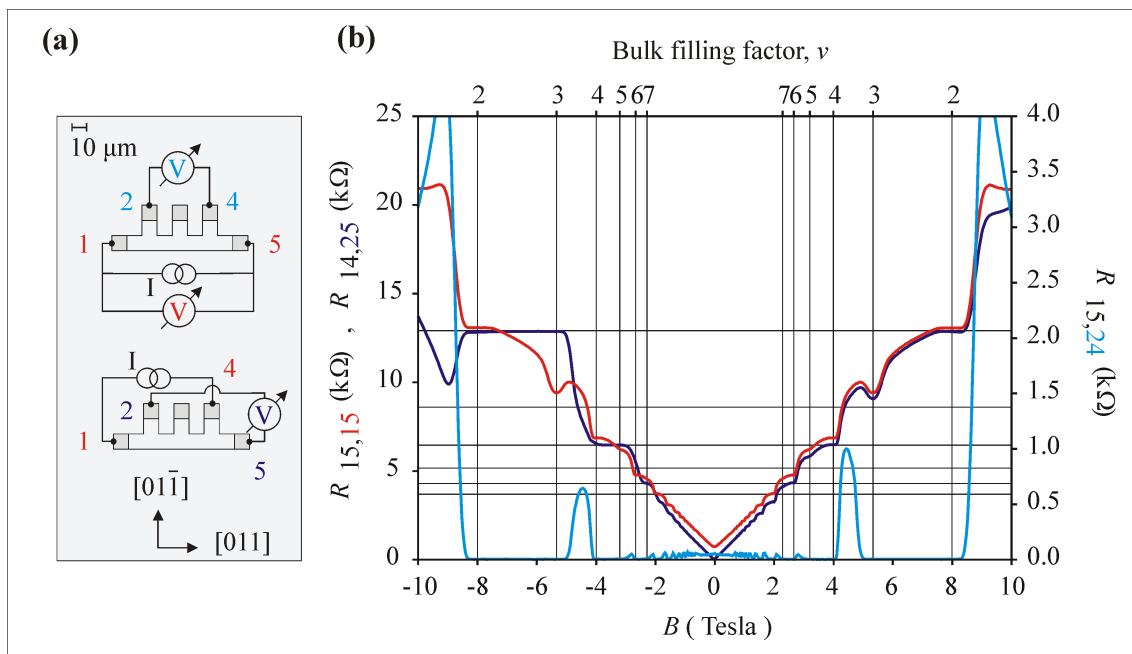

Figure 4.16.: **a)** Five-terminal Hall bar in two different measurement setup. **b)** The SdH peak at $\nu = 2.5$ is missing in the longitudinal resistance $R_{15,24}$ (light blue) and the Hall resistance $R_{14,25}$ (dark blue) is different in positive and negative magnetic field.

the number of contact borderline is irrelevant if the borderlines of these voltage probing contacts are oriented perpendicular to the [01-1] crystal direction of the heterostructure.

4.4. Conclusion

Adiabatic transport features as the disappearance of SdH peaks or non local resistance have been observed in four-terminal Hall bars with micrometers size and high mobility 2DES. Different samples with various mesa geometries and orientations relatively to the heterostructure crystal have been tested. The result demonstrates that the adiabatic behavior is generic. The two-terminal measurements also indicate that IQHE at the right filling factors is only obtained if both source and drain contacts have their borderlines oriented perpendicularly to the [011] direction of the heterostructure. Such anisotropic behavior has the same tendency as the contact resistance. Indeed, contact resistance is higher if its borderline is perpendicular to the [01-1] direction of the heterostructure. In the edge state picture, this deviation of the Hall plateaus in the two-terminal resistance would be considered as a reflection of one edge state at the contact since the position of the Hall plateaus is deviated from nearly one filling factor: $R_{2\text{pts}} = h/(\nu - 1)e^2$. Nevertheless all the contacts used in this work are strictly ohmic at zero magnetic field and low resistive as proved by transmission line measurement. In order to determine the microscopic origin of these deviations, the four-terminal Hall bar showing adiabatic features will be characterized in the next chapter via local Hall potential probing.

Bibliography

[1] F. S. T Ando, A.B. Fowler, Rev. Mod. Phys. **54**, 437 (1982).

[2] L. van der Pauw, Philips Research Reports **13**, 1 (1958).

[3] L. van der Pauw, Philips Technical review **20**, 220 (1958).

[4] U. Graumann, *Praktikumsarbeit: Ohmsche Kontakt zu zweidimensionalen Elektronensystemen* (Max-Planck-Institut für Festkörperforschung, Stuttgart, 1998).

[5] S. Cohen, in *VLSI electronics* (Academic Press. Inc., New York, 1986), Vol. 13, Chap. 4, p. 87.

[6] H. Berger, J. Electrochem. Soc. **119**, 507 (1972).

[7] H. Berger, Solid-State Electronics **15**, 145 (1972).

[8] G. Reeves and H. Harrison, IEEE Electron Device Lett. **18**, 111 (1974).

[9] M. D. Feuer, IEEE Trans. Electron Devices **32**, 7 (1985).

[10] D. look, IEEE Electron Device Lett. **8**, 162 (1987).

[11] M. Kamada, T. Suzuki, F. Nakamura, Y. Mori, and M. Arai, Ann. Phys. (Leipzig) **49**, 1263 (1986).

[12] H. Bühlmann and M. Ilegens, J. Electrochemical. Soc. **138**, 2795 (1991).

5. Local probing of the Hall potential in the adiabatic regime

Adiabatic transport features as disappearance of Shubnikov-de Haas peaks or non local resistance are generically obtained with a high mobility four-terminal Hall bar of micrometer size (chapter 4). Such features are explained in the literature via the assumption of a non equilibration between adjacent edge states with different chemical potentials (chapter 3). A recent description of the integer quantum Hall effect in terms of metal-like compressible strip and insulator-like incompressible strip has been possible via the probing of the local Hall potential (section 1.7.2). Similar measurements on our higher mobility samples should allow to develop a microscopic description of the adiabatic regime in terms of these strips.

The following chapter presents the local probing of the Hall potential for the four configurations presented in the previous chapter: current injection and ejection in [011] direction or [01-1], atypical Hall resistance and non local transport. For these four configurations, the determination of Hall potential via scanning force microscopy [i] should allow a better understanding of the special transport features as the disappearance of SdH peaks, the appearance of non local resistance, or the asymmetry of the Hall resistance with respect to the magnetic field sign.

---

[i] The same cryogenic scanning force microscope as Peter Weitz [1] and Erik Ahlswede [2] is used to measure the potential distribution.

Contents

5.1. Potential distribution of the four measurement configurations showing adiabatic transport features

The four configurations studied by transport measurements in the previous chapter are reviewed via local probing of their potential distributions. The transport experiments were made by driven a fixed current (100 nA). The current is obtained via a 1 Volt AC voltage excitation at 13.43 Hz applied to a 10 MΩ resistance. For the local probing technique, a $15\,\mathrm{mV}$ AC voltage excitation at 3.43 Hz is applied. Therefore, the terminology will change from "applied current to the contact..." to "applied voltage to the contact...". The physics stays nevertheless the same. At such high voltage, the magnitude of the net current is still small and the system stays in the linear regime. Measurements of the potential profiles for a $1\,\mathrm{mV}$ voltage excitation give the same distribution. This statement was verified in the configuration presented in the section 5.1.2. The signal being more noisily, the voltage probing are obtained in higher voltage excitation in order to increase the ratio signal/noise. All the measurements have been done two times with the voltage excitation applied to either one or the other contact. The result of the potential distribution for one case to the other corresponding only to an inversion between low and high potential. For simplicity, only one case is shown in the following.

5.1.1. Configuration with voltage applied via contacts with a borderline perpendicular to [011]

The Hall bar is oriented with its length in the [01-1] crystal direction. The borderline between the contacts 2 and 3 is therefore aligned perpendicularly to the [011] direction. The voltage excitation is applied to the contact 2, and the contact 3 is at the ground potential. The measured Hall potential distribution is shown in figure 5.1 for positive and negative magnetic field. The result is qualitatively similar to E. Ahlswede data obtained in middle mobility samples [3]. On an interval between two integer filling factors, three types of Hall potential profiles are distinguishable: a linear potential drop, two equal potential drops at the opposite mesa edges and a drop in the bulk area (see section 1.8). The inversion of the magnetic field orientation just exchanges the potential polarity between the two mesa edges: low (high) voltage for the upper edge and high (low) voltage for the lower edge at positive (negative) magnetic field (see Appendix C for explanation). A quantitative difference compared to the measurement of E. Ahlswede is the shift to lower value of the filling factor at which the different profiles appear. In both case, the determination of the filling factor is always done via transport measurement performed at the same cooling down as the potential probing. An explanation for the shift may be due to the high mobility of the sample (see the work of A. Siddiki [4]).
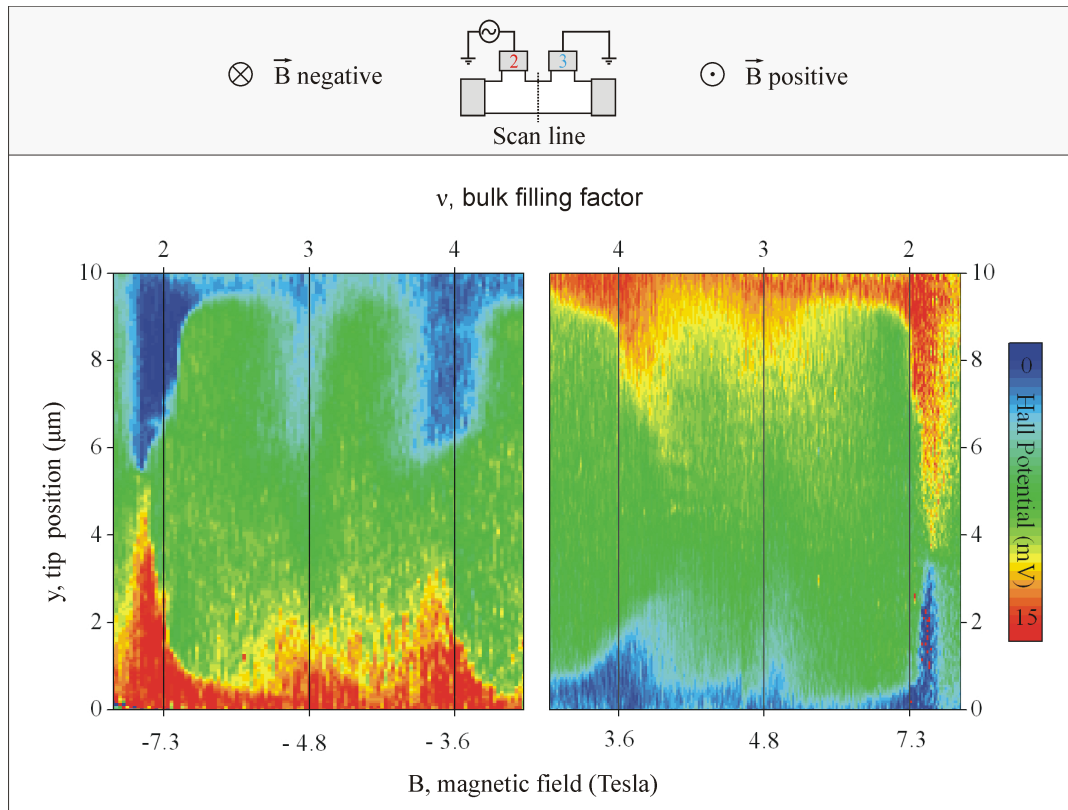
Figure 5.1.: Local Hall potential measured at different magnetic fields in a four-terminal Hall bar in which the voltage excitation is applied between the contacts 2 and 3. The scan line is oriented in the 10 μm width direction of the mesa and located between the contacts 2 and 3. For all magnetic field, the Hall potential distribution along the width of the sample shows henceforth the same behavior at the two mesa border. For instance close to $\nu = 2$ the potential have an equal drop at the two edges.

5.1.2. Configuration with voltage applied contacts with a borderline perpendicular to [01-1]

The figure 5.2 corresponds to the situation in which the voltage excitation is applied to the contact 1, and the contact 4 is grounded. This situation presents transport with a quantization of the two-terminal resistance at an unexpected filling factor (Fig 4.10). For the Hall potential distribution, a clear change is found compared to the previous configuration. Between the bulk filling factor $\nu = 2$ and $\nu = 3$, a drop from a high potential (red color) to a low potential (blue color) occurs only at the lower mesa edge without voltage probing contacts. Such drop associated to one innermost incompressible strip is interpreted as a direct probing of a robust non
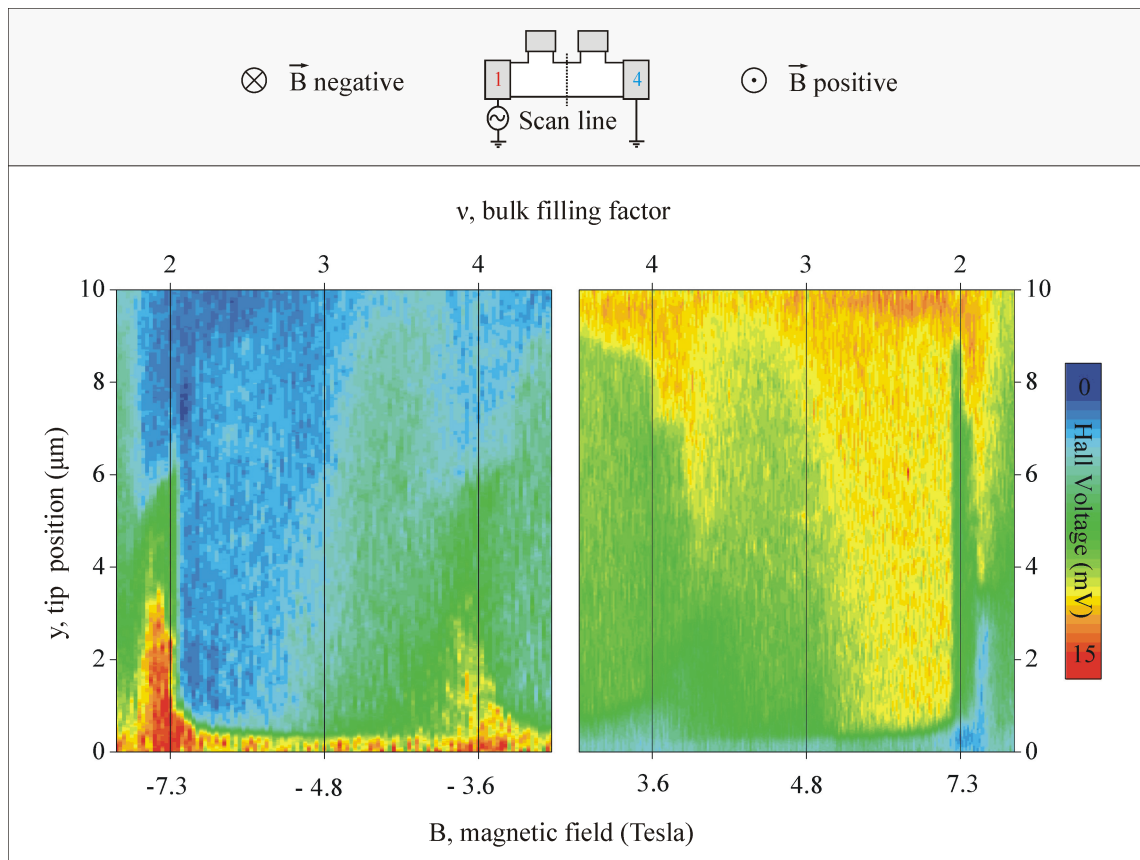
Figure 5.2.: Same experiment as in Fig 5.1 but the voltage excitation is now applied to the contacts 1 and 4. The distribution of the Hall potential for the positive magnetic field is similar compared to the distribution at negative magnetic field. Only the potential magnitude is inverted. Outstanding fact: the Hall potential drop appears only at one mesa edge between $\nu = 2$ and $\nu = 3$.

equilibrium situation between compressible regions with different electrochemical potentials [ii]. The conservation of this single drop has been continuously measured along a large distance of $20\,\mu\mathrm{m}$ and it is expected to be maintained along the complete length of the Hall bar (see next chapter).

[ii] The SFM measurements record the electrostatic potential variation in non-equilibrium (with current flow) relatively to the equilibrium situation (without current). The potential variation follows the electrochemical potential since the electron density varies few.

M.T. Woodside *et al.* [5] has locally probed by scanning force microscopy such single potential drop at one mesa edge (Fig 5.3(a)). In their case, the non equilibrium situation was extrinsically produced by a gate electrode located on the Hall bar surface (Fig 5.3(b)). The gate electrode charged negatively produces non equilibrium at one mesa edge. Otherwise the potential profile is flat over the complete mesa width if the gate is not polarized. The two different situations are visible at the lower part of the figure 5.3(c) which shows a zoom of the potential result at one of the mesa's edges. In the work of M.T. Woodside *et al.*, no comparison to transport measurement is reported.
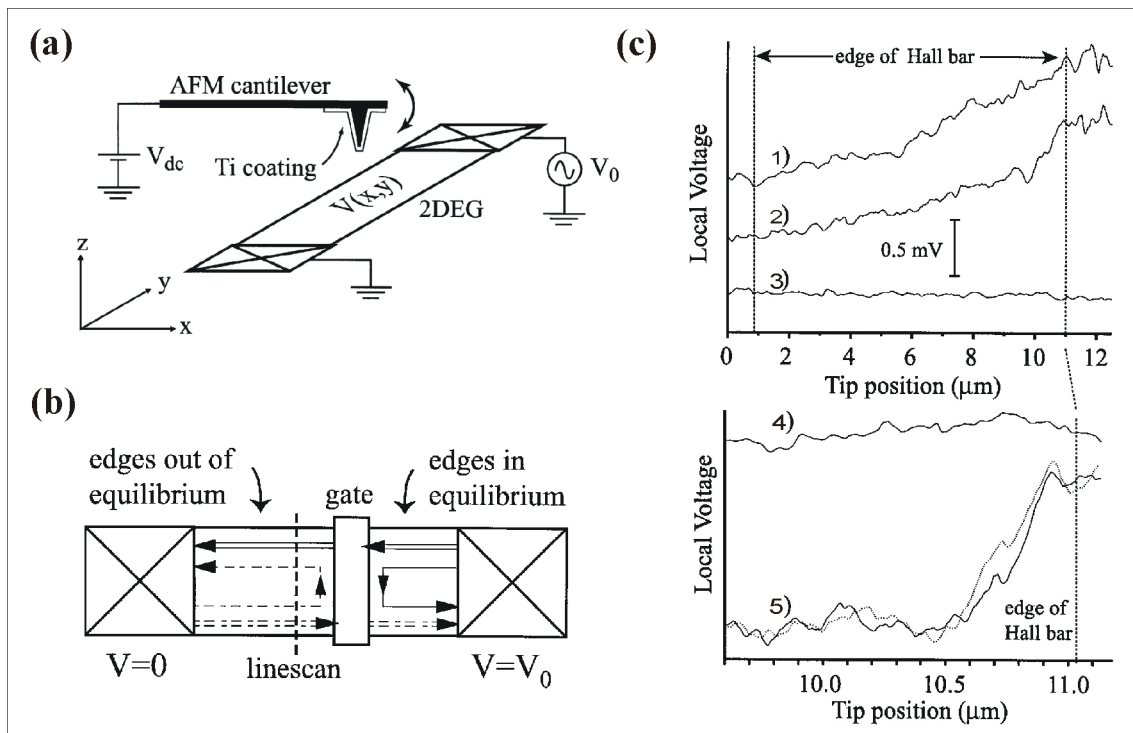

Figure 5.3.: **a)** Setup of the scanning force microscope to locally measure the Hall potential. **b)** Schematic of the gated mesa. Edge states picture showing the reflection of the innermost edge state. **c)** Results of the measured potential profiles with and without negative polarity applied to the gate electrode. Adapted from Woodside *et al.* [5].

5.1.3. Atypical Hall configuration

The voltage excitation is applied to the contact 2, and the contact 4 is grounded. In this configuration, the four-terminal resistance $R_{24,13}$ corresponds to an atypical Hall resistance which is asymmetric with respect to the magnetic field orientation (Fig 4.12). The potential distribution reproduces this asymmetry: the figure 5.4 shows that Hall potential is completely different at positive and at negative magnetic field. The positive case is similar to the distribution of the potential when the voltage excitation is applied between contacts 1 and 4 (Fig 5.2). In contrary, the negative case is similar to the configuration in which the voltage excitation is applied between contacts 2 and 3 (Fig 5.1).

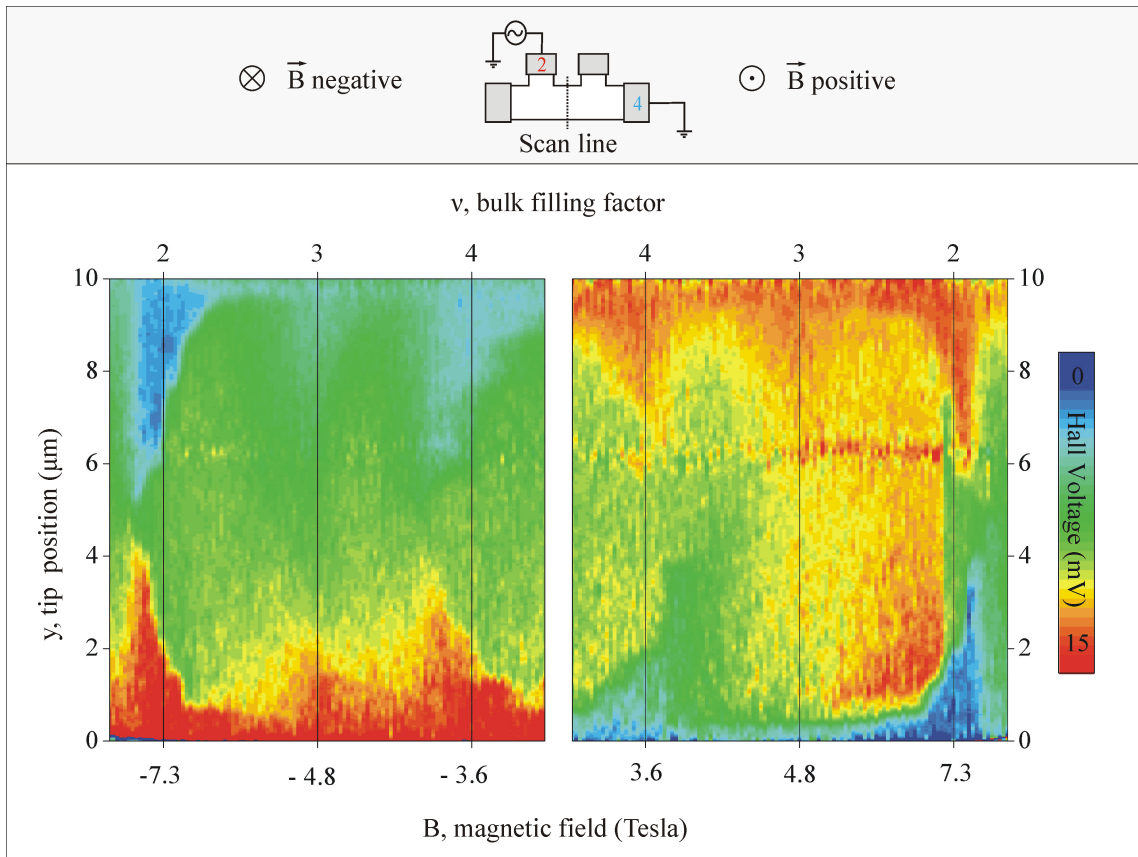Figure 5.4.: Potential probing in the atypical Hall configuration. The contacts 2 and 4 are used to applied the voltage excitation. Potential results at positive and negative magnetic field are different. For $B > 0$, the drops of the Hall potential in between $\nu = 2$ and $\nu = 3$ equally occur at the two Hall bar edges. For $B < 0$, a single drop is present at a distance around $y = 0.5 \, \mu\mathrm{m}$ of the lower border.

5.1.4. Non local configuration

The last studied configuration is the one related to the measurement of a non local resistance. In this configuration the excitation is applied at the left side of the Hall bar (contacts 1 and 2). As in the transport measurement of the section 4.13, the potential distribution is asymmetrical with respect to the magnetic field orientation. For positive magnetic field sign in which no local resistance was observed, the potential remains low (blue). At negative magnetic field, the potential shows a close coexistence of a high (red) and low (blue) potential value which is visible at the lower edge ($y \approx 1\,\mu$m). The measurement of a such distribution is a direct observation of local non equilibrium situation. At the upper mesa edge ($y = 10\,\mu$m), the potential has only a high value.
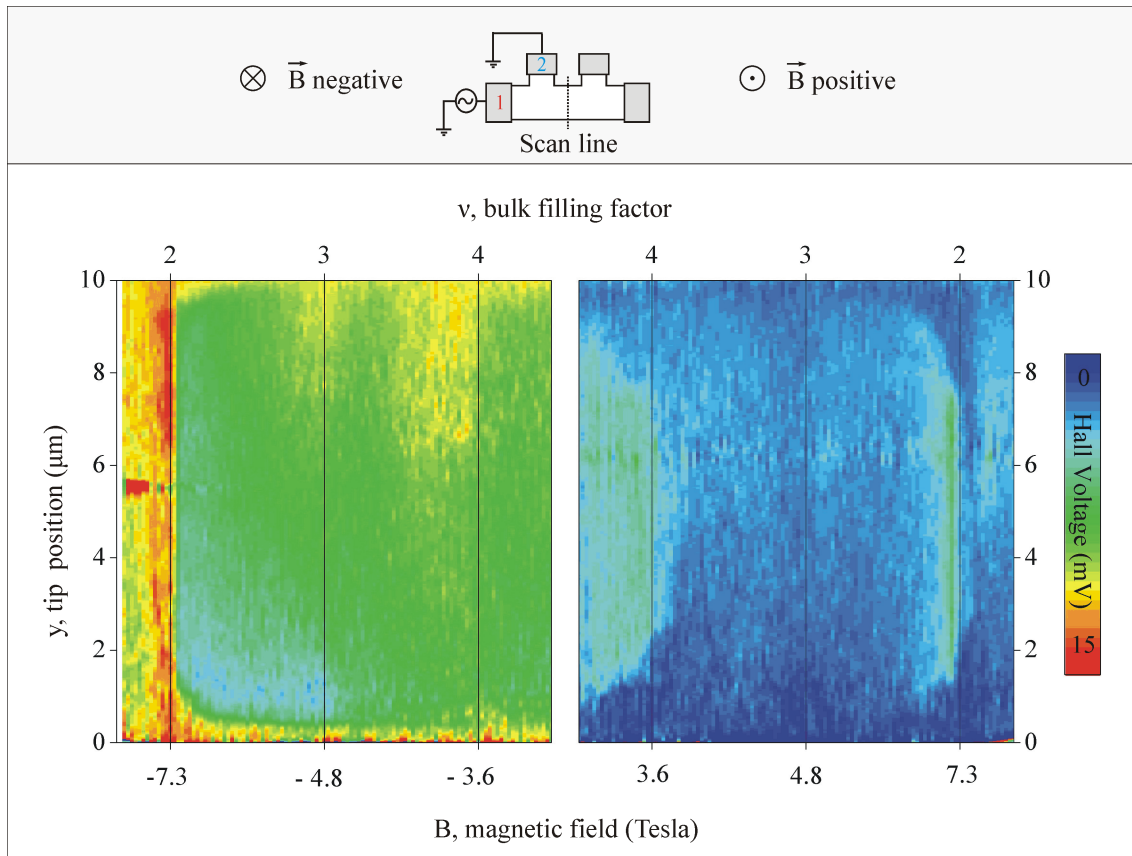
Figure 5.5.: Local potential measurement in a non local configuration with an excitation voltage in between the contacts 1 and 2. The potential profiles are absolutely different for the two signs of the magnetic field like in Fig. 5.4. The potential stays at low value (blue) for the positive magnetic field. At negative magnetic field in between $2 < \nu < 3$, a high potential (red) followed by a low potential (blue) is present at one edge. The other edge has a high potential.

5.2. Potential distribution in front of voltage probing contacts

Further potential measurements have been done close to the contact 4 in the atypical Hall configuration. We focus to the situation in which the voltage excitation is applied to the contact 1, and the contact 3 is grounded. The probing area has a rectangular shape of $10\,\mu\text{m} \times 3\,\mu\text{m}$. For safety reason, the scan is starting 200 nm away from the metallic contact. The figure 5.6 shows this $x - y$ potential mapping for a positive and a negative magnetic field corresponding to $\nu = 2.2$. The potential distribution for these two field orientations are different. At negative magnetic field, the potential has a high value (yellow/red) along the mesa border and the bulk has a low potential (blue). At positive field, this variation is less pronounced with a mean potential value which is lower. In both cases, the potential variation is located at mesa border. It is important to notice that such variation is present even along the line interface close to the contact.

In order to observe the different bulk potential with respect to the magnetic field value, the potential distribution is recorded for four positive magnetic fields corresponding to the bulk
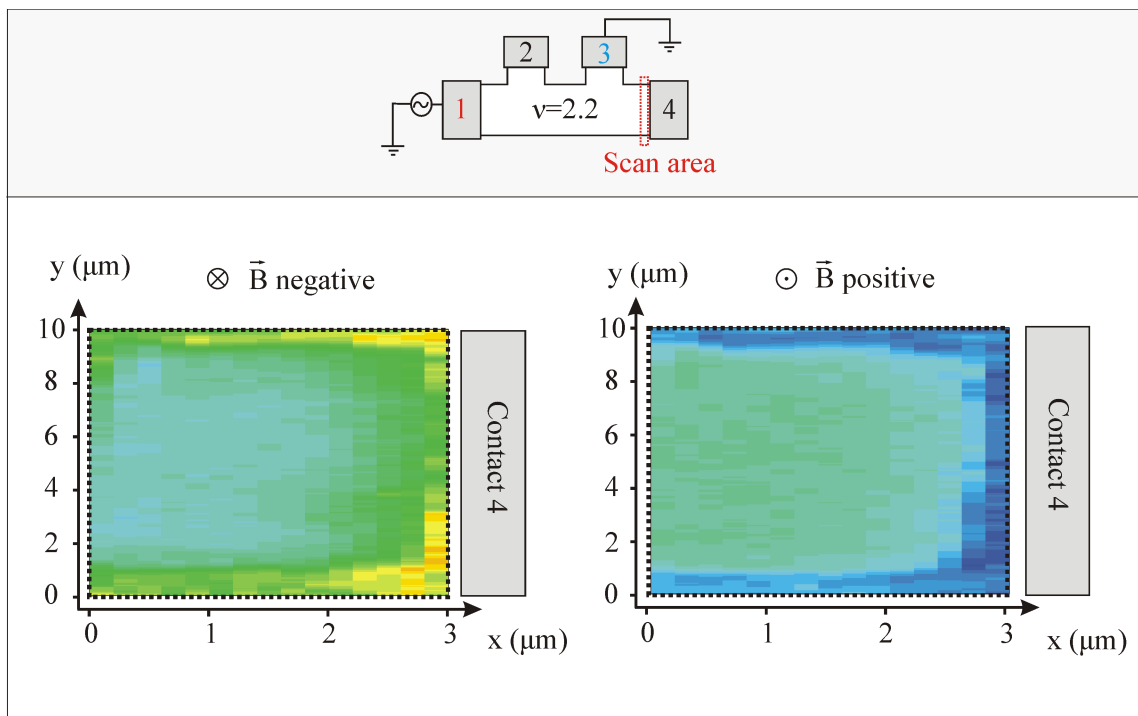
Figure 5.6.: $x - y$ potential profiles close to the contact 4 at $\nu = 2.2$ for a positive and a negative magnetic field. The electric setup has a similar configuration as the atypical Hall resistance measurement presented in the section 4.2.2.3.

filling factor $\nu = 2.2$, 2.1, 1.9 and 1.6 (Fig. 5.7). At $\nu = 2.2$, the bulk potential shows lower value which increases if the magnetic field is increased to $\nu = 2.1$. Then the potential at the scan area get a high value everywhere if $\nu = 1.9$ is attained. It starts to decrease at $\nu = 1.6$.

   This data obtained near the contact shows that the innermost incompressible strips (located by the drop of the potential) move to the bulk center region when the magnetic field is increased.
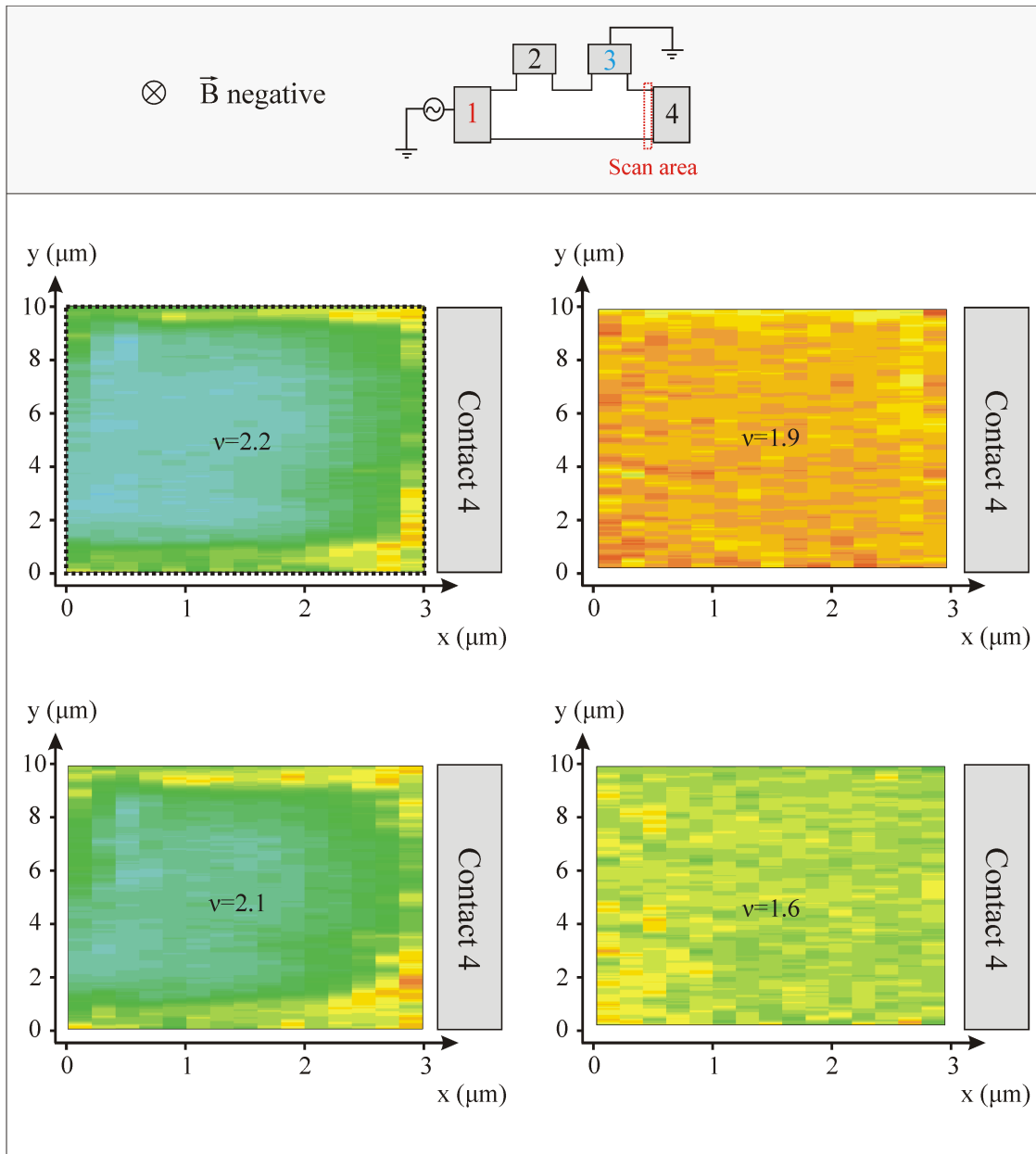
Figure 5.7.: $x - y$ mapping of the potential distribution in front of the contact 4 for a negative magnetic field at different bulk filling factor ν.

It is visible by looking at the main potential variation in the x-direction which is closer to the borderline of the contact at $\nu = 2.2$ than at $\nu = 2.1$. It is not possible to continuously follow the movement of the incompressible strips with the figure 5.7 since the figure only shows four different filling factors. Figure 5.8 replies to this problem by presenting the potential distribution along a trace at $1.5\,\mu\text{m}$ distance away from the contact as function of the magnetic field. Similar as in figure 5.7, we see how the potential value of the bulk mesa changes from low value at $\nu = 2.2$ or 2.1 to high value at $\nu = 1.9$. We can also observe that the transition from a situation with potential variation to a situation with flat potential distribution is very sharp and located around $\nu = 2$. At the scan line position corresponding to $x = 1.5\,\mu\text{m}$, on one hand, there is no potential drop - i.e. no incompressible strip, just below $\nu = 2$. On the other hand, potential drops are present at the two mesa'edges just above $\nu = 2$.

Figure 5.8.: Evolution of the potential profile with respect to the magnetic field. The line scan is recorded $1.5\,\mu\text{m}$ away from the borderline of the contact 4.

5.3. Potential profiles near the current sinking contact

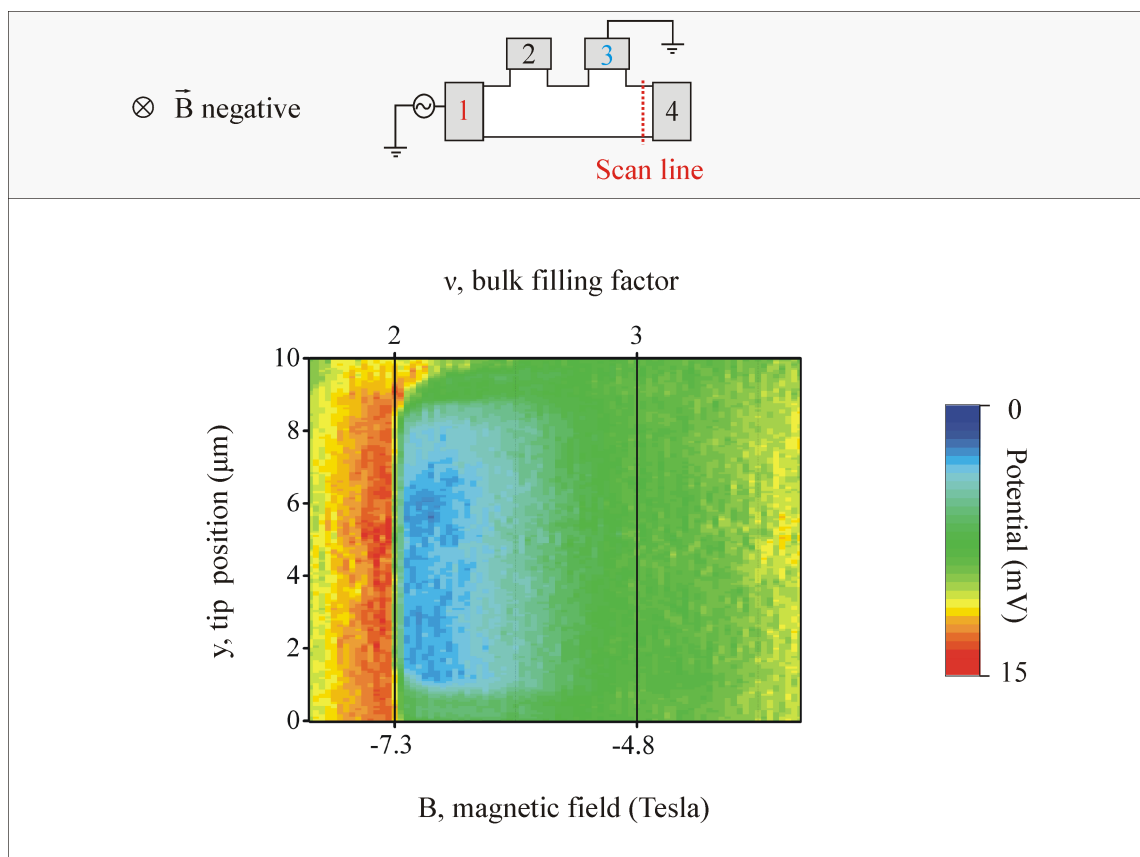Area close to the current injecting and sinking contacts has been studied in high magnetic field by different techniques such as Helium fountain effect [6] or cyclotron emission [7]. The results show strong local energy dissipation - named hot spot, which appears at one corner of these contacts (see figure 5.9). The location of the hot spot - either at the upper or lower contact corner, change with the magnetic field sign.
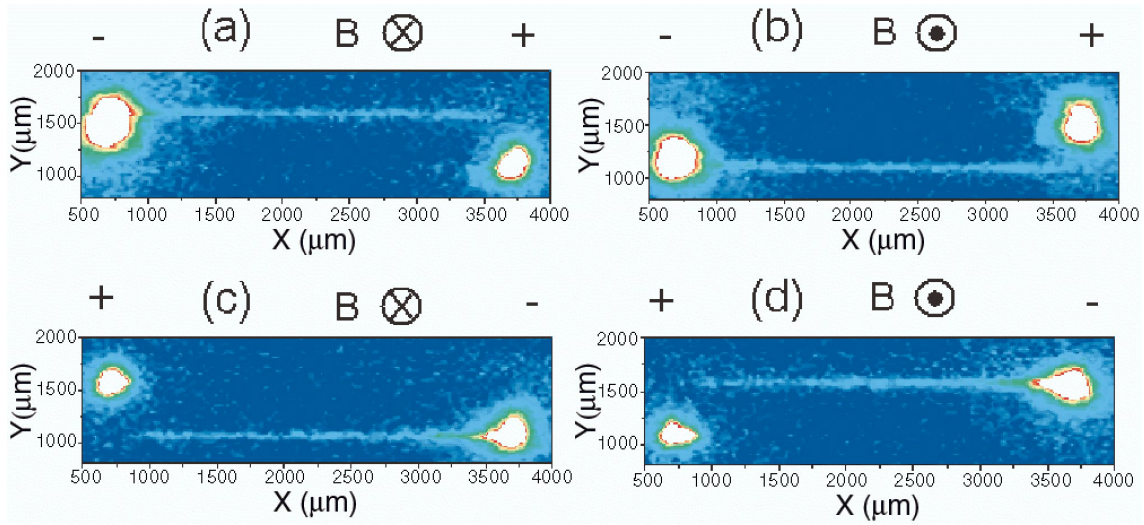
Figure 5.9.: Cyclotron emission measurements in the IQHE showing the position of the local dissipation in a macroscopic Hall bar (adapted from K. Ikushima *et al.* [7]). The four configurations correspond to different polarities and magnetic field orientations. Clear spots of dissipation are visible at opposite contact corners.

Hot spots positions are well understood from the calculation of the potential distribution under classical magnetic field. Potential inside the Drude model has its equipotential lines which converge to one contact corner (see J.H. Davies book [8]). Being expressed by the product $\vec{E} \cdot \vec{j}$ with $\vec{E}$ the local electric field and $\vec{j}$ the density of current, the dissipation is maximum and no zero at this corner.

With our cryogenic scanning force microscope, it is possible to investigate the equipotential convergence at such area and therefore to observe hot spots. The result of the potential distribution measurements in front of a current sinking contact is presented in figure 5.10. It corresponds to the configuration in which the contacts 1 is used to inject current and the contact 4 is connected to ground (as presented in figure 5.2, this configuration corresponds to a single drop inside the Hall potential profiles). The scan area is a rectangle of $10\,\mu$m times $3\,\mu$m located 200 nm near the contact 4. The bulk filling factor is $\nu = 2$.
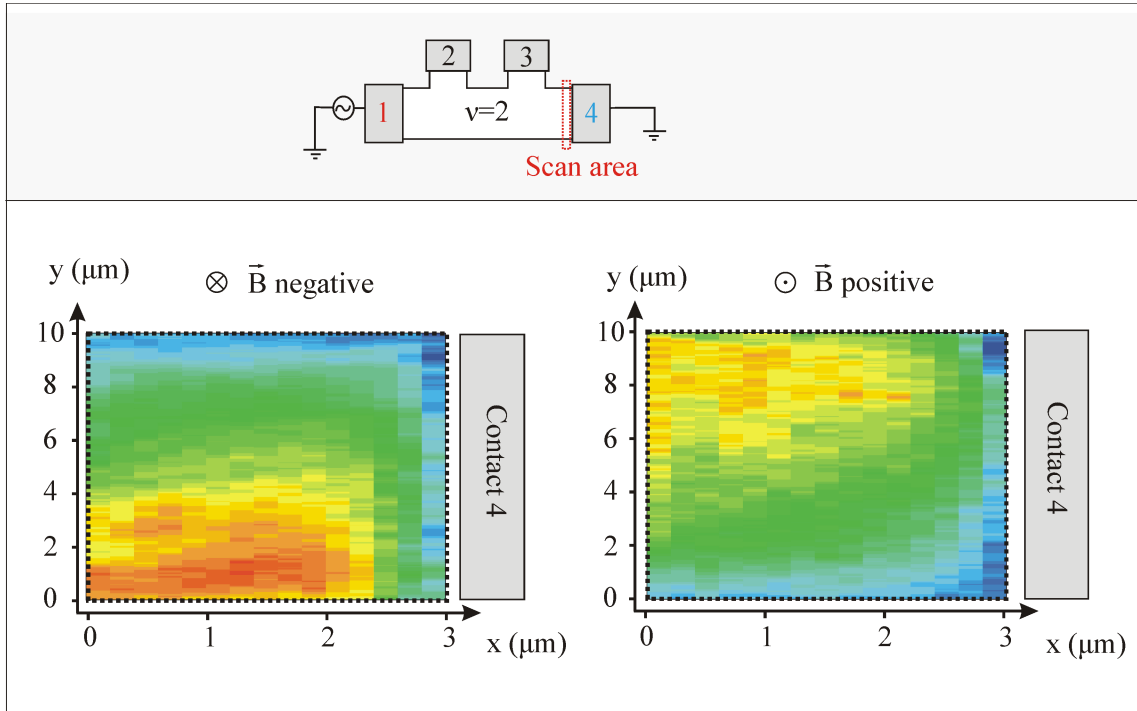
Figure 5.10.: Hall potential mapping near the grounding contact 4 at $\nu = 2$ for negative and positive magnetic field. The scanned area is a rectangle of $10\,\mu m$ times $3\,\mu m$. The equipotential line converge to the upper or lower contact corner depending on the magnetic field orientation.

At negative magnetic field and away from the contact 4 (defined in Fig 5.10 as $x \approx 0\,\mu$m), the potential has a low (blue) value at the upper edge ($y \approx 10\,\mu$m) and a high (red) value at the lower edge ($y \approx 0\,\mu$m). Coming closer to the contact 4 ($x \approx 3\,\mu$m), the equipotential lines (same color) converge to the lower corner and the interface line between the contact and the 2DES owns a low potential as it should be from the boundary conditions (we remind that the contact 4 is at ground potential). For positive magnetic field, the situation is opposite (see Appendix C): the equipotential lines converge to the upper corner. These results demonstrate that the dissipation occurs in the 2DES and not inside the metallic contact.

The figure 5.11 present similar results for four different values of negative magnetic field. The gradient of potential (contrast of color) is maximum at integer filling factors. Therefore dissipation is maximum in the quantum Hall regime.
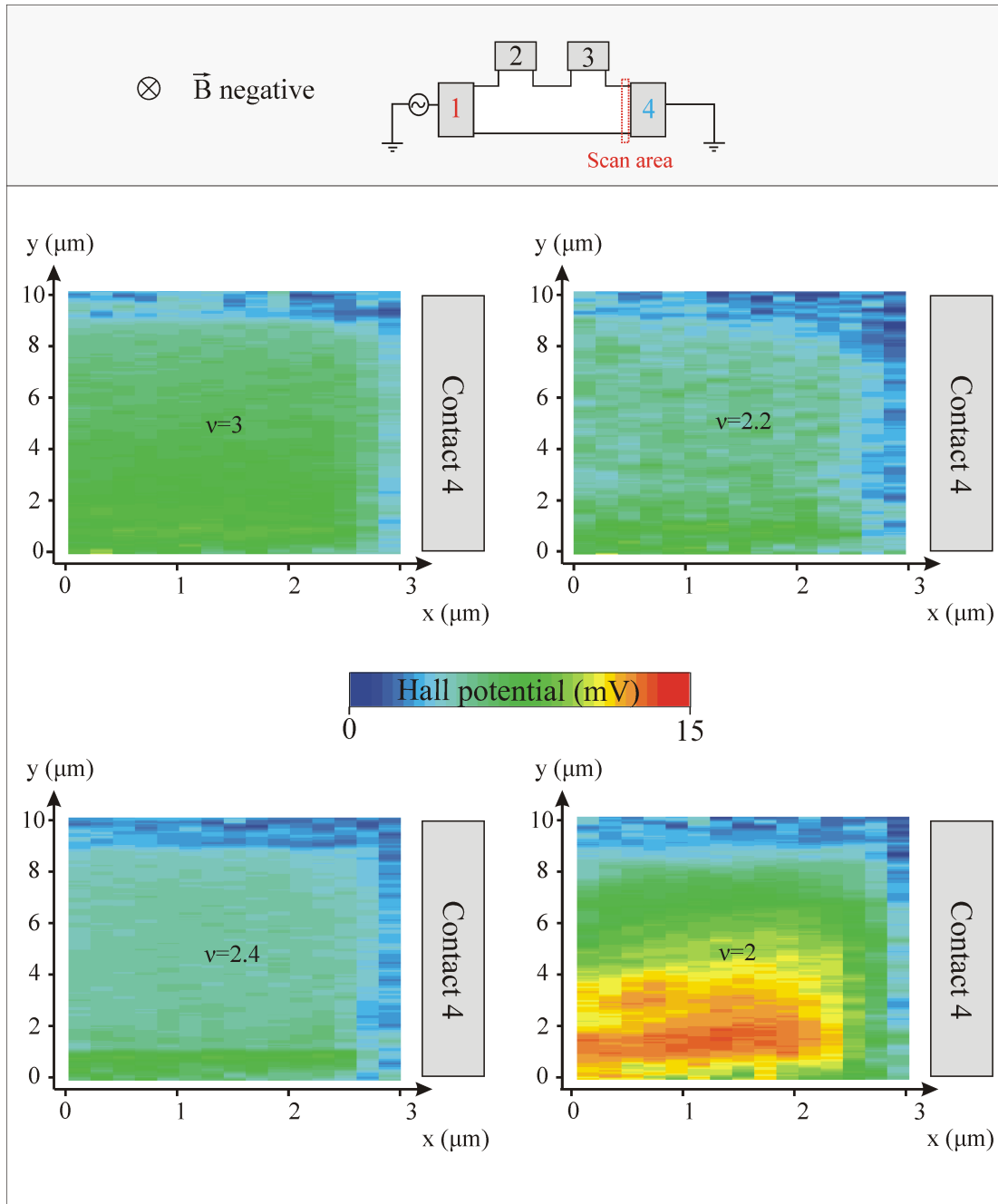
Figure 5.11.: Evolution of the potential distribution near the grounded contact 4 with negative magnetic field.

Bibliography

[1] P. Weitz, Untersuchungen zum Verlauf der Hall-Spannung in einem zweidimensionalen Elektronensystem unter den Bedingung des Quanten-Hall-Effekts mittels eines Raster-Kraft-Mikroskops, PhD thesis, Max-Planck-Institut für Festkörperforschung / University of Hamburg (1999).

[2] E. Ahlswede, Potential- und Stromverteilung beim Quantum-Hall-Effekt bestimmt mittels Ratserkraftmikroskopie, PhD thesis, Max-Planck-Institut für Festkörperforschung / University of Stuttgart (2002).

[3] E. Ahlswede, P. Weitz, J. Weis, K. Klitzing, and K. Eberl, Physica B **298**, 562 (2001).

[4] A. Siddiki, Model calculation of current and density distributions in dissipative Hall bar, PhD thesis, Max-Planck-Institut für Festkörperforschung / University of Würzburg (2005).

[5] K. McCormick, M. Woodside, M. Huang, M. Wu, P. McEuen, C. Duruoz, and J. Harris, Phys. Rev. B **59**, 4654 (1999).

[6] U. Klass, W. Dietsche, K. von Klitzing, and K. Ploog, Journal Zeitschrift für Physik B Condensed Matter **82**, 351 (1991).

[7] K. Ikushima, H. Sakuma, S. Komiyama, , and K. Hirakawa, Phys. Rev. Lett. **93**, 146804 (2004).

[8] J. Davies, *The physics of low dimensional semiconductors* (Cambridge University Press, Cambridge, 1998), Chap. 9.

6. The adiabatic regime described in terms of compressible and incompressible strips

The adiabatic regime is usually described within the single particle edge state picture. However, previous measurements of the potential landscape in the quantum Hall regime [1] enforce us to use the picture of compressible and incompressible strips (denoted as CSs and ISs). We know that in front of an ohmic contact an electron depletion occurs - with the consequence that CSs and ISs are even running in parallel to the interface between alloyed metal and 2DES [2]. This should be the base to explain our data in this chapter. Nevertheless it turns out that it is not enough: different insulating properties for the incompressible strips depending on the orientation of the metal/2DES interface line relatively to the crystal orientation of the heterostructure have to be assumed to explain our full set of data.

The chapter is organized in the following way: first, our qualitative model is described via the configuration in which the current carrying contacts are 1 and 4 (the borderline with the 2DES is oriented perpendicular to the [01-1] crystal direction). This configuration will prove that the innermost incompressible strip is decoupled from these contacts. The non local resistance configuration is then illustrated. It shows how the ISs are equilibrated either in contact 2 or in contact 3. These two configurations clearly justify the assumption about the anisotropic insulating behavior of incompressible strips in front of contact oriented in different crystal orientations. The model depicted for the atypical Hall configuration in which the current is injected by the contacts 1 and 3, explains the asymmetry of this resistance with respect to the magnetic field sign and the existence of large plateaus. The last configuration -contacts 2 and 3 as injecting contacts, is included for completeness. Further situations are presented which also stress the powerful predictability of the model.

Contents

6.1. Elaboration of a qualitative model

6.1.1. Anisotropy in the insulating properties of incompressible strips along the contact borderline

Potential profiles obtained in the configuration with current injecting contacts 1 and 4 (section 5.1.2) is used for elaborating a qualitative model of the adiabatic transport. At $\nu = 3$, this model splits the 2DES in three compressible and incompressible strips at each mesa edges. As observed by E. Ahlswede (Fig. 1.8) and by myself (Fig. 5.6), these strips follow the shape of the Hall bar by running along ohmic contacts and mesa edges (section 1.9). To fit with our measurements, the innermost incompressible strip has to produce a decoupling of the outermost compressible strip in front of contacts 1 and 4, and it should let in balance the compressible strips in front of the contacts 2 and 3.

   Two situations are depicted and compared in figure 6.1 in order to justify such an anisotropy. In the first situation - named "coupling without anisotropy" (Fig. 6.1 (a) to (d)), the innermost incompressible strip owns the same thickness in front of all contacts. This strip is thin enough to perform a good coupling between different compressible strips. In the second situation ("decoupling with anisotropy", Fig 6.1 (e) to (h)), the innermost incompressible strip is represented with a thin thickness in front of contacts 2 and 3, and a large one in front of contacts 1 and 4. The large thickness is at the origin of a perfect decoupling between compressible regions. Difference of strips thickness is due to the assumption of different electron density profiles [i]: either the density profile is assumed to be smooth if the interface line to the contact is perpendicular to the [01-1] heterostructure crystal direction (contacts 1 and 4), or it is sharp for the [011] direction (contacts 2 and 3).

   The anisotropy in the electron density was already expected at zero magnetic field from the measurement of the contact resistances: higher resistance was found in the [01-1] heterostructure direction than in [011] direction (see section 4.1.3). In addition, the two-terminal magnetotransport measurements in high magnetic field displayed similar anisotropy: the Hall plateau of the two terminal resistance is expended to lower magnetic field if at least one of the contacts 1 or 4 is used to inject or to sink the applied current (see section 4.2.3). It is not the case if only the contacts 2 and 3 with a borderline perpendicular to the [011] direction of the heterostructure are used.

---

[i] The relation between thickness and density variation is expressed via the equation 1.27.

In figure 6.1 (a) and (e), the 2DES is depicted in the equilibrium situation. All the strips have the same electrochemical potentials (symbolized by a gray color). A difference of DC voltage [ii] is applied between the contacts 1 and 4 which produces a current flow through the Hall bar. The new distribution of the electrochemical potential μ_{elch} and the related potential landscape under non equilibrium situation is shown in figure 6.1 (a) to (d) and (e) to (h) via different levels of color: blue for low μ_{elch}, red for high μ_{elch} and orange (red+red+blue) or green (red+blue) for intermediate μ_{elch}. The time evolution of the electrochemical potential is the following. In front of the contacts 1 and 4 (Fig. 6.1 (b) and (f)), the two innermost compressible strips adjust first their electrochemical potential with respect to the attached contacts: high μ_{elch} strips (red) in front of contact 1 and low μ_{elch} strips (blue) close to the contact 2.   These two CSs get the same electrochemical potential since the insulator-like outermost IS is too thin to perform a significant decoupling (even if its insulating behavior is negligible, this IS is shown in the figures to point out the value of the filling factor). In Fig. 6.1(f), the innermost CS is isolated (gray color) due to the large thickness of the innermost IS in front of the contacts 1 and 4. It is not the case in figure 6.1(b). Under current flow, the evolution of the electrochemical potential into the sample depends on the magnetic field sign which assigns the direction of the skipping orbit. With a negative B as chosen in figure 6.1, the electrochemical potential of the compressible strips is propagated in anti-clockwise direction. The high μ_{elch} of the CSs connected to the contact 1 and the low μ_{elch} of the CSs linked to the contact 2 are transmitted in the direction of the contact 3 (Fig. 6.1(c) and (g)). In the case of "anisotropy", the inner and outer CSs keep their own electrochemical potential close to the contacts 1 and 4 since a large incompressible strip isolates them. The lack of scattering in high mobility sample allows also to keep this different of electrochemical potential along the complete mesa length. It follows that a strong and local non equilibrium persist along the complete Hall Bar (adiabatic regime). Such non equilibrium was probed by scanning force microscopy as shown in the previous chapter 5 or in Fig. 6.2. Under high magnetic field, the distortion of the electric field at the opposite corners of the current injecting and sinking contacts induces some hot spots (yellow quarters of

---

[ii] In the transport measurements, a net current was driven whereas in the potential probing an AC voltage was applied. Henceforth a DC voltage is used to draw the model. This difference is not relevant and the configurations are considered as equivalent.

Figure 6.1.: Model showing the time evolution of the electrochemical potential distribution at $\nu = 3$. The voltage difference in the four-terminal Hall bar is applied between contacts 1 and 4. **a-d)** The innermost incompressible strip has the same little thickness in front of all the contacts. Equilibration of the electrochemical potentials occurs. **e-h)** The thickness of the innermost incompressible strip is thinner close to contacts 2 and 3. With a larger thickness close to the contacts 1 and 4, the innermost IS stay decoupled from these contacts.

circle in the figures 6.1(d)-(e)) corresponding to spot of energy dissipation (section 5.3). This dissipation obviously does not modify the decoupling of the innermost IS in front of contacts
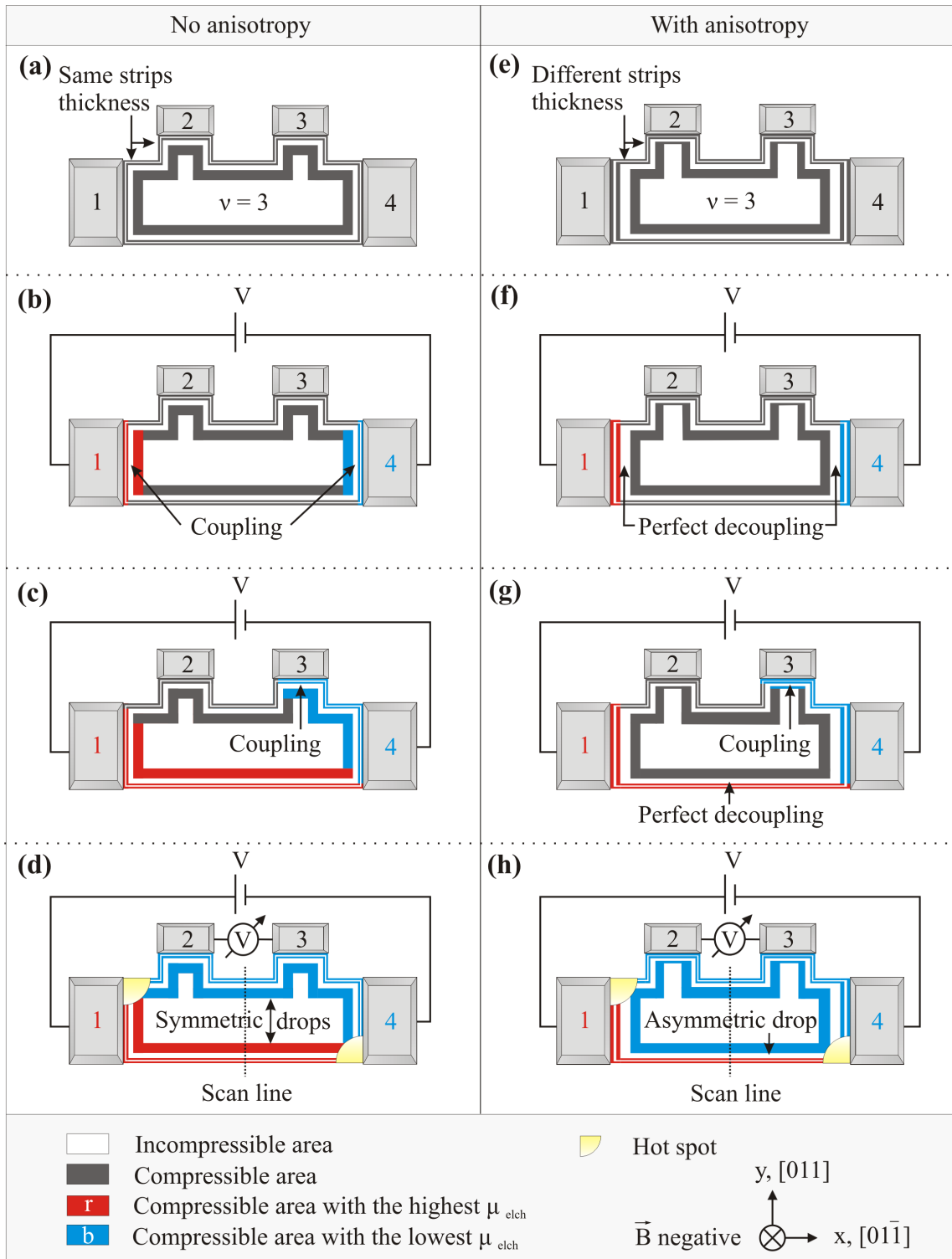
1 and 4. Finally, two distinguishable profiles appear (Fig. 6.1(d) and (h)). Only the case (h) with the anisotropy reproduces the large potential drop measured at one mesa edge. The case (d) predicts unobserved drops of the Hall potential equally distributed at the two edges of the Hall bar.

The model in similar configuration as Fig. 6.1 is displayed for negative and for positive magnetic fields in Fig. 6.2. The measured potential profile at $\nu = 3$ is also shown in order to compare it to the model. A clear similarity is visible between the distribution of electrochemical potential given by the model and the measured Hall potential (the scanning line is oriented in the width direction of the mesa and located between the contacts 2 and 3). At negative (positive) magnetic field, the model exhibits between the contacts 2 and 3 a large single drop (rise) in the Hall potential located exclusively at the edge of the mesa owing no voltage probing contacts. It is in agreement with the measured potential profile shown at the bottom of the figure 6.2. Such
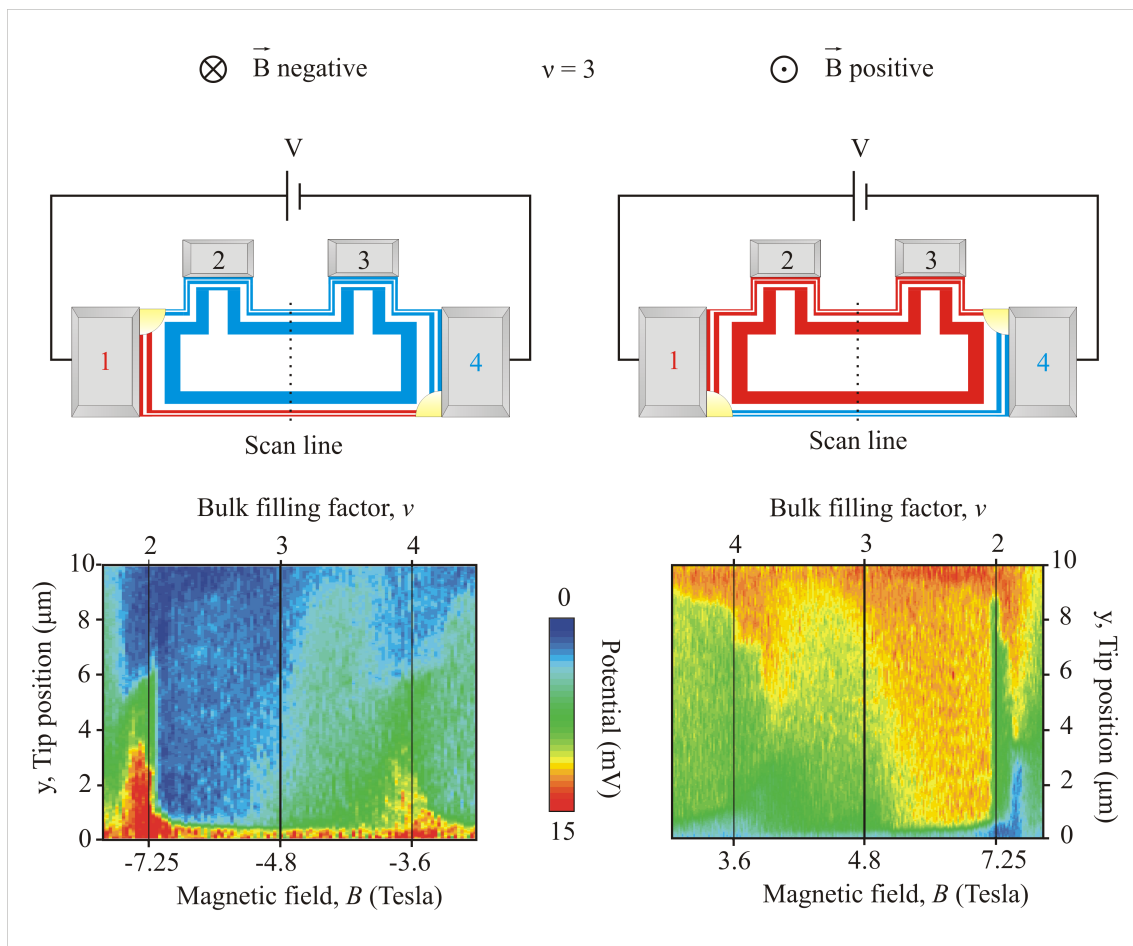

Figure 6.2.: Comparison between model and potential measurements in the setup with current injected in [01-1] direction (contacts 1 and 4).

distribution of potential only happens if the innermost compressible strip is decoupled from the contact 1 (4) in negative (positive) magnetic field. Such decoupling has to be include at both contacts 1 and 4.

6.1.2. Model in the non local resistance configuration

Compared to the previous section, the model is now elaborated in the non local resistance configuration - i.e. the voltage excitation is applied between the contacts 1 and 2. The situations without and with anisotropy of the strip thickness are presented in figure 6.3 at negative negative magnetic field ($\nu = 3$). In the first situation (Fig. 6.3(a) to (d)), the CSs close to the contacts 1, 2, 3 and 4 are coupled whereas the innermost CS in front of the contact 1 and 4 stays decoupled in the second situation (Fig. 6.3(e) to (h)). Different electrochemical potential distributions follow as shown in Fig. 6.3(d) and (h):

- Without anisotropy, the contacts 3 and 4 have the same electrochemical potential (red) and no potential drop is predicted on the right side of the Hall bar. In consequence, no resistance $R_{12,34}$ is expected. This prediction is in contradiction with the measured Hall potential profiles which show potential drops (see data in Fig. 6.4) and with the transport measurements which give a no local resistance (see section 4.2.2.4).

- With anisotropy, the model depicted a change at the scan line position from high to low μ_{elch} and again to high μ_{elch}. This landscape is precisely the result obtained with the scanning force measurements (see Fig. 6.4).

The model in non local resistance configuration reinforces our anisotropic assumption since only the anisotropic case (d) properly describes the measurements. In addition, the model and the Hall potential measurements agree for positive and for negative magnetic field (Fig. 6.4). The non local configuration shows also that equilibration has to be included in front of the contact 3 (or in front of the contact 2 if the voltage excitation is applied between the contacts 3 and 4). Energy dissipation - like hot spot, is expected near such contact where low and high electrochemical potential are equilibrated (transition to orange color in figure 6.4).

Some comments concerning the origin of non local resistance can be done from the model: at negative magnetic field, $R_{12,34}$ is non zero since a gradient of electrochemical potential between the contacts 1 and 2 gives different potential at the contacts 3 and 4 (labeled respectively by orange and red colors). This resistance is called "non local" in the way that the contact 3 probes the outermost compressible strip which has an electrochemical potential value determined by the insulating properties of the innermost incompressible strip located far away in front of the contact 1. The voltage probed at one side of the Hall bar drastically depends on the more or less good equilibration occurring at the other side. The voltage measurement extracts global behavior and the definition of a local resistivity becomes not adequate.
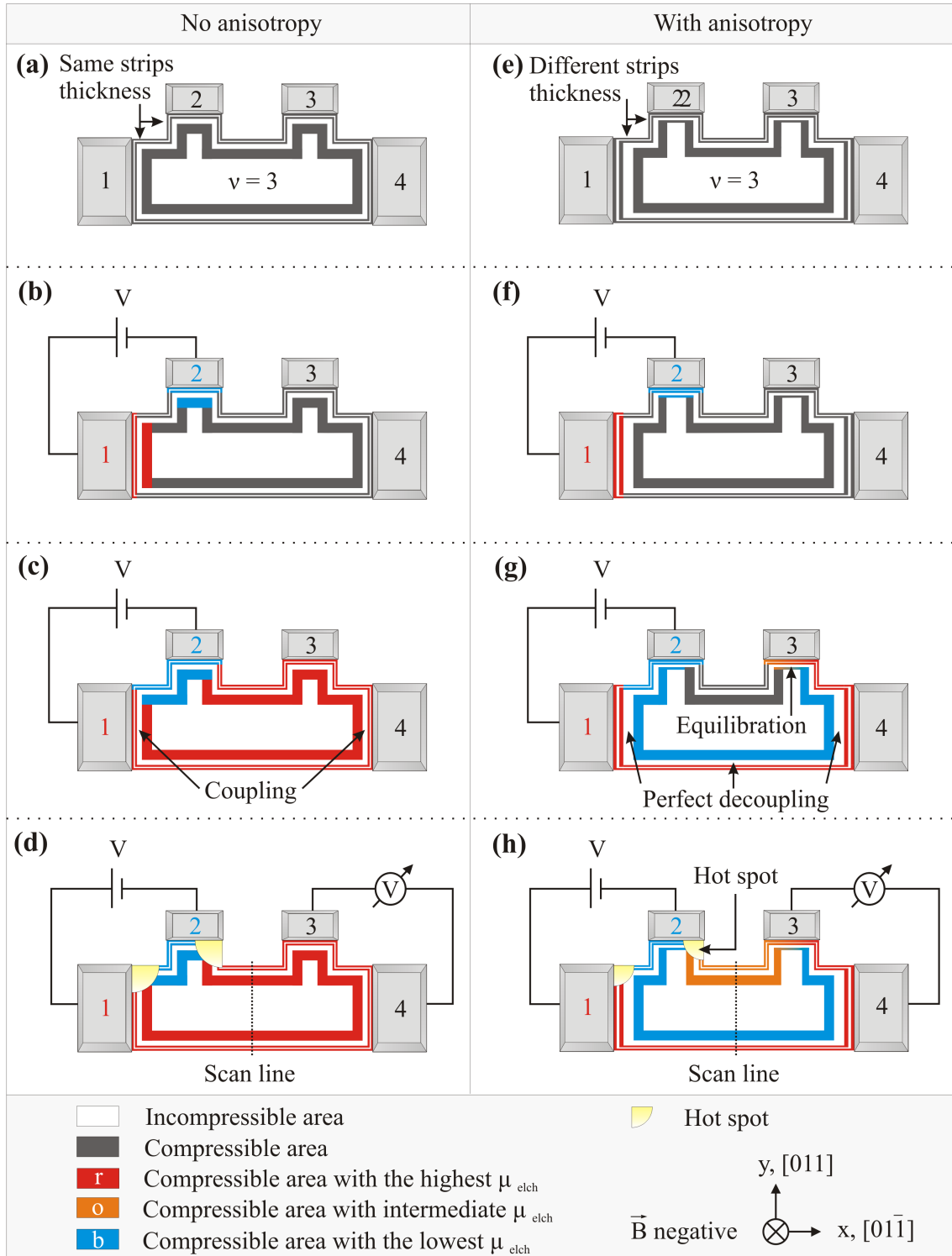
Figure 6.3.: Model at $\nu = 3$ in the case of the non local setup. Situation without (a-d) and with (e-h) strip thickness anisotropy are illustrated. **a/e)** Equilibrium situation. **b/f)** Voltage applied to contacts 1 and 2. The connected compressible strips follow the electrochemical potential of these contacts. **c/g)** Propagation of the electrochemical potential along the edges into the sample. The direction is given by the magnetic field sign. **d/h)** Final potential distribution.
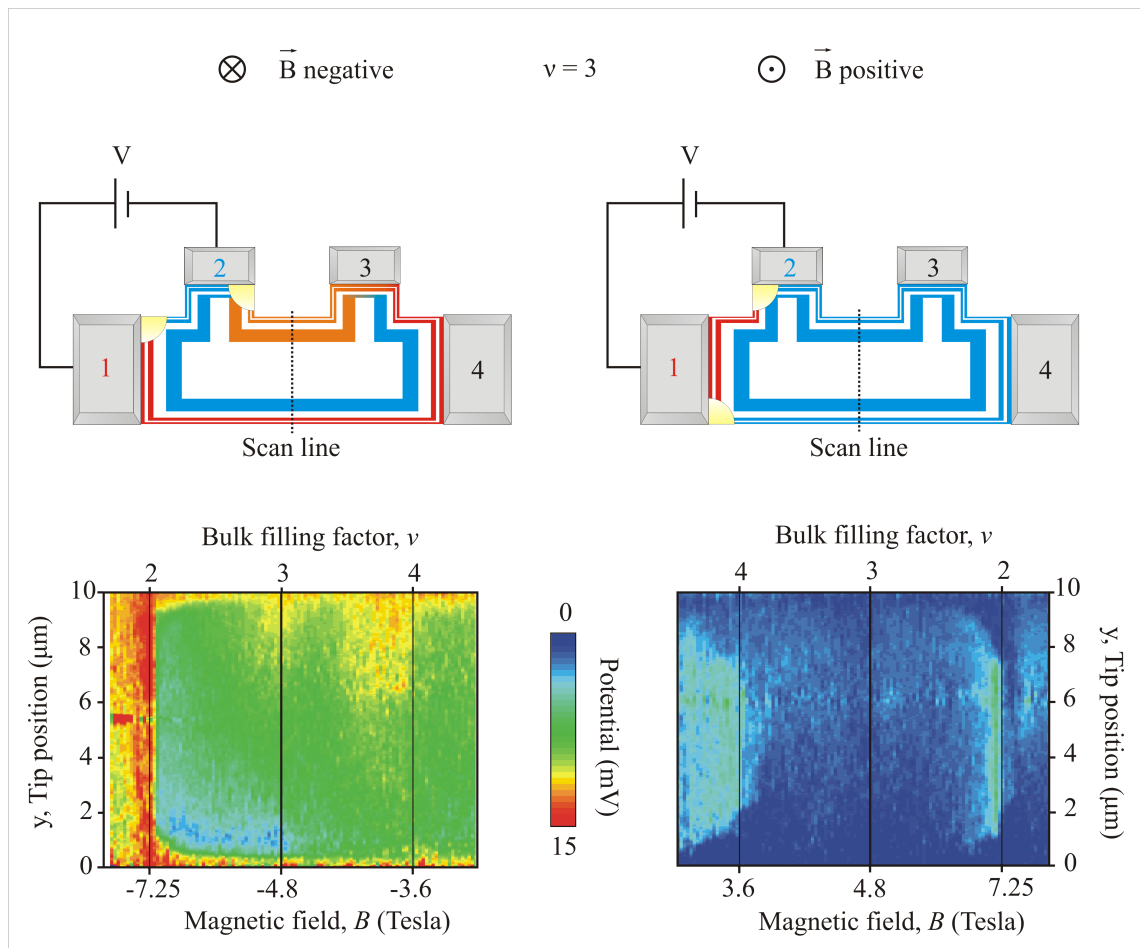
Figure 6.4.: Comparison between model and potential measurements in the non local configuration. In front of contact 3 at negative magnetic field, equilibration and dissipation occur.

Concerning the current path for negative B, the potential drop is different in one mesa edge compared to the other edge. It follows a net non equilibrium current flowing on the mesa side where the contacts 3 and 4 are located. It is surprising since the classical current path occurring at zero magnetic field would show no net current in this area. In positive magnetic field, the situation is easier: the two potential probing contacts feel the same electrochemical potential and the voltage drops between contacts 3 and 4 is therefore null. The electrochemical potential is the same everywhere in this part of the Hall bar and out of equilibrium current is not present.

6.1.3. Model for the atypical Hall configuration

The model is now developed with a high electrochemical potential at the contact 2 and a low electrochemical potential applied to the contact 4. The situation is equivalent to the atypical
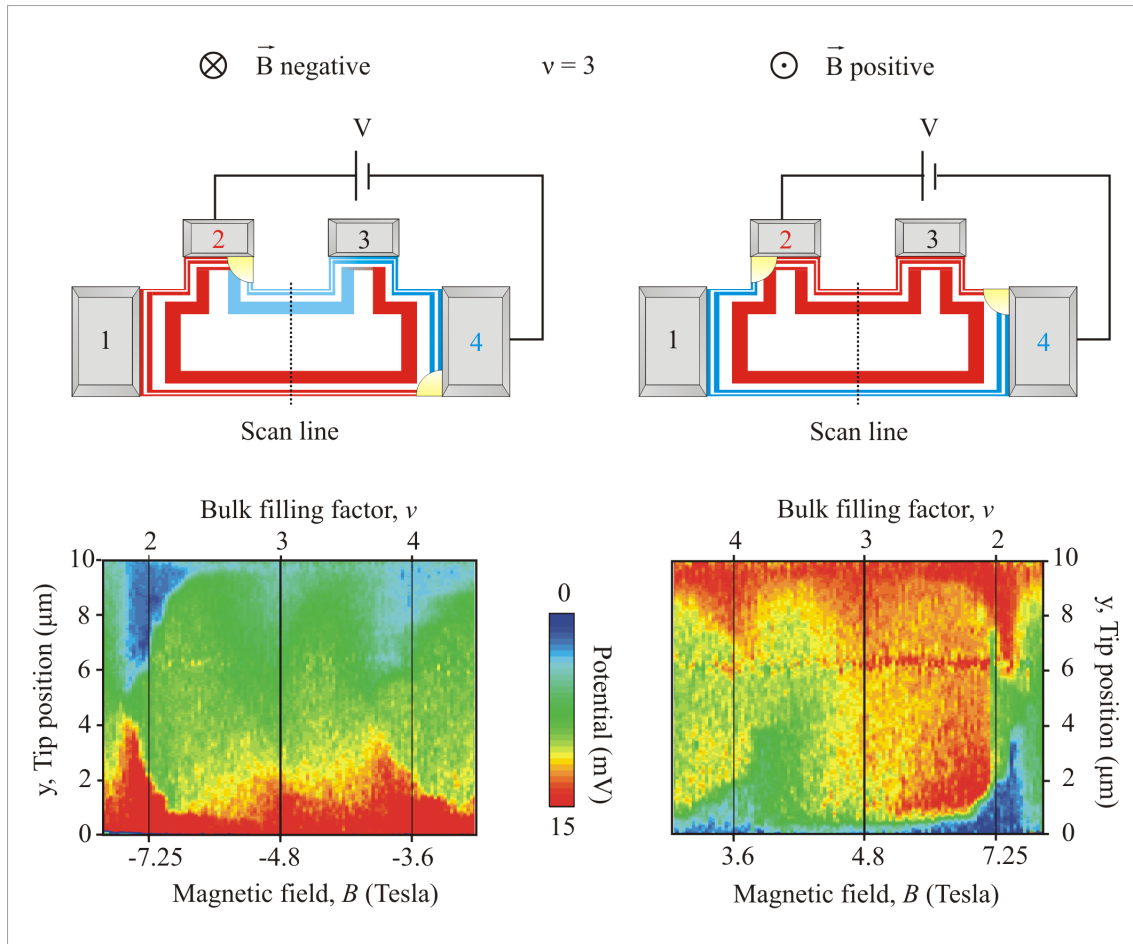

Figure 6.5.: Comparison between model and potential measurements in the atypical Hall configuration.

Hall transport configuration shown in section 4.2.2.3 (the current carrying contacts are just different). Thin incompressible strips in front of the contact 3 allows the equilibration of all the compressible strips present in this contact arm. The results give different potential distribution in negative and in positive magnetic field as it is measured in the Hall potential measurements (Fig. 6.5). In negative magnetic field, the expected Hall resistance is recovered since the equilibration between edge and bulk (or innermost compressible strip) occurs in front of the voltage probing contact 3. In positive magnetic field at $\nu = 3$, only the incompressible strip corresponding to the local filling factor $\nu = 2$ located at the bottom edge carries current. The voltage probe 1 measures low potential and the voltage probe 3 measures a high potential. This unbalanced situation will stay until $\nu = 2$. It follows that the atypical Hall resistance $R_{24,13}$ is constant on the complete magnetic field range between $\nu = 3$ and $\nu = 2$ as it was measured via the observation of a large plateau in the magneto-transport of the atypical Hall resistance $R_{24,13}$ (see section 4.2.2.3).

In an atypical Hall configuration, potential profile was measured close to the voltage probing contact 4. The result can be compared to the model. The figure 6.6 shows the results at filling factor $\nu = 2$ and at $\nu = 2.2$. The SFM scans an area of $3\ \mu$m large over the $10\ \mu$m mesa width [iii]. The similarity between the model and the potential measurement confirms the existence of a strong decoupling between bulk and edge in front of this contact. At $\nu = 2.2$, the measurement attests that the voltage probing contact is linked to a high potential (red) at the edges whereas the bulk has a lower potential (blue). In between these two regions, a large area (around $1\ \mu$m thick) shows a gradient of potential - i.e. a large incompressible strip. At $\nu = 2$, the potential profile has a high potential (red) everywhere in the contact arm because the region with lower potential is moved much more inside the center of the Hall bar (see section 1.9).

[iii] To protect the tip from possible collisions, a safety distance of 0.2 μm is maintained between tip and contact.
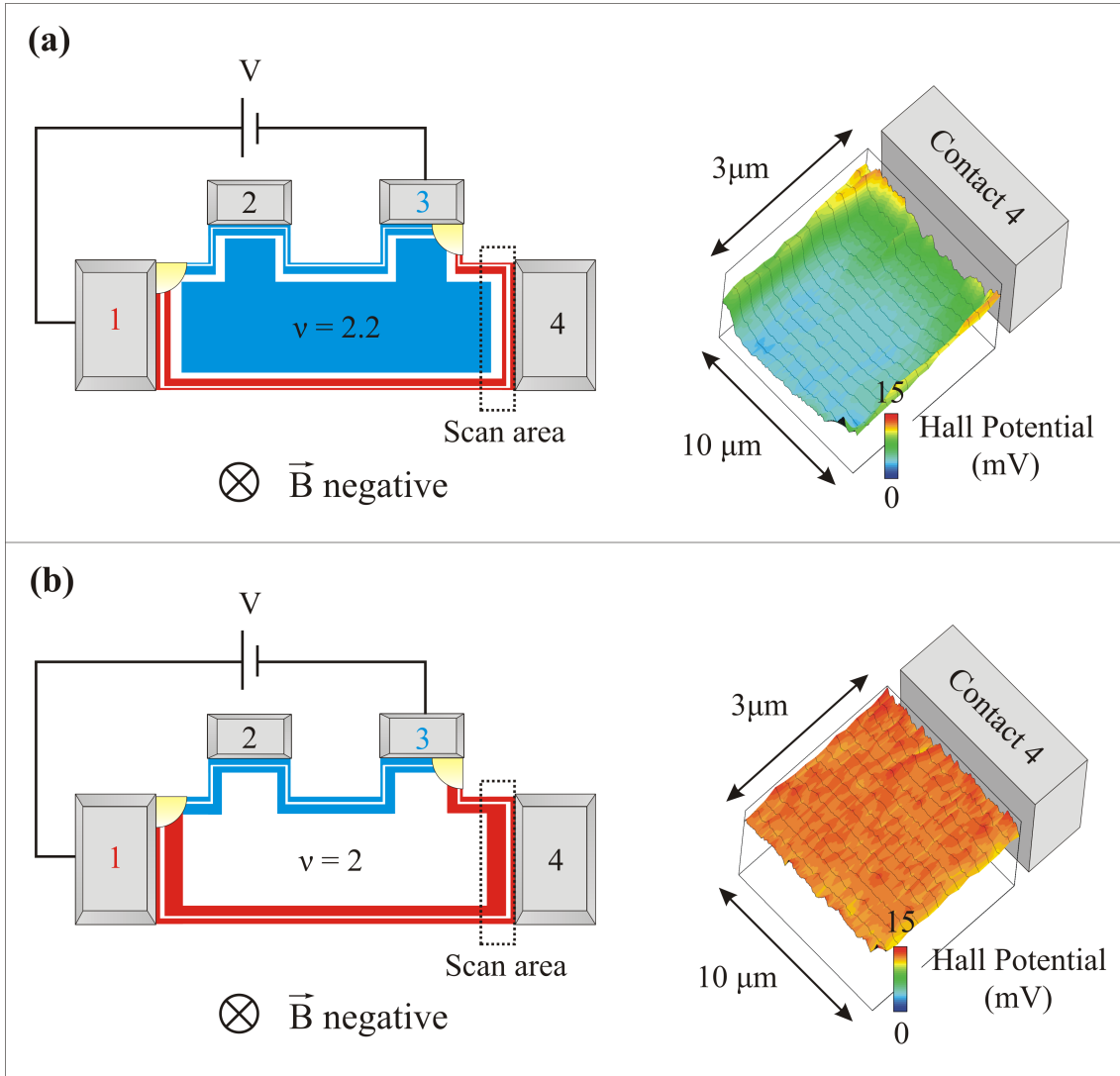
Figure 6.6.: Comparison between model predictions and probed potential in front of the voltage probing contact 4 in the case of the atypical Hall setup. **a)** At $\nu = 2.2$, the bulk is compressible with low μ_{elch} (blue) and decoupled from the contacts 1 and 4 by a large incompressible strip. Such situation is measured by scanning force microscopy: Hall potential stays at high magnitude in front of the contact 4 and along the edges, whereas the area more inside the mesa has lower potential. **b)** At $\nu = 2$, the bulk is incompressible (white) and the strips with high μ_{elch} moves in direction of the mesa center. Only the high potential is present and probed close to the contact 4.

6.1.4. Model for current injecting contacts 2 and 3

For completeness, the figure 6.7 presents the model prediction at $\nu = 3$ when contacts 2 and 3 own a difference of electrochemical potential. The borderline of these contacts is oriented perpendicularly to the [011] direction of the heterostructure, in consequence the present configuration is not sensitive to the decoupling of the innermost incompressible strip in front of the contact 1 and 4. As observed with the scanning force measurements in our high mobility sample, the model predicts on one edge of the Hall bar a high potential (red) defined by the elec-
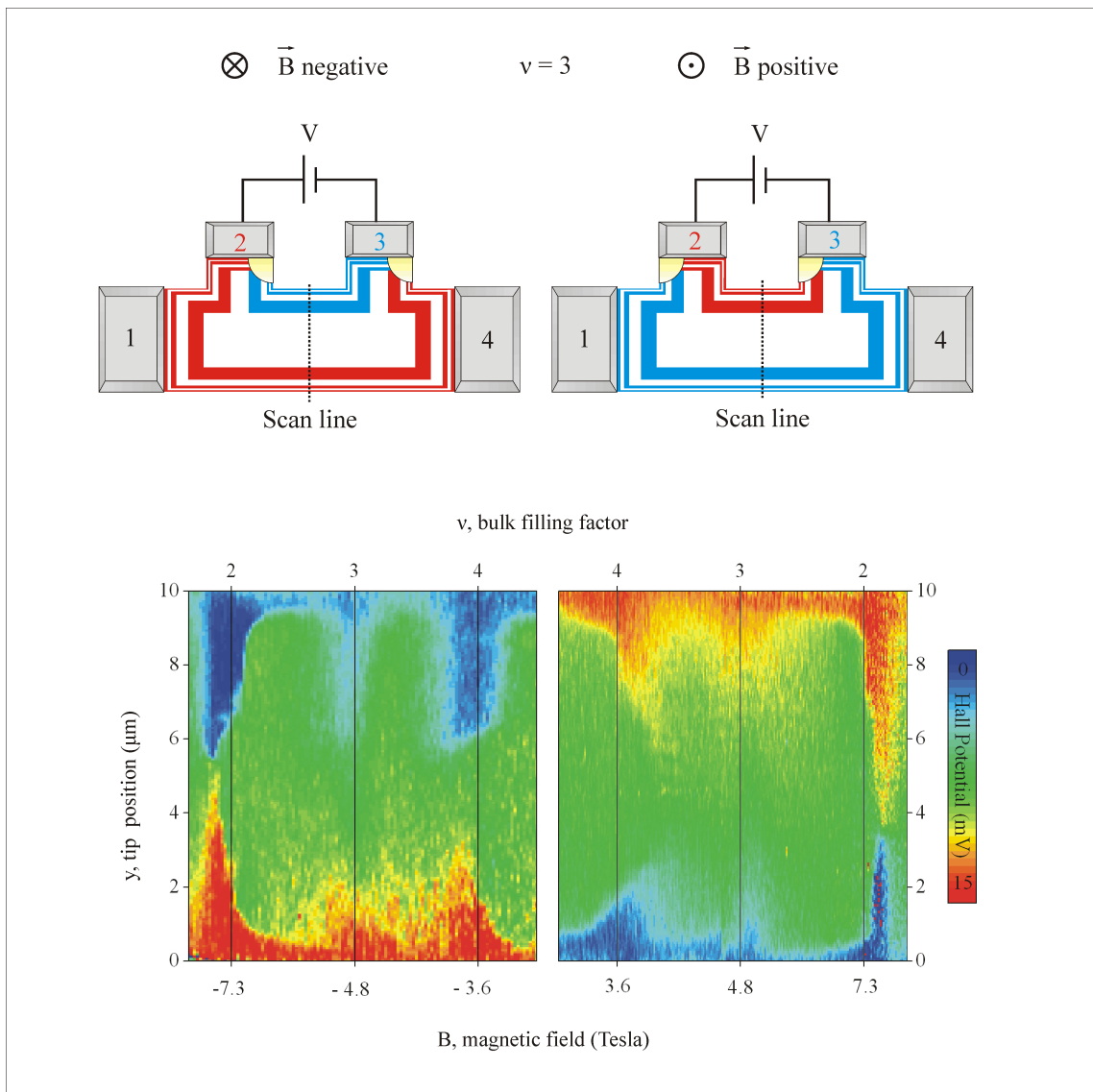
Figure 6.7.: Comparison between model and potential measurements in the setup with current injected in [011] direction via contact 2 and 3.

trochemical potential of the contact 2, whereas the potential in the other edge follows the low electrochemical potential (blue) of the contact 3 (see potential data between $\nu = 2$ and $\nu = 3$ in figure 6.7). Such locally equilibrated distribution of electrochemical potential at the same mesa edge is usually observed in lower mobility samples [2] since the insulating properties of the incompressible strips being less efficient, the adiabatic conditions are not fulfilled.

6.2. Further confirmations of the anisotropy via other configurations

6.2.1. Comparison of the Hall potential distribution for different mesa alignments on the heterostructure crystal

In the previous section, we have presented a model in which the incompressible width is assumed to be larger in front of contacts 1 and 4 than in front of contacts 2 and 3. To confirm this effect of the Hall bar orientation on the transport measurement, the magneto-resistance were measured with mesa either oriented to [011] or to [01-1] direction of the heterostructure crystal (see Fig. 6.8). If the model is plotted for these two configurations in the case of the positive and negative magnetic field, it becomes possible to clarify the measured transport features. Results are displayed in the figure 6.9 in which the incompressible strips have larger thickness in front of contacts with borderline perpendicularly to the [01-1] direction than in front of the other contacts.
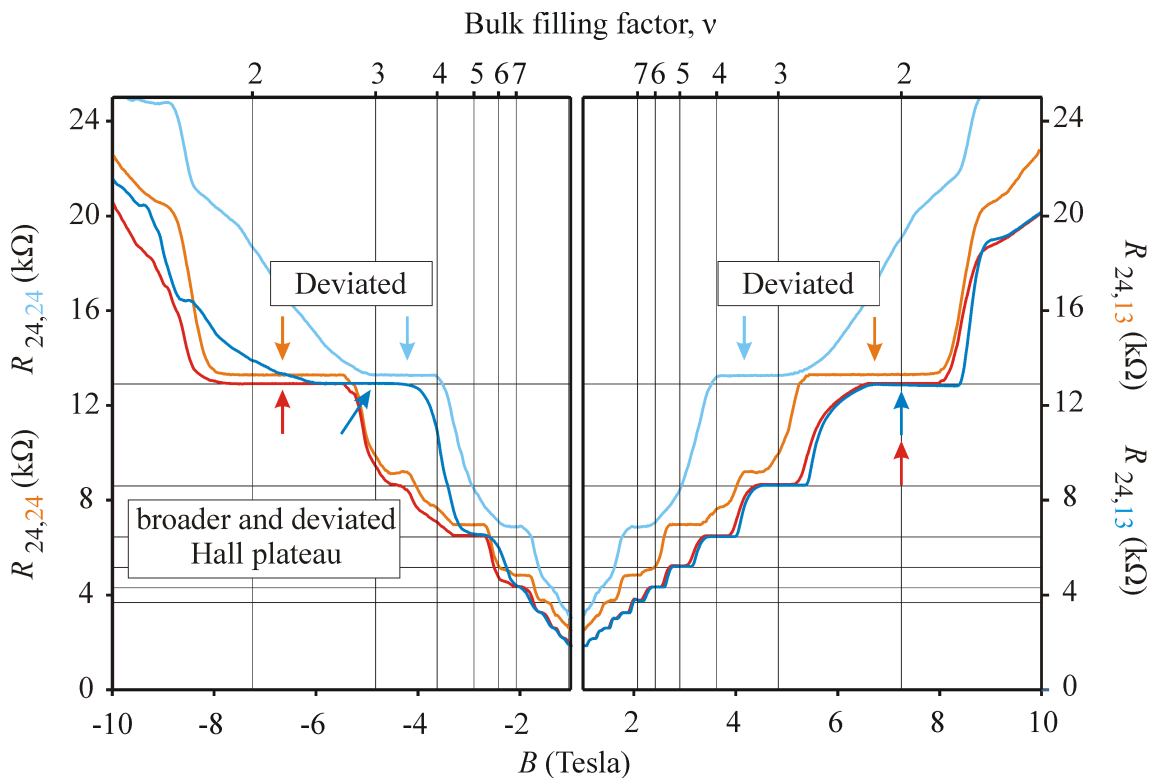
Figure 6.8.: Same as Fig. 4.15 showing two-terminal and atypical Hall resistances in Hall bars oriented by $90\,^{\circ}$ to each other.

If the length of the Hall bar is aligned in the [011] direction or in the [01-1] direction of the heterostructure, the atypical Hall magneto-resistance predicted by the model will be different in positive and in negative magnetic fields as measured in the transport (red and dark blue curves in Fig. 6.8). For the mesa in the [01-1] direction, the model gives high (red) and intermediate (yellow) μ_{elch} at the voltage probing contacts for negative magnetic fields (Fig. 6.9(a)). For positive magnetic fields, these electrochemical potentials are high (red) and low (blue) (Fig. 6.9(b)). For
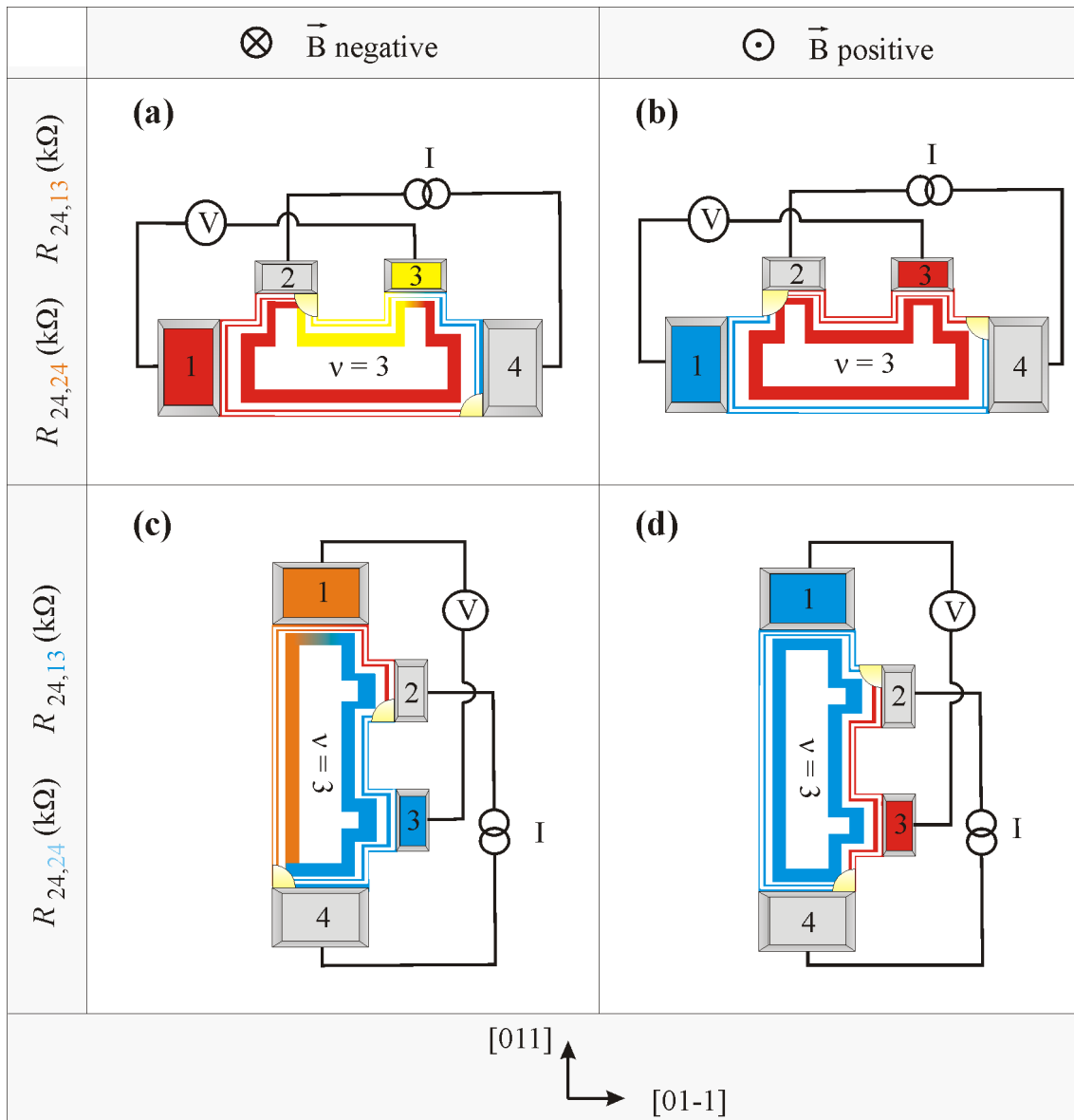
Figure 6.9.: Potential distribution for two different orientations of the mesa with respect to the heterostructure at positive ((b) and (d)) and at negative ((a) and (c)) magnetic fields. The setup measurement corresponds to the atypical Hall configuration.

the mesa aligned in the [011] direction, the model gives a low (blue) and intermediate (orange) μ_{elch} at the voltage probing contacts for negative magnetic fields (Fig. 6.9(c)) versus blue and red at positive magnetic fields (Fig. 6.9(d)).

Finally, the model predicts similar atypical Hall resistances for the configuration (b) and (d) in figure 6.9 but different resistances in the case (a) and (c). These results are also observed in the transport measurements since at positive magnetic field Hall plateaus occur at the expected filling factors for the two crystal orientations, whereas at the negative magnetic field they are deviated to lower magnetic field (compared in Fig. 6.8 red and dark blue curves at positive and at negative B).

6.2.2. Voltage distribution for six- versus four-terminal Hall bar

The magneto-transport changes between a six- and four-terminal Hall bar (see Fig. 6.10 and comments in section 4.2.1). The reason is simply pointed out by our model. The presence of contacts at the two mesa edges in the case of the six-terminal Hall bar modifies the overall potential distribution compared to the four-terminal situation. The latter case which shows
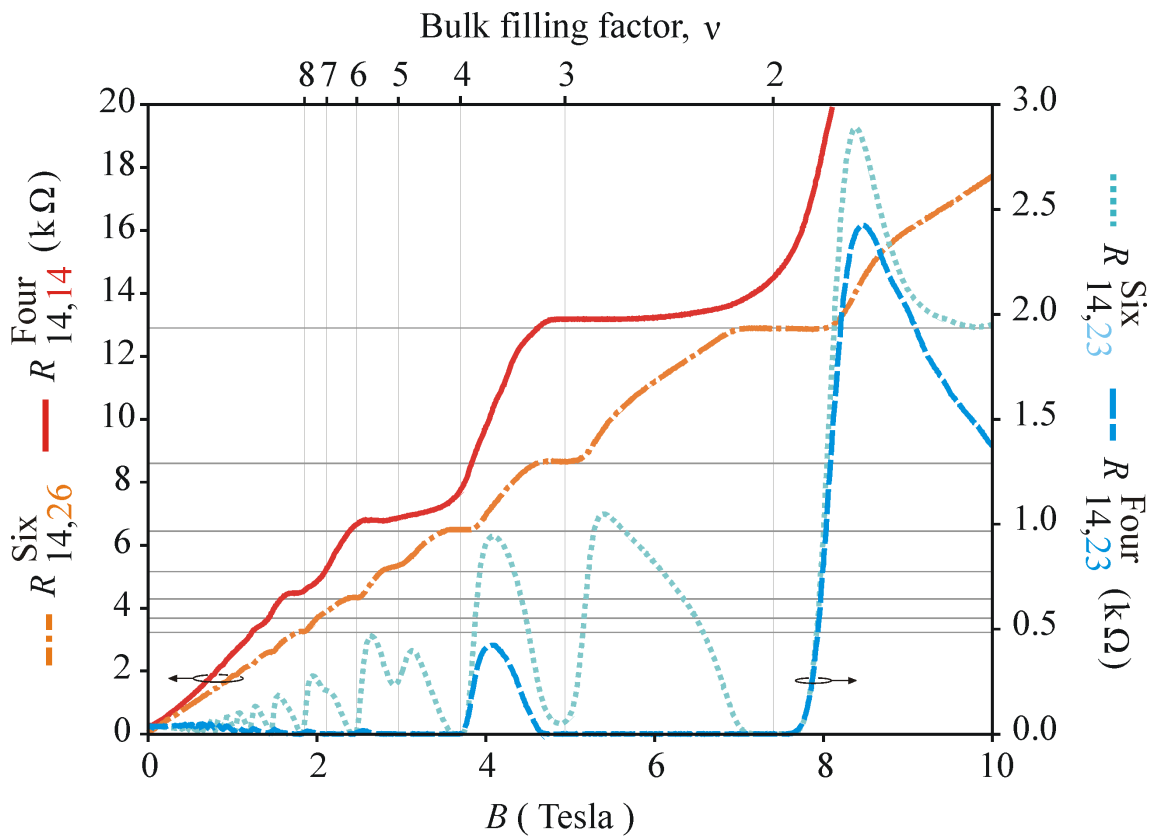
Figure 6.10.: Magneto-resistances measured at 1.4 K in a six- and a four-terminal Hall bar.
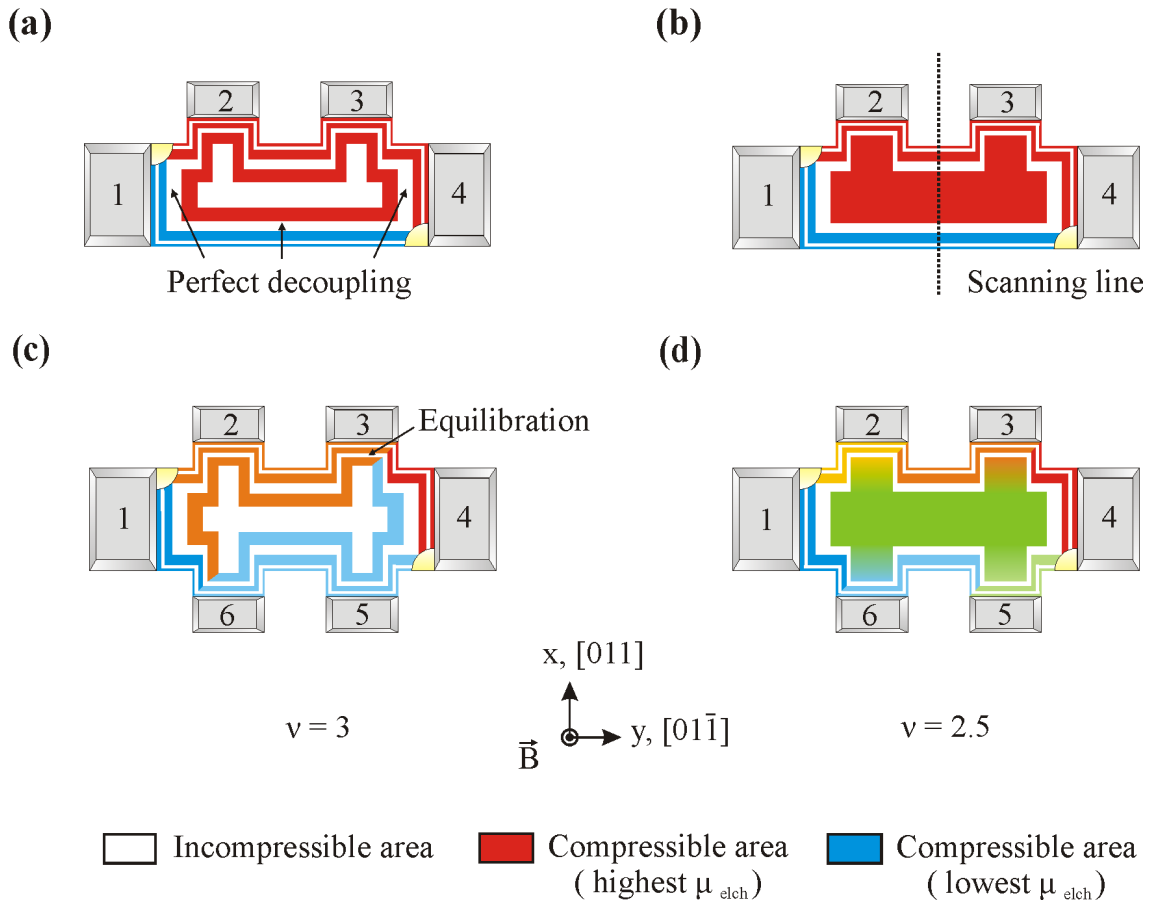
Figure 6.11.: Electrochemical potential in a four and six-terminal Hall bar at $\nu = 3$ and $\nu = 2.5$.

a single potential drop has already been treated in the previous section and consequently no further comments will be done for the configurations (a) and (b) in Fig. 6.11 (they are just represented here for comparison). In the six-terminal Hall bar at $\nu = 3$, the contacts 6 and 3 equilibrate the difference of electrochemical potential between the compressible strips since the incompressible strips in front of them are thin and own a low insulating properties (Fig. 6.11(c)). The contacts 2 and 3 (or 5 and 6) have then the same electrochemical potential, and longitudinal resistances measured with these voltage probes should show zero resistance. At $\nu = 2.5$, the existence of the contact 6 or 5 introduces a mixing between the bulk and the mesa edge. All the contacts get different electrochemical potentials and the longitudinal resistances are therefore not zero anymore. This corresponds to the usual dissipative regime of the IQHE transition.

6.3. Conclusion

Including adiabatic and anisotropic effects, the model presented in this chapter explains qualitatively well our experimental results. The origin of this success can be summarized in the following way. If the interface line of the metal-2DES contact is perpendicular to [01-1] direction, a relatively wide region of reduced carrier density close to the contact is deduced from our experiments. Such reduction leads in high magnetic field to a wide incompressible strip separating electrically the contact and the outer boundary of the 2DES from the bulk region of the 2DES. Since the resistance for a 2DES in strong magnetic fields is proportional to the backscattering of the charges across the width of the device, finite resistance is only expected if both boundaries of the device (upper and lower boundaries) couple to the inner compressible part of the 2DES. This coupling can be established by contacts with a borderline perpendicular to [011]. The phenomena is intrinsic and related to the regular electron depletion in front of contacts. We stress that such depletion is generic and appears for all contacted 2DES. The phenomena in this work is more pronounced or more sensitive due to the small dimensions of the Hall bar structures.

Bibliography

[1] E. Ahlswede, P. Weitz, J. Weis, K. Klitzing, and K. Eberl, Physica B **298**, 562 (2001).

[2] E. Ahlswede, P. Weitz, J. Weis, K. Klitzing, and K. Eberl, Physica E **12**, 165 (2002).

Conclusion and Outlook

The local potential distribution of high mobility 2DES embedded in GaAs-AlGaAs heterostructure has been measured under quantum Hall conditions. These measurements performed via cryogenic scanning force microscopy brought information concerning the microscopic explanation of adiabatic transport features. These adiabatic features are the disappearance of peaks in the Shubnikov-de Haas oscillations, the extension of quantum Hall plateaus to lower magnetic fields and the existence of non-local resistances. As for the usual quantum Hall effect, the present PhD thesis demonstrates that the description based on compressible and incompressible strips is able to explain the magnetotransport results. For instance, the observation of a huge potential drop only located at one border of the mesa is a direct proof of unusual potential distributions under adiabatic transport conditions. In the compressible and incompressible picture, this drop is interpreted as a large difference of electrochemical potential between two compressible areas separated by an incompressible strip owing good insulating properties. Due to the high mobility and small size of the Hall bar, such non equilibrium survives along the complete length of the sample and determines the transport features.

The present PhD work shows that incompressible strips appear in front of alloyed ohmic contact and that they have different insulating properties depending on the orientation. These incompressible strips are broader -so more insulating- if they are located close to contact with an interface perpendicular to the [01-1] direction than if they are in front of contact with an interface parallel to the [01-1] direction. This finding gives a physical meaning to the term "non ideal contact" in the case of low resistive and ohmic contacts. The picture corrects and completes the following statement found in the litterature:

> "Thus our theory of edge states suggests a quite satisfactory explanation of experimental observations of the anomalous QHE with so-called nonideal contacts, which probe only some edge channels. In the same experiment, the usual "bulk" QHE was observed while using standard probes. There is a significant difference in the physics of "bulk" and anomalous QHE's. Quantization of the Hall resistance in the former case is due to the localization of the bulk electron states. Quantization observed with nonideal probes occurs at different values of magnetic field and is due to the lack of equilibration. This effect is not a macroscopic one (it should vanish in sufficient long samples) and usually the quantization is not as good as in

the "bulk" QHE. While the disorder is crucial for the observation of the bulk effect,
it may destroy the anomalous QHE."

D.B. Chklovskii, B.I. Shklovskii and L.I. Glazman, Phys. Rev. Lett. 46, p. 4026
(1992)

Finally our results advertise that every 2DES is inhomogeneous. A 2DES is never a flat distribution of electron but it owns border with gradient of electron density even in front of metal contacts. Any measurement and complete theory should include the effect of what it is called by V. Shikin as "regular inhomogeneities" at the edges of the mesa and in front of contacts [1]. Indeed, such gradient of density determines the insulator properties of the incompressible strips in high magnetic field and therefore the transport (it might also influence the transport measurement in the case of a zero magnetic field). Explanation of other recent experiments might need to include this effect of density gradient. For instance, W. Pan *et al.* [2, 3] explained their transport data with two different electron density areas. It can be that their unintentional variation of electron density is located near the contacts as in our case. Concerning the crystal direction anisotropy, M. Lilly *et al.* [4] found anisotropic behavior in their magneto-transport measurements in high Landau levels. They interpreted their results due to some anisotropy in the 2DES bulk . Since their anisotropy has the same dependence on the crystal orientation as ours, we can wonder if the anisotropy of the regular inhomogeneities in front of contact could be a possible explanation for the origin of this effect. To conlude this part, the present PhD work has strongly highlighted the role of the contact interface. Only few articles are published on this field even though the research community pays tremendous attempts on investigations of transport through 2DES. The reason is that fabrication of reliable contacts is difficult. There are still several open questions on this topic which are mandatory for the scientific community, especially a microscopic understanding of the interface between alloyed contacts and 2DES.

Concerning the cryogenic scanning force microscopy in high magnetic field, the two next challenges are the potential probing in the fractional quantum Hall effect (FQHE) and at the breakdown of the quantum Hall effect - i.e. under high current bias or at high temperature. For the fractional quantum Hall effect, our group is building a similar scanning force system but located inside a ^{3}He-^{4}He dilution fridge. The limited space of a dilution insert makes the project a technical challenge. Adiabatic transport was also observed in the FQHE - the understanding might be based on our results. For the breakdown of the quantum Hall effect, some measurements toward the breakdown were already obtained by E. Ahlswede [5] but the interpretation of this data was a rather difficult issue. Further investigations are needed and especially close to the contact where the breakdown is believed to start [6].

Local probe technique is definitely an important tool to provide microscopic picture of transport phenomena. Such measurements should be encouraged. Recently the quantum Hall effect

has been observed in graphene [7]. Such a single sheet of carbon should facilitate the local investigations of the QHE since graphen gives a 2DES which is directly electrically accessible.

Bibliography

[1] V. Shikin, Phys. Rev. B **64**, 245335 (2001).

[2] W. Pan, J. Xia, H. Störmer, and D. Tsui, Phys. Rev. Lett. **95**, 066808 (2005).

[3] R. Ilan, N. Cooper, and A. Stern, Cond-mat 0601614 (2006).

[4] M. Lilly, K. Cooper, J. Eisenstein, L. Pfeiffer, and K. West, Phys. Rev. Lett. **82**, 394 (1999).

[5] E. Ahlswede, Potential- und Stromverteilung beim Quantum-Hall-Effekt bestimmt mittels Rasterkraftmikroskopie, PhD thesis, Max-Planck-Institut für Festkörperforschung / University of Stuttgart (2002).

[6] S. Komiyama, Y. Kawaguchi, T. Osada, and Y. Shiraki, Phys. Rev. Lett. **77**, 558 (1996).

[7] K. Novoselov, E. McCann, S. V. Morozov, V. I. Fal'ko, M. I. Katsnelson, U. Zeitler, D. Jiang, F. Schedin, and A. K. Geim, Nat. Phys. **2**, 177 (2006).

A. The CSG electrostatic model

This appendix presents some elements of the Chklovskii, Shklovski, and Glazman (CSG) electrostatic model [1]. It follows the lecture of Prof. R.R. Gerhardts entitled *Static screnning in low-dimensional electron systems* (see also [2]).

Chklovskii, Shklovskii, and Glazman analytically and quantitatively calculate the electron density and the electrostatic potential of a 2DES defined by split gates. Their electrostatic approach which includes the non linear screening effect occurring at high magnetic field describes the 2DES edges with its inhomogeneous electron density. The system is shown in figure A.1(a). The 2DES is located at a distance h from the surface at the junction of the AlGaAs layer and GaAs layer. These layers respectively have a dielectrics constant of $\kappa_<$ and $\kappa_>$. The 2DES has a spatial extension in the y direction defined via two gates electrodes at the sample surface [i]. These gates, separated from each other by $W \gg h$, are negatively polarized in order to deplete the 2DES below them. The 2DES density $n_s(y)$ is due to some donor charges ("plus" sign in the draw) which have a constant density n_0. The whole system is neutral and specially $n_s(y) = n_0$ far away from the mesa edge. The determination of the electron density and potential distribution is in principle a 3D problem. The invariance of the 2DES in the x direction and the assumption[ii] that all the donor charges and the potential electrodes are located in $z = 0$ allow to treat the electrostatic problem as one dimensional (Fig A.1(b)). The screening is also assumed to be perfect - i.e. there is no gradient of the electrostatic potential energy $\nabla U(y, z) = 0$ if the 2DES is present.

The first step is to solve the Laplace equation at $z < 0$ and $z > 0$. For this purpose, the properties of the analytic function $F(y + iz)$ is used with

$$U(y, z) = -e \cdot \phi(y, z) = \mathrm{Im}F(\zeta) \quad \text{and} \quad \zeta = \mathrm{y} + \mathrm{iz}. \tag{A.1}$$

The functions $\mathrm{Im}\,\mathrm{F}(\mathrm{y} + \mathrm{iz})$ have the advantage to be a class of functions which are solutions of the Laplace equation $\partial_y^2 U(y, z) + \partial_z^2 U(y, z) = 0$ since $\partial U / \partial y = \mathrm{Im}\,\mathrm{d}F/\mathrm{d}\zeta$ and $\partial U / \partial z =$

---

[i] In their article, Chklovskii, Shklovski and Glazman present the problem in the half-plan of the 2DES. It may be extended to the complete plan.

[ii] This assumption is justified by the value of the electrostatic characteristic length $d \leq 200\ nm$ which is much higher than the gate/2DES distance or the donor/2DES distance (in the order of $60\ nm$). This electrostatic length is characteristic to the electron depletion at the edge.

$\mathrm{Re}\, \mathrm{d}F/\mathrm{d}\zeta$. The function $F(\zeta)$ is determined by the surface charge and the boundary conditions

$$\begin{cases} U(y,0) = U_g & \text{if } y < 0, \\ \kappa_> \dfrac{\partial U}{\partial z}(y,0^+) - \kappa_< \dfrac{\partial U}{\partial z}(y,0^-) = 4\pi e^2 n_0 & \text{if } 0 < y < d, \\ U(y,0) = 0 & \text{if } y > d. \end{cases}$$

These boundary conditions are written in a different way in order to simplify the resolution of the electrostatic problem. The potential energy is separated in two parts: $U = U_1 + U_2$. The first part includes all the effect of the gates potential whereas the effect of the interface charges are added in the second part. The boundary conditions becomes

$$\begin{cases} U_1(y,0) = U_g & \text{if } y < 0, \\ \dfrac{\partial U_1(y,z)}{\partial z}\bigg|_{z\to+0} = 0 & \text{if } 0 < y < d, \\ U_1(y,0) = 0 & \text{if } y > d. \end{cases} \quad \text{and} \quad \begin{cases} U_2(y,0) = 0 & \text{if } y < 0, \\ \dfrac{\partial U_2(y,z)}{\partial z}\bigg|_{z\to+0} = r_0 & \text{if } 0 < y < d, \\ U_2(y,0) = 0 & \text{if } y > d, \end{cases}$$

with the usual 2D screening length $r_0 = 4\pi e^2 n_0/(\kappa_< + \kappa_<)$.

To obtain an analytic solution, CSG assume the perfect screening of the potential by the 2DES -i.e. $U(y,0) = 0$ if $y > d$. After resolution of the electrostatic equation via the analytic
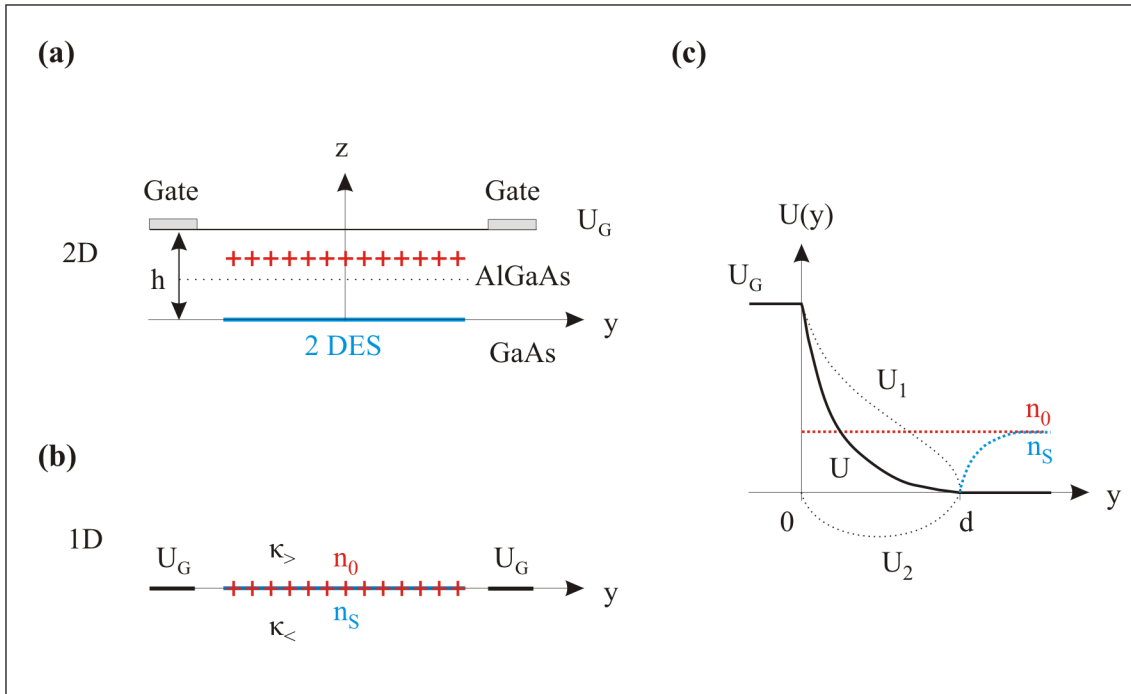

Figure A.1.: **a)** Schematic of an AlGaAs/GaAs heterostruture. **b)** CSG model as a 1D system. **c)** Draw showing the potential and charge density distribution.

properties of $F(\zeta)$ (not detailed here), the dependency of the energy potential U with respect to y is

$$U = U_1 + U_2 = \frac{U_g}{\pi} \left[\frac{\pi}{2} - \arcsin\left(\frac{2y}{d} - 1 \right) \right] - r_0 \sqrt{y \cdot (d - y)}. \qquad \text{(A.2)}$$

In the limit where $y \to d$:

$$U = \left[\frac{2U_g}{\pi} - r_0 \cdot d \right] \sqrt{1 - \frac{y}{d}}. \qquad \text{(A.3)}$$

The smooth connection of the potential at $y = d$ supposes $2U_g/\pi = r_0 d$ with $2\pi e^2 n_0/\tilde{\kappa} = \varepsilon_F/a_0$, $\tilde{\kappa} = (\kappa_< + \kappa_>)/2$ and a_0 the screening length [iii]. Such condition determines the value of the depletion length d: $d/a_0 = 2U_g/\pi\varepsilon_F$.

The electron density profiles $n_s(y)$ at $T = 0$ and $B = 0$ is calculated from the equation

$$\frac{2\pi e^2}{\tilde{\kappa}} \cdot [n_0 - n_{\mathrm{s}}(y)] = \mathrm{Re}\, \mathrm{F}'(\mathrm{y} + \mathrm{i}0^+) = \mathrm{r}_0 \left(1 - \sqrt{\frac{\mathrm{y} - \mathrm{d}}{\mathrm{y}}} \right). \qquad \text{(A.4)}$$

By including the definition $r_0 = 4\pi e^2 n_0/(\kappa_< + \kappa_<)$, it follows [iv] for $y > d$:

$$n_s(y) = n_0 \cdot \sqrt{1 - d/y}. \qquad \text{(A.5)}$$

This electron density $n_s(y)$ is the starting point to treat the perturbation effect of high magnetic field in 2DES. Nevertheless it does not respect the constant electrochemical potential present in equilibrium condition (see the works of R.R. Gerhardts *et al.* as [2]).

Bibliography

[1] D. Chklovskii, B. Shklovskii, and L. Glazman, Phys. Rev. B **46**, 4026 (1992).

[2] K. Lier and R. Gerhardts, Phys. Rev. B **50**, 7757 (1994).

[iii] $a_0 = \tilde{\kappa}\hbar^2/2me^2 \approx 5\,nm$ for $\tilde{\kappa} = 12.4$ as in GaAs.

[iv] In the CSG notation, $n_s(y) = n_0 \cdot \sqrt{\frac{y'-l}{y'+l}}$ since the gate is stopped at $y' = -l$ instead of $y = 0$ and the 2DES starts at $y' = l$, not at $y = d$. To find this form from the equation A.5 , $2l$ should be replaced by d after translating the center of the y-axis by $-l$.

B. Methods to measure the electrostatic potential of 2DES

To extract the 2DES electrostatic potential, several types of methods can be derived from the analytic formulas of the cantilever dynamics. Following the PhD work of Peter Weitz [1], this appendix proposes a list of these methods. It will appear that to obtain the Hall potential of the 2DES without the contribution of the surface charges and buried donors, technique named calibration method is needed. Such technique used during my Ph-D work is presented in the chapter 2.

B.1. Direct measurement of the electrostatic force

The first method to probe the 2DES Hall potential consists to measure directly the electrostatic force. The cantilever is approached to the surface without oscillating - i.e. in a static way. The derivative terms in the second Newton law of motion are zero. The equation of movement becomes: $k \cdot z = F$ which means that the electrostatic force may be measured via the cantilever bending[i]. Using the model of the electrostatic force proposed in the section 2.2.6, the motion is described by

$$k \cdot z = \frac{1}{2}\frac{\partial C_{t,s}}{\partial z} \cdot \phi_{\text{2DEG}}^2 + \frac{\partial Q_t}{\partial z} \cdot \phi_{\text{2DEG}} + \frac{\partial W_{\text{ion}}}{\partial z} \tag{B.1}$$

with $\phi_{\text{2DEG}} = V_{DC} + \Delta\mu_{t,s}^{ch}/e$ and $\phi_{\text{tip}} = 0$ (the tip is grounded). V_{DC} corresponds to the DC voltage applied between the metallic tip and the 2DES [ii].

---

[i] This bending being controlled by the spring constant of the cantilever, a soft cantilever should be used in order to get the largest bending from the smallest force.

[ii] A voltage source which supplies a voltage V_{DC} between two electrodes of different materials defines a difference in the electrochemical potential $\mu^{elch} = \mu^{ch} - e \cdot \phi$. This voltage corresponds to a difference of potential electrostatic if the two electrodes are from the same material -i.e. if they have the same chemical potential.

If this equation is rearranged as following,

$$k \cdot z = \frac{1}{2} \frac{\partial C_{t,s}}{\partial z} \cdot \left(\phi_{2\text{DEG}}^2 + 2 \frac{\partial Q_t / \partial z}{\partial C_{t,s} / \partial z} \cdot \phi_{2\text{DEG}} \right) + \frac{\partial W_{\text{ion}}}{\partial z}$$

$$k \cdot z = \frac{1}{2} \frac{\partial C_{t,s}}{\partial z} \cdot \left[\left(\phi_{2\text{DEG}} + \frac{\partial Q_t / \partial z}{\partial C_{t,s} / \partial z} \right)^2 - \left(\frac{\partial Q_t / \partial z}{\partial C_{t,s} / \partial z} \right)^2 \right] + \frac{\partial W_{\text{ion}}}{\partial z}$$

$$k \cdot z = \frac{1}{2} \frac{\partial C_{t,s}}{\partial z} \cdot \left(V_{DC} + \Delta\mu_{t,s}^{ch}/e + \frac{\partial Q_t / \partial z}{\partial C_{t,s} / \partial z} \right)^2 - \frac{1}{2} \frac{(\partial Q_t / \partial z)^2}{\partial C_{t,s} / \partial z} + \frac{\partial W_{\text{ion}}}{\partial z}$$

the bending z shows a parabolic behavior with respect to the applied voltage V_{DC}. By changing the DC voltage, the maximum of the curve z versus V_{DC} is reached for $V_{DC} = -\Delta\mu_{t,s}^{ch}/e - \partial_z Q_t / \partial_z C_{t,s}$. Due to the existence of the term $\partial Q_t / \partial z$ in doped heterostructure, it's not possible to access the difference of the chemical potential $\Delta\mu_{t,s}^{ch}$ and therefore the 2DES electrostatic potential $\phi_{2\text{DEG}} = V_{DC} + \Delta\mu_{t,s}^{ch}/e$.

B.2. Differential measurement of the electrostatic force

In other technique, an AC voltage modulation is applied to the 2DES. The voltage modulation induces a tip oscillation which depends on the 2DES potential. This technique known as Kelvin probe force microscopy (KPFM) is communally used to evaluate the doping density profiles or to measure the contact potential difference (CPD). The effect of the electrostatic force F on the cantilever tip is expressed by the equation

$$F = m \frac{d^2 z}{dt^2} + b \frac{dz}{dt} + k \cdot z$$

The electrostatic force has the following form:

$$F = \frac{1}{2} \frac{\partial C_{t,s}}{\partial z} \cdot \left(V_{DC} + V_{AC} \sin wt + \Delta\mu_{t,s}^{ch}/e \right)^2 + \frac{\partial Q_t}{\partial z} \cdot \left(V_{DC} + V_{AC} \sin wt + \Delta\mu_{t,s}^{ch}/e \right) + \frac{\partial W_{\text{ion}}}{\partial z} \,.$$

After expending and regrouping, three contributions appears: $F = F_{static} + F_{2w} + F_w$ with

$$F_{static} = \frac{1}{2} \frac{\partial C_{t,s}}{\partial z} \cdot [(V_{DC} + \Delta\mu_{t,s}^{ch}/e)^2 + V_{AC}^2] + \frac{\partial Q}{\partial z} \cdot (V_{DC} + \Delta\mu_{t,s}^{ch}/e) + \frac{\partial W_{\text{ion}}}{\partial z}$$

$$F_w = \left[\frac{\partial C_{t,s}}{\partial z} \cdot (V_{DC} + \Delta\mu_{t,s}^{ch}/e) + \frac{\partial Q_t}{\partial z} \right] \cdot V_{AC} \sin wt$$

$$F_{2w} = -\frac{1}{4} \frac{\partial C_{t,s}}{\partial z} \cdot V_{AC}^2 \cos 2wt$$

The term with a w dependency is detected via lock-in detection. If working at the resonance frequency w_r, the amplitude of the oscillations is given by

$$A = \frac{Q}{k} \cdot F_{w_r} = \frac{Q}{k} \cdot \left[\frac{\partial C_{t,s}}{\partial z} \cdot (V_{DC} + \Delta\mu_{t,s}^{ch}/e) + \frac{\partial Q_t}{\partial z} \right] \cdot V_{AC} \sin wt \,.$$

From the linear behavior of the amplitude A versus V_{DC}, it is possible in principle to reach $\Delta\mu_{t,s}^{ch}/e$ (i.e. $\phi_{2\text{DEG}}$). In doped heterostructures, this method suffers from the same problem as the direct measurement of the force: a term coming from the Q_t charges contributes with the difference of chemical potential.

B.3. Probing the gradient of the electrostatic force

Another measurement process is to keep the tip oscillate around few tens of nanometer above the surface and to probe the resonance frequency shift. An inhomogeneous force with different values with respect to the distance z induces a resonance frequency shift due to the force gradient. This effect is illustrated via Taylor series in the case of a smooth force variation:

$$F(z(t)) = F(z(0)) + \frac{\partial F}{\partial z(t)} \cdot [z(t) - z(0)] + \dots$$

The first term induces a weak correction to the equilibrium position whereas the second term is view as an effective spring constant. By rewriting the equation:

$$[z(t) - z(0)] \cdot k_0 = F(z(0)) + \frac{\partial F}{\partial z(t)} \cdot [z(t) - z(0)]$$

$$[z(t) - z(0)] \cdot \left(k_0 - \frac{\partial F}{\partial z(t)}\right) = F(z(0))$$

$$[z(t) - z(0)] \cdot k_{eff} = F(z(0))$$

it follows: $k_{eff} = k_0 - \partial F/\partial z(t)$ The resonance frequency is changed from $w_0^2 = k/m_{eff}$ to $w_{eff}^2 = k_{eff}/m_{eff}$. The shift of the resonance frequency,

$$\Delta w = w_{eff} - w_0$$
$$= \frac{-w_0}{2k_0} \cdot \partial F/\partial z(t)$$
$$= \frac{-w_0}{2k_0} \cdot \left(\frac{1}{2}\frac{\partial^2 C_{t,s}}{\partial z^2} \cdot \phi_{2\text{DEG}}^2 + \frac{\partial^2 Q_t}{\partial z^2} \cdot \phi_{2\text{DEG}} + \frac{\partial^2 W_{\text{ion}}}{\partial z^2}\right)$$

shows a spatial dependency which is in the second order of $C_{t,s}$, Q_t and W_{ion}.

Bibliography

[1] P. Weitz, Untersuchungen zum Verlauf der Hall-Spannung in einem zweidimensionalen Elektronensystem unter den Bedingung des Quanten-Hall-Effekts mittels eines Raster-Kraft-Mikroskops, PhD thesis, Max-Planck-Institut für Festkörperforschung / University of Hamburg (1999).

C. Hall potential distribution for voltage excitation and/or magnetic field sign permutation

The figure C.1 represents a model to illustrate the effect of inverting the voltage polarity and/or magnetic field orientation on the potential distribution. This model being depicted at $\nu = 3$, the 2DES is separated in three incompressible area (white color) and three compressible area (blue for low electrochemical potential and red for high electrochemical potential). The contacts 2 and 3 are used to induce a current flow by fixing a difference of voltage between them. The voltage excitation is either applied to the contact 2 in the figures C.1(a) or to the contact 3 in the figures C.1(b). In the first case (a), the compressible strips with the low μ_{elch} (blue) provided from the contact 3 are located at the upper edge of the mesa and the compressible strips with high μ_{elch} (red) are at the other edge if the magnetic field is perpendicular out of the page. To reversed magnetic field (i.e. coming in the page), the position of the low and high electrochemical potential is interchanged due to the opposite direction of the skipping orbit propagation [i]. In the second case (b), the distribution of μ_{elch} is reversed in comparison to the case (a) since the voltage polarity of the contact 2 and 3 have been permuted. Similar distribution of μ_{elch} (or Hall potential) is therefore obtained if both the voltage polarity and the magnetic field orientation are changed. It is illustrated in figure C.1 in the case of $\nu = 3$ but it is still valid for all the filling factors (local Hall potential probing confirms this statement - see figure C.2).

---

[i] The magnetic field determines the direction of the skipping orbit which changes with its sign.
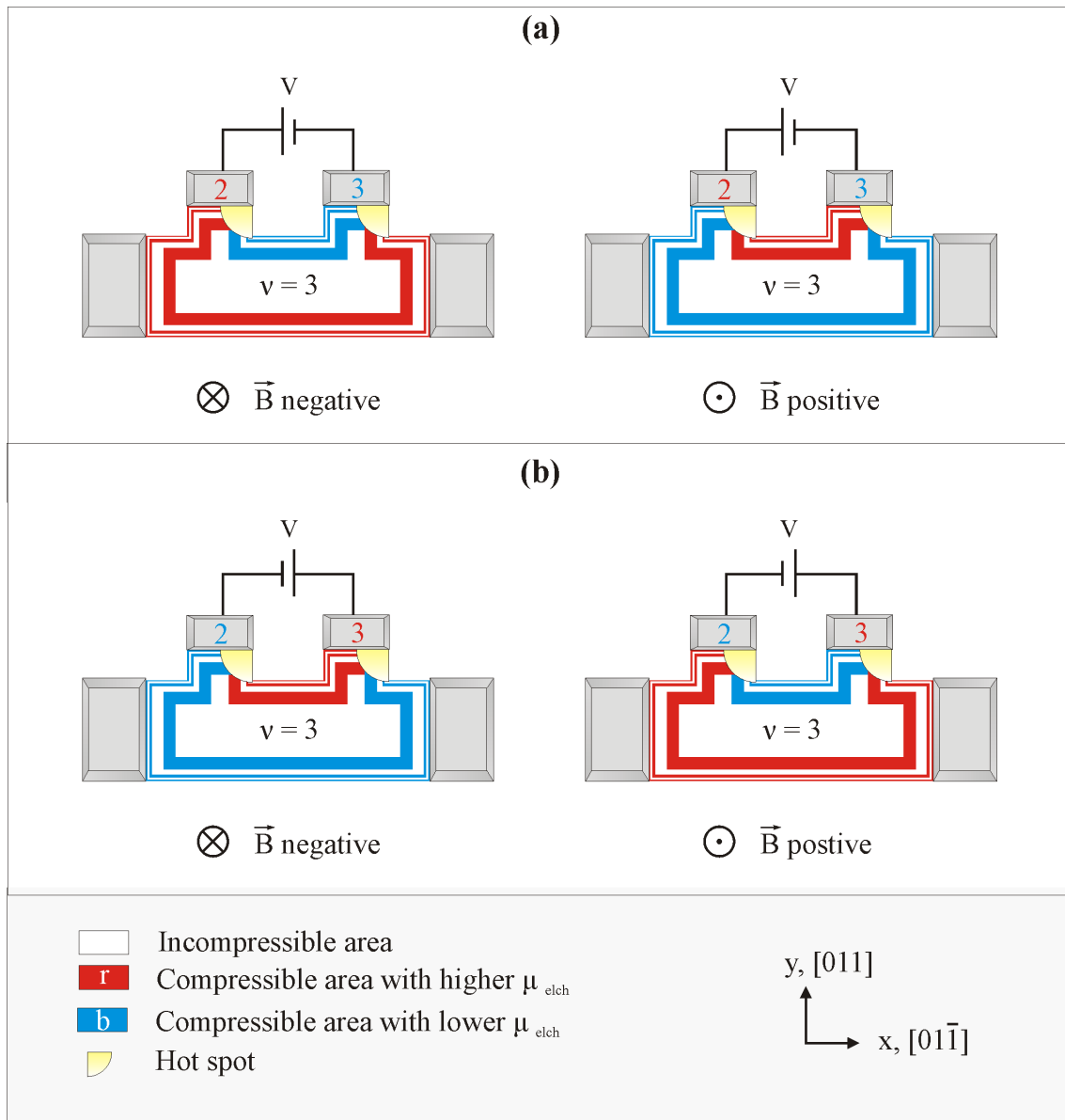
Figure C.1.: Model of the electrochemical potential distribution μ_{elch} for two voltage polarities and magnetic field orientations. The voltage excitation is at contact 2 in **(a)** and at contact 3 in **(b)**. By exchanging the voltage polarity, the same μ_{elch} distribution is restored if the sign of the magnetic field is also inverted.
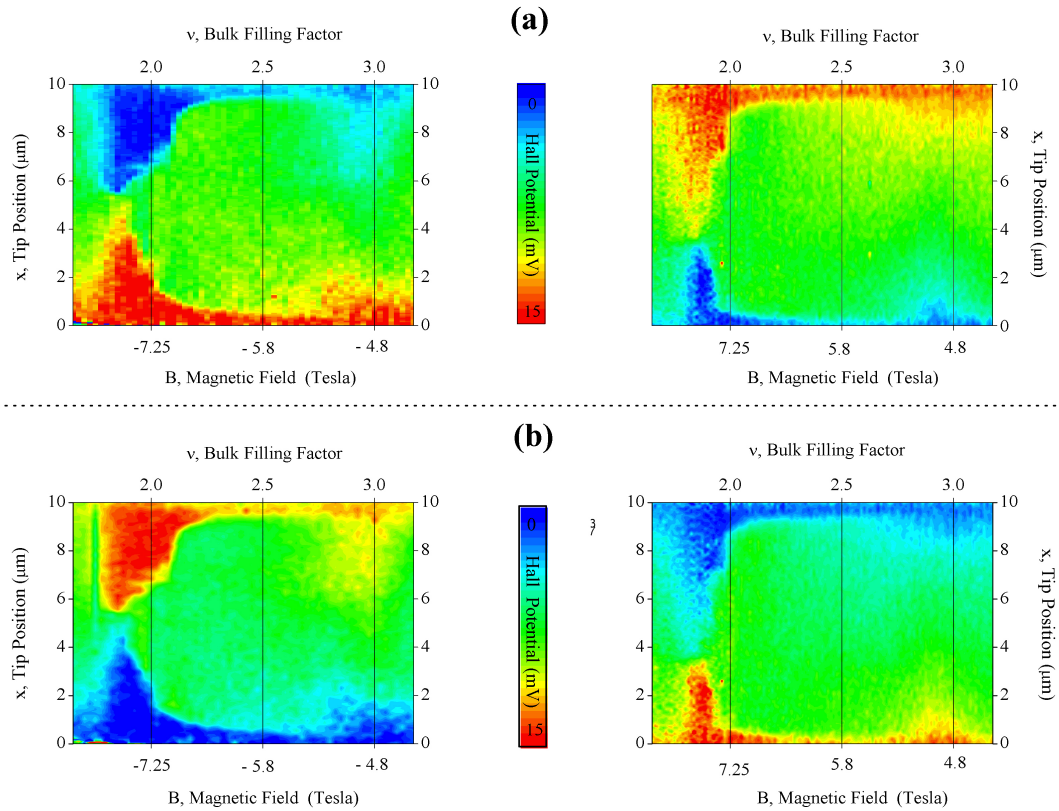
Figure C.2.: Measured distribution of the Hall potential for two voltage polarities and for positive and negative magnetic fields. The voltage excitation is at contact 2 in **(a)** and at contact 3 in **(b)**. By exchanging the voltage polarity, the same Hall voltage distribution results if the sign of the magnetic field is also inverted.

The figure C.2 containing our potential measurements is organized in the same way as the previous figure C.1 in order to facilitate the comparison: first, in the case (a), the voltage is applied to contact 2, then in case (b) the contact 3 performs the voltage excitation. The correspondence with the μ_{elch} distribution as described above is clearly visible. For instance, the Hall potential distribution for the voltage excitation applied to the contact 2 at negative (positive) magnetic fields is similar as the situation in which the voltage excitation is performed via the contact 3 at positive (negative) magnetic fields.

D. Corrections to the Drude longitudinal resistance

At low magnetic field (few milliTelsa), the longitudinal resistance measured in our high mobility 2DES presents some magnetic field dependency (see figure D.1). Such deviation from the Drude formula $\sigma_{xx} = e^2 n_s \tau / m^*$ may correspond to three sources of correction:

1. *The memory effect* [1–4]. By moving and probing the space, the electron remembers when it comes back to the origin if it had suffered scattering at this point. This classical effect induces a strong modification of the magnetoresistance which is negative in the case of short range scattering (like in anti-dots systems) or positive in the case of long range scattering (like in a smooth random magnetic field). Such classical effect is enhanced by magnetic field since the skipping orbit increases the back-trajectories. At higher magnetic field, the Shubnikov-de Haas oscillations destroy it.

2. *The weak localization* [5]. The weak localization is a quantum interference effect. The interferences of closed electron trajectory with itself (the Diffusion term) and with its time reversal trajectory (the Cooperon term) increase the probability to find the electron at the origin and therefore increase the resistance. Such effect is small (around 3% of the magnetoresistance) and it is located on a narrow range of magnetic field since the magnetic field destroys the time reversal symmetry. The weak localization is also very sensitive to the temperature as all interference phenomena.

3. *The electron-electron interaction* [5]. The Drude model does not include the inelastic electron-electron scattering. In the diffusive regime ($k_B T << \hbar\tau$), A. Houghton *et al.* [6] and S.M. Girvin *et al.* [7] extend to strong magnetic field, the electron-electron correction to the conductivity formula of B.L. Altshuler and A.G. Aronov [5] obtained for zero magnetic field. Recently, the ballistic case ($k_B T >> \hbar\tau$) which concerns high mobility 2DES has been treated by Gorny *et al.* [8,9]. A negative parabolic magneto-resistance is found.

In our data presented in the figure D.1, a large peak (20%) is observed around zero magnetic field. The parameters of the 2DES (see section 4.1.4) corresponding to the ballistic regime,

we suspect a classical geometric effect such as magnetic focusing at the entrance of the small contact arms. At larger magnetic field, there is a negative parabolic magnetoresistance which changes with the temperature.

All the theoretical descriptions consider a homogeneous 2DES. I suspect that the lower density at the contact interface is the place of a strongest electron-electron interaction. The local character of a voltage measurement via a voltage probing contact should intensify the relevance of this gradient of electron density at the contact area. Another electron-electron phenomena occurring at very high magnetic field is the Wigner crystal (WC) which may be related to similar border effect by assuming that the WC is formed and probed majoritary near the contact.
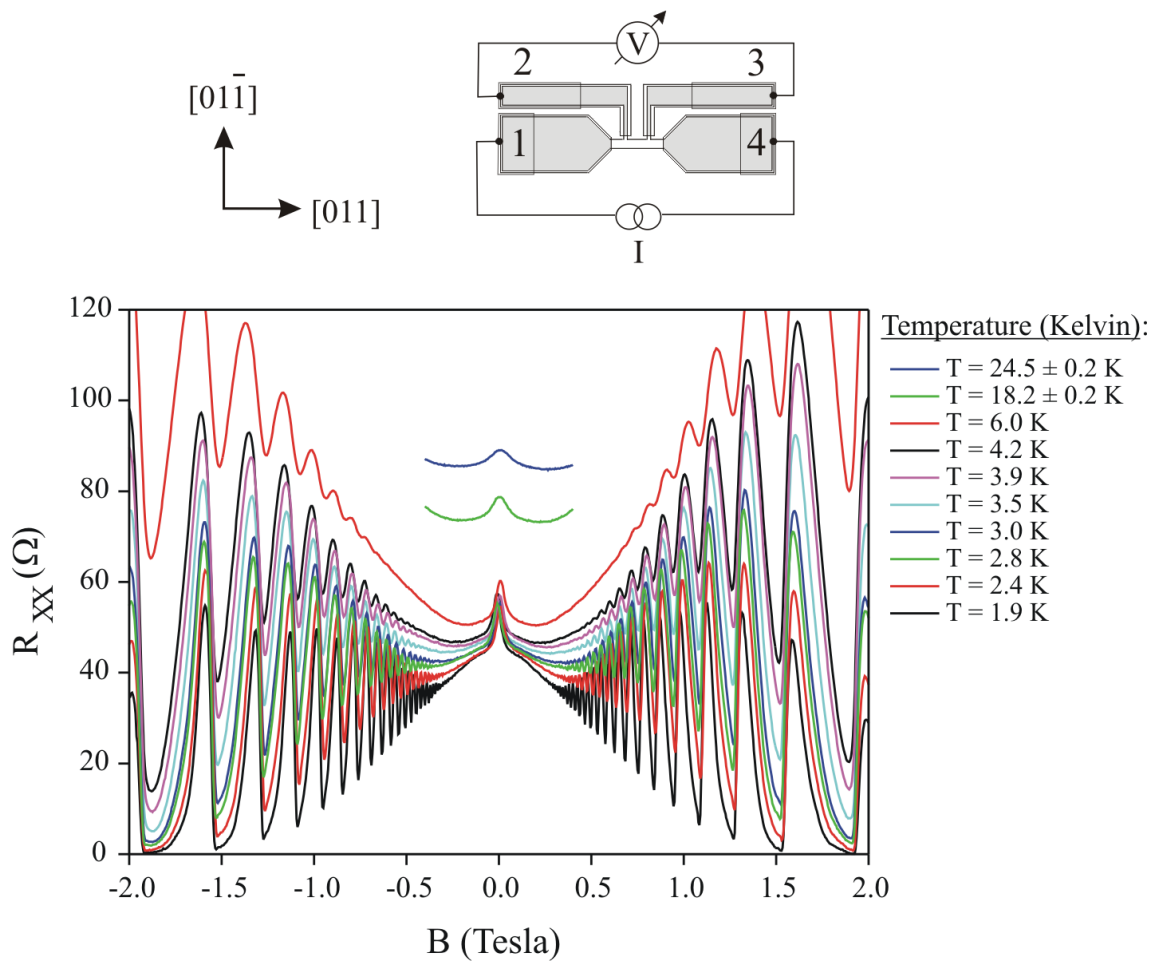

Figure D.1.: The longitudinal resistance is measured at different temperatures. Three regimes exist for different range of magnetic field (see text). This data has been obtained with Dirk Obergfell and Yvonne Bose.

Bibliography

[1] E. Baskin, L. Magarill, and M. Entin, Sov. Phys. JETP **48**, 365 (1978).

[2] E. Baskin and M. Entin, Physica B **805**, 249 (1998).

[3] A. Bobylev, F. Maao, A. Hansen, and E. Hauge, J. Stat. Phys. **87**, 1205 (1997).

[4] A. Dmitriev, M. Dyakonov, and R. Jullien, Phys. Rev. Lett. **89**, 266804 (2002).

[5] B. Altshuler and A. Aronov, in *Electron-electron interactions in disordered systems*, edited by A. Efros and M. Pollak (Elsevier, Amsterdam, 1985).

[6] A. Houghton, J. Senna, and S. Ying, Phys. Rev. B **25**, 2196 (1982).

[7] S. Girvin, M. Jonson, and P. Lee, Phys. Rev. B **26**, 1651 (1982).

[8] I. Gornyi and A. Mirlin, Phys. Rev. B **69**, 045313 (2004).

[9] I. Gornyi and A. Mirlin, Phys. Rev. Lett. **90**, 076801 (2003).

E. Description of the tip preparation and mounting on the setup

This appendix describes how the cantilever tips are prepared and mounted on the measurement setup.

E.0.1. Tip preparation

The first step of the measurement process is to metallize the silicon piezoresistive cantilever [i] since magnetic field has a strong effect on the silicon but few on metal (connected to the ground potential, the tip is also used as reference potential). This affects the work function difference and therefore causes an electrostatic force between the metalized tip and the semiconductor sample. The figure E.1(c) represents the schematic of cantilever-tip packaging with their ceramic holder. The free standing cantilever (Fig E.1(a)) and the static cantilever used as a reference resistance are integrated in a conductive circuit which forms the Wheatstone bridge. This circuit inserted in an insulator material (black part in the drawing) is hold by a ceramic plate which contains two large gold pads. The silicon is asymmetrically doped on one surface of the cantilever (Fig E.1(b)) to assume a net change of the resistance due to the piezoresistive effect. The system is then further prepared by us. The tip is metallized in order to contact it to the ground reference potential. A 100 nm thin layer of gold/palladium is evaporated with an Univex thermal evaporating system[ii]. To avoid shortcut in the electrical circuit, a thin layer of polyamide (blue layer in Fig E.1(b-d)) is before brushed over the top part of the aluminum circuit whereas the bottom part of the circuit is protected by Fixoglue which is removed after the process. Two thin ceramic plates with a gold layer on the surface are added by gluing them and serve as a pad for the soldering of the contact wires. Microbonding between the gold pads and the aluminum circuit is performed (red lines in figure E.1(d)) and contacts are improved by the adding of a small droplet of silver paste (Fig E.1(d)).

---

[i] The cantilevers are bought from Veeco metrology group.

[ii] This thickness allows to get a homogeneous metallic surface and the palladium avoids the formation of gold pyramids during the evaporation.

E.0.2. Tip mounting

After their fabrication, the tip and the sample are mounted on the piezoelectric tube and table respectively in order to be inserted inside the cryostat. The ceramic plate in which the cantilever tip is installed are directly screwed to a Macor cube glued at the end of the scanning piezotube. Three small screws in a triangular geometry guarantee a good mechanical coupling between the exciter and the cantilever. The electrical connections are done with a conventional soldering iron.

The sample owning different Hall bar microstructures are glued on a sample holder. The CrAu contact pads of the Hall bar are then connected to the sample holder via microbonding. The sample holder is then glued with silver epoxy on the sapphire central tube of the piezotable which performs the z axis movement. The silver epoxy allows the thermalization between the piezotable and the sample holder. The piezotable part is screwed to the bottom of the cryostat insert in the way that the cantilever tip of the detection system is installed above the sample. Precise positioning of the tip over the Hall bar structure is done with a light microscope. One millimeter distance between the tip and the sample is kept to safety reason since the thermal expansion and contraction of the material setup may crash the tip on the surface of the sample during the cooling process. The head is closed with a vacuum sealing and pump to perform leakage detection. Few helium gas is added to the chamber to assume a good thermalization via convection. Finally, the insert is slowly moved inside the VTI of the cryostat and the Helium circulation is started. After reached 1.4 K, the exchange gas in the vacuum chamber is removed until a pressure of 10^{-2} mbar.
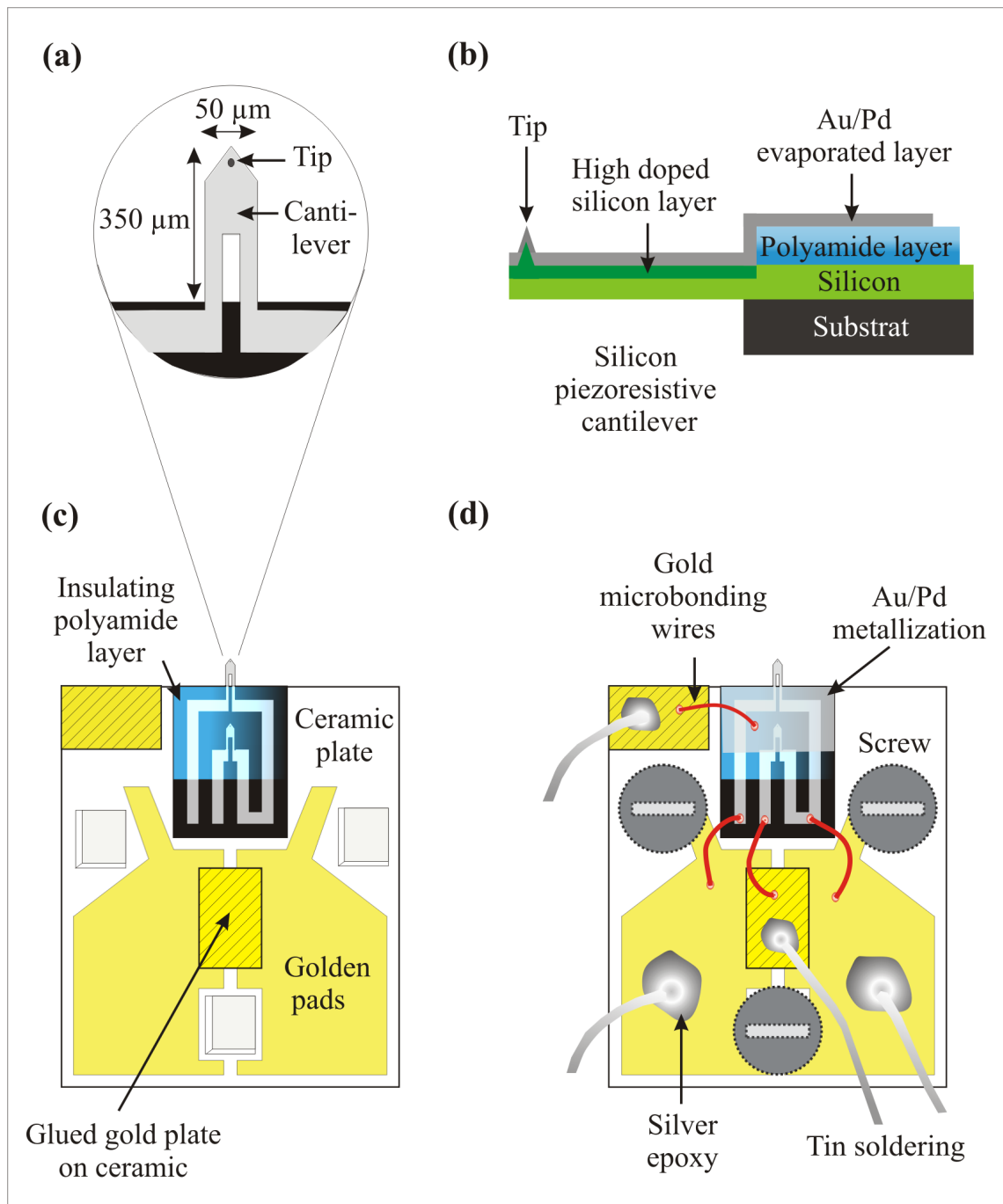
Figure E.1.: **a)** Zoom in the freestanding cantilever tip. **b)** Cut view of the silicon cantilever system after our metalization preparation. Polyamide layer protects the electrical circuit from the evaporated AuPd layer. **c)** Ceramic plate on which the electrical circuit containing the cantilevers is integrated. Insulating polyamide layer and thin gold layer on ceramic plate are added. **d)** Au/Pd thin layer is evaporated in order to connect the tip to the ground potential. The connections are done by gold microbonding and tin wires. The ceramic plate is hold to the scanning piezoelectric tube by three screws.

Zusammenfassung

Bei sehr tiefen Temperaturen und hohen Magnetfeldern zeigen zwei-dimensionale Elektronensysteme (2DES) den ganzzahligen Quantum-Hall-Effekt. Im Frühjahr 1980 entdeckte Klaus von Klitzing, dass der Hall-Widerstand - d.h. das Verhältnis zwischen Hall-Spannung und eingeprägtem Strom - quantisierte Werte über breite Magnetfeldbereiche annimmt. Für diese wichtige Entdeckung wurde ihm der Nobelpreis für Physik 1985 zuerkannt. Der präzise Wert für den Füllfaktor $\nu = 1$ entspricht der von-Klitzing-Konstante R_K, die als $R_K = h/e^2$ identifiziert wurde. Da die Feinstrukturkonstante α direkt mit der von-Klitzing-Konstante R_K zusammenhängt, schlug er vor, den Quantum-Hall-Effekt zur genaueren Bestimmung von α zu benutzen. Unabhängig davon wird der Quanten-Hall-Effekt wegen seiner hohen Reproduzierbarbeit und Unabhängigkeit von der genauen Probengeometrie seit 1990 als internationaler Widerstandsstandard verwendet.

Mikroskopische Modelle, um dem Quanten-Hall-Effekt zu erklären, wurden sehr kontrovers diskutiert. In unserer Gruppe konnten P. Weitz und E. Ahlswede mit Hilfe eines Rasterkraftmikroskopes die Potentialverteilung in einer Quanten-Hall-Probe basierend auf einer GaAs-AlGaAs-Heterostruktur mit Erfolg messen. Dieses ortsaufgelöste Bild des Potentials und der Stromverteilung führte zur Entwicklung eines geschlossenes theoretischen Bildes zur Erklärung des Quanten-Hall-Effekts. An den Rändern eines zweidimensionalen Elektronensystems steigt in der etwa $1\,\mu$m breiten Verarmungszone die Elektronendichte von Null auf den Wert des Innern an. Entlang der Ränder bildet sich eine streifenartige Struktur der Elektronendichte aus, in der sich die Streifen konstanter Elektronendichte inkompressibel verhalten, diejenigen variierender Elektronendichte kompressibel. In den kompressiblen Bereichen existieren besetzte und unbesetzte Elektronenzustände am Fermi-Niveau, die eine isoenergetische Umbesetzung zur elektrischen Abschirmung möglich machen. In den inkompressiblen Bereichen liegen besetzte Zustände unterhalb des Fermi-Niveaus, unbesetzte oberhalb, sodass dort elektrische Felder durch Elektronenumbesetzung nicht abgeschirmt werden können. P. Weitz and E. Ahlswede entdeckten oberhalb ganzzahliger Landauniveau-Füllfaktoren Abfälle der Hall-Spannung nur an den innersten inkompressiblen Streifen symmetrisch an beiden Rändern. Aus diesem Umstand konnte geschlossen werden, dass der dissipationfrei Strom in inkompressiblen Streifen fließt.

In der vorliegenden Arbeit wurde mit dem gleichen Tieftemperatur-Rasterkraftmikroskop Hall-Potential-Profile in 2DES mit höherer Elektronenbeweglichkeit unter Quanten-Hall-Be-

dingungen gemessen. Überraschend konnte ich in diesen Proben sogenannte adiabatische Transportphänomene beobachten, d.h. zu niedrigen Magnetfeldern verschobene Hall-Plateaus, unterdrückte Längswiderstände und das Auftreten von nichtlokalen Magnetowiderständen. Diese Phänomene wurden in der Literatur mit dem Auftreten von einer Nichtgleichgewichtssituation zwischen Randkanälen interpretiert.

Durch systematische Magnetotransport- und rasterkraftmikroskopische Untersuchungen gelang es mir, ein mikroskopische Beschreibung im Rahmen kompressibler und inkompressibler Streifen zu erhalten. So konnte ich zeigen, dass entlang der einlegierten Metallkontakte eine elektrostatische Verarmung im 2DES auftritt, die in hohen Magnetfeldern zum Auftreten eines inkompressiblen Streifen, and damit zu einer Isolation zwischen Rand und Innern des 2DES führt. Wichtig ist hierbei, dass die Isolationswirkung (wahrscheinlich aufgrund der Breite) des inkompressiblen Streifens von der Orientierung der Kontakt/2DES-Grenzlinie relativ zur Kristallorientierung der GaAs/AlGaAs-Heterostruktur abhängt. Erst diese Anisotropie in der Breite der Streifen erklärt die gemessenen Potentialverteilungen und Magnetotransportmessungen in diversen elektrischen Anordnungen und Hallstruktur-Orientierungen.

Die Arbeit gliedert sich in eine kurze Einführung in zwei-dimensionale Elektronensysteme und grundlegende Aspekte des Quanten-Hall-Effekts (Kapitel 1) und der Messtechnik (Kapitel 2). Das Kapitel 3 führt in den adiabatischen Magnetotransport ein und das vierte Kapitel präsentiert solche Messungen an meinen Proben. Daran schliesst sich die Darstellung der Potentialmessungen in Kapitel 5 an. Aus diesen wird in Kapitel 6 ein Modell entwickelt, mit dessen Hilfe auch die Transportmessungen erklärt werden könne.

Acknowlegdement

Prof. Klaus von Klitzing gave me the opportunity to study the quantum Hall effect (QHE) under his supervision. His expertise and vision in the field were always helpful. His group also offers all the best working facilities.

Jürgen Weis has followed my PhD work. With his detailed knowledge concerning physics concepts, he was often thinking one step ahead. This was an important help for me. The present manuscript has been also greatly improved thanks to his suggestions.

I would like to thank my friend and mentor Dr. Erik Ahlswede who taught me with passion and patience the local Hall potential probing. Our mutual attraction for the physics, the common interest in mountains and the piano create our strong friendship inside and outside the MPI.

Cher David Quirion - mon autre moi-même, we spent time together quite often at the corridor of my lab either to speak about sophisticated physics (I remenber that you explained to me once the relation between the quark theory and the Kondo effect) or to debate on the concept of "Visage" in the philosophy of Levinas. You came also several times to help me in order to solve lab problems. Merci!

All along my PhD time, Armin Christian Welker has shared his office, his happiness ("we are the champions, my friend") and unhappiness ("this is the end") with me. Showing availability to help everyone at any time, he secured me many times from computer crises.

I got the chance during my PhD to work with Yvonne Boose who did her internship with Jürgen Weis and me. Her motivation and happiness brought a large positive wave in the group. Thanks for this (et pour le chocolat). After several questions concerning her future orientation, she finally decided to join the physics research. I hope in the future to have the chance to supervise her PhD.

Prof. R. Gerhardts - theoretician in the von Klitzing group, has spent part of his research time on screening phenomena in low dimensional systems. Interactions with him were in consequence very fruitful. He gave several lectures on this topic and I have learnt a lot from him. I also had the chance to exchange experiences with Dr. Afif Siddiki. Theoretician and guitarist who enjoys J.P. Sartre, Afif always gives serious advices but not without some humor.

Thanks to Prof. Dr. Werner Dietsche who is the specialist in our group of growth of AlGaAs/GaAs heterostructure.

During my PhD, I got strong support in the cleanroom by Monika Riek (for samples' fabrication), Achim Güth (for teaching me design software), Thomas Reindl (for SEM support) and

Ulrike Weizmann (for loving South of France). Thanks a lot to all of them!

The von Klitzing group has also very qualified technical staffs for example Manni Schmid. I appreciate their help and comments. Thanks to the specialists of microbonding: Benjamin Stuhlhofer and the angel Frank Scharttner. Many thanks to the people of the low temperature service. I would also like to mention all the nice guardians of the MPI - unique witness of our workholic symptom, who always give us mental support by their smiles and happiness.

I would like to thank Oktay Göktas who is doing a lot of work concerning the alloyed contacts on 2DES. It was helpful to discuss with him and I was very impressed by his motivation.

Merci to Eleonora Storace who has always corrected my abstracts. Even with some lightnings, I wish you enjoyed the trip to Grenoble mountains as much as I appreciated the journey to Venice.

Ruben Esteban - my Stuttgart mother, I feel gratitude for your generosity since you brought to me food on sunday at the MPI during my PhD writing period. Years after our trip to the black forest, I still look at my (bloody) feet, but now with some happiness.

Thomas Reindl, ami discret, plein de finesse et d'ironie. Always at the top of the technology! I dream sometimes that you will come for few months to France to work together on SETs.

Walter Schmidt, you were "le père fondateur" with the present author of the Café Weiss meeting. It always had a nice atmosphere and it gave the occasion for the MPI physicists to relax on the Friday nights. I would also like to mention how you tried to help me by building a new cryostat insert for my system. I really appreciate your way of thinking for a group, not for yourself.

Vielen Danke an meine Freund Stefan - fournisseur officiel de programmes informatiques et de médicaments. I wish you will get beautiful pictures of the Hall potential profile in the fractional quantum Hall regime.

Dirk Obergsfell is an example of a very motivated PhD student. When I needed to measure temperature dependence, he directly accepted and spent time to show me his system. Merci Dirk.

Several conferences and meetings gave me the occasion to meet a lot of nice physicists. I would like to mention Prof. Josef Oswald who kindly invited me to visit him at his university in Austria, Dr. Kawano with memories of his trip to Stuttgart and Dr. Hartmut Buhmann with whom we tested the Würzburg wines. A special thanks to Ferdinand Evers who helped me to find my way into solid state physics and who showed me the perfect example at the beginning of my carrier.

During my PhD, I attended several lectures at the university of Stuttgart. I specially enjoyed the lecture of Kasten Held on "theory of quantum dots", "the screening theory on low dimensional systems" by Prof. Gerhardts and the lecture on "group theory" of Heinz Barentzen. Thanks a lot to these lecturers.

To summarize, I would like to thank all of you for joining the climbing, boules games or Cafe Weiss meeting, for coming to mountain trips and to accept to test my crepes and my experimental Thai cuisine or to share a waterpipe. I also apologize to have split too often my time with you and my lab.

Since a few months, I am back to Grenoble and new colleagues have welcomed me in their Neel Institute. I would like to thank them: merci à Hervé, Sukumar, Aurélien, Nele, Julien, Thomas, Cécile, Emile, Philippe et Etienne.

I would also like to thank my friends from France: Merci à mes amis d'enfance: Magali, Christophe, Jérome, Emilie, Aurélie et Sophie. Merci à mes amis du collège: Nathanaël, Nathalie, Romain, Cécile, David et Guillaume. Merci aux amis du Lycée: Guillaume, Olivier, Damien, Blaise, Laurent et Stéphane(s), ainsi qu'à mes amis philosophes: Damien, Alberto et Daunia, et à mes trois frères marocains: Fred, Jilles et Khalid. Merci à vous tous qui malgré mon exil dans la physique et en Allemagne avez toujours su me témoigner votre amitié.

To finish, I thank my grand-mother and grand-father, my parents - Isabelle and Denis, my marvelous sisters - Frédérique, Bénédicte and Aude, and the new members of the family - Mathias, Renaud and Noa. During my studies, they always provided me strong support. Merci!

Summarize

In this PhD work, the local potential distribution of a high mobility 2DES has been measured under quantum Hall conditions. The 2DES embedded in a GaAs-AlGaAs heterostructure designed in a small Hall bar geometry shows intrinsic adiabatic transport features. Usually presented in the literature with the edge state picture, these features are the disappearance of peaks in the Shubnikov-de Haas oscillations, the extension of quantum Hall plateaus to lower magnetic fields and the existence of non-local resistances. Our local potential measurements obtained with a cryogenic scanning force microscope present another microscopic explanation of such adiabatic transport. The new picture is based on compressible and incompressible strips. An incompressible strip is a region in which the Fermi energy is located inside the energy gap (the electron density is constant and the electrostatic potential is changing) whereas a compressible strip occurs if the Fermi energy is pinning inside a Landau level (the electron density is changing and the electrostatic potential is screening). In previous work, the compressible and incompressible strips model has been successfully used to describe the quantum Hall effect. The present work demonstrates that the strips distribution accounts also for the adiabatic transport features observed on high mobility samples in the quantum Hall regime.

Our research shows that in adiabatic situations, compressible regions with an unusual difference of electrochemical potential are found to coexist along the same edge due to an insulator-like incompressible strip in between and due to the lack of impurities scattering. Due to the high mobility and small size of the Hall bar, such non equilibrium survives along the complete length of the sample and determines the transport features. The insulator properties of incompressible strips in front of the alloyed ohmic contacts are found to be anisotropic with a dependency on the orientation of the contact borderline with respect to the crystal direction. The incompressible strips are broader -so more insulating- if they are located close to contact with an interface perpendicular to the [01-1] direction than if they are in front of contact with an interface parallel to the [01-1] direction. This finding gives a physical meaning to the term "non ideal contact" in the case of low resistive and ohmic contacts.

Finally our results advertise that every 2DES is inhomogeneous. A 2DES is never a flat distribution of electron but it owns border with gradient of electron density even in front of metal contacts. These "Regular inhomogeneities" at the edges of the mesa and in front of contacts determines the insulator properties of the incompressible strips in high magnetic field and therefore the transport.

Curriculum Vitae

Franck DAHLEM
Nationality: French
Date of birth: 12th July 1978

EDUCATION

2007–present : CNRS Postdoc: Niobium wire under biased current measured by combined AFM/STM at millikelvin range, Néel Institute, Grenoble.

2002–2007 : PhD thesis: local potential profiles of the adiabatic transport in quantum Hall regime, Max Planck Institute, Stuttgart.

2001–2002 : Master degree of history and philosophy of science, Sorbonne University, Paris.

2000–2001 : Master degree of physics of matter and light, Joseph Fourier University (UJF), Grenoble.

1999–2000 : A Four-year university diploma on research physics ("Maîtrise"), UJF.

1998–1999 : A three-year university diploma on research physics ("Licence"), UJF.

1997–1998 : A two-year university diploma on science of matter ("DEUG"), UJF.

: A first-year university on philosophy, Pierre Mendès France University, Grenoble.

1996–1997 : Preparation to engineer schools, Champollion high school, Grenoble.

1995–1996 : Baccalauréart degree, Grésivaudan high school, Grenoble.

TRAINING EXPERIENCES

- 2002: One year of philosophical research with M. Bitbol, PARIS.
  Report on decoherence theories and the quantum measurement problem.

- 2001: Four months training at the Louis Néel Laboratory with R. Giraud, W. Wernsdorfer and B. Barbara, Grenoble.
  Report on quantum phase transition in rare earth hydroxides and molecular crystals.

- 2000: Five months training at the Institute for condensed matter theory with F. Evers, Karlsruhe.
  Article on Nonadiabatic scattering of a quantum particle in an inhomogeneous magnetic field, Dahlem et al., Europhys. Lett. 55, 603.

SCIENTIFIC CONTRIBUTIONS

- "Local probing of adiabatic transport in the IQHE"
    - Cargèse International School: Magnetic Fields for Science, 2007 (Talk).
    - Leoben University (Austria), 2007 (Invited talk).
    - GDR méso, Aussois, 2007 (Talk).
    - G.E.S. Laboratory, Montpellier, 2007 (Invited talk).
    - Journées de la Matière Condensée 10, Toulouse, 2007 (Invited talk).
    - International Conference on Physics of Semiconductors, Vienna, 2006 (Poster).
    - High Magnetic Fields in semiconductor physics, Würzburg, 2006 (Poster).
    - international winterschool on new developments in solid state physics, Mauterndorf, 2006 (Poster).

- School before PhD on mesoscopic physics, Les Houches, 2001.

- "Discours sur l'origine et les fondements de l'inégalité parmi les hommes de J.J Rousseau", German summer university with the Studenstiftung des Deutschen Volkes, la Rochelle, 1999 (Talk).